Dynamic Interaction Between a Two-Phase Submarine Landslide and a Fluid Reservoir

DISSERTATION

SUBMITTED FOR THE
PARTIAL FULFILLMENT OF THE REQUIREMENT FOR
THE MASTER OF PHILOSOPHY (M. Phil.) DEGREE
IN MATHEMATICS

BY

JEEVAN KAFLE

DEPARTMENT OF NATURAL SCIENCES
SCHOOL OF SCIENCE
KATHMANDU UNIVERSITY, DHULIKHEL, KAVRE, NEPAL
MARCH, 2014

Dedication

.....to my parents

Bhagawan Prasad Kafle

and

Chandra Kumari Kafle

Certificate by the Supervisors

The dissertation entitled **Dynamic Interaction Between a Two-Phase Submarine Landslide and a Fluid Reservoir** presented by Jeevan Kafle under our supervision is hereby submitted for the partial fulfillment of the Master of Philosophy (M. Phil.) Degree in Mathematics to the Department of Natural Sciences, School of Science, Kathmandu University, Dhulikhel, Kavre, Nepal.

Dr. Shiva P. Pudasaini
(Supervisor)
Professor, Kathmandu University
School of Science, Department of Natural Sciences
Dhulikhel, Kavre, Nepal

and

University of Bonn
Faculty of Mathematical and Natural Sciences
Department of Geodynamics and Geophysics
Meckenheimer Allee 176, D-53115 Bonn, Germany.
Date:

Dr. Dil B. Gurung
(Co-supervisor)
Associate Professor, Kathmandu University
School of Science, Department of Natural Sciences
Dhulikhel, Kavre, Nepal.
Date:

Certificate of Approval

This dissertation entitled **Dynamic Interaction between a Two-Phase Submarine Landslide and a Fluid Reservoir** is submitted for the partial fulfillment of the Master of Philosophy (M. Phil.) Degree in Mathematics to the Department of Natural Sciences, School of Science, Kathmandu University, in March 2014, by Jeevan Kafle.

Approved by

Dr. Shiva P. Pudasaini
(Supervisor)
Professor, Kathmandu University, School of Science
Department of Natural Sciences, Dhulikhel, Kavre, Nepal, and
University of Bonn, Faculty of Mathematical and Natural Sciences
Department of Geodynamics and Geophysics
Meckenheimer Allee 176, D-53115 Bonn, Germany.
Date:

Dr. Dil B. Gurung
(Co-supervisor)
Associate Professor, Kathmandu University, School of Science
Department of Natural Science, Dhulikhel, Kavre, Nepal.
Date:

Dr. Jyoti Upadhaya
Head of Department, Department of Natural Sciences
Professor, Kathmandu University, School of Science, Dhulikhel, Kavre, Nepal.
Date:

Dr. Ranjan Kumar Dahal
(External Examiner)
Associate Professor, Tribhuvan University, Tri-Chandra Multiple Campus, Kathmandu, Nepal
Date:

Acknowledgements

It is my pleasure to thank all those who made this thesis possible. First and foremost, I would like to extend my gratitude and indebtedness to my supervisor Prof. Dr. Shiva P. Pudasaini and co-supervisor Assoc. Prof. Dr. Dil B. Gurung for their inspiration, motivation, supervision and full support. I am indeed grateful to Prof. Pudasaini for his continuous guidance, effort and suggestions which have been very helpful for me to complete this work successfully.

I would like to express my sincere gratitude to the external examiner Assoc. Prof. Dr. Ranjan Kumar Dahal for his interest, valuable time, kind support and the suggestions. I have also been benefited from comments and discussions at various stages of the thesis from my M. Phil. colleagues and especially Mr. Parameshwari Kattel, Mr. Khim B. Khattri and Mr. Puskar R. Pokhrel. I am especially thankful to them, not only for the enriching conversations, but because they have been a wonderful company during this work.

I would also like to thank my wife Durga Sharma Kafle, for standing by my side and helping me in my M. Phil. thesis.

Jeevan Kafle
Kathmandu University Registration Number: 012660-11

Student's Declaration

I, Jeevan Kafle, hereby declare that the research work entitled **Dynamic Interaction between a Two-Phase Submarine Landslide and a Fluid Reservoir** submitted for the partial fulfillment of the Master of Philosophy (M. Phil.) Degree in Mathematics to the Department of Natural Sciences, School of Science, Kathmandu University, Dhulikhel, Kavre in March 2014 is a genuine work that I carried out under the guidance of my supervisors and has not been published or submitted elsewhere for the requirement of any degree programme. Any literature, data or work done by others are cited within this dissertation has been given due acknowledgement and listed in the Bibliography.

_____

Jeevan Kafle
Batch: 2011
Kathmandu University Registration Number: 012660-11

Abstract

Gravitational flows, such as subaerial and submarine landslides, debris avalanches and pyroclastic flows are often the sources of super tsunamis. Here, the general two-phase debris flow model proposed by Pudasaini (2012) is applied to study subaerial and submarine debris flows, and the tsunami generated by the debris impact at reservoirs. The model, which includes three fundamentally new and dominant physical aspects such as enhanced non-Newtonian viscous stress, virtual mass, and generalized drag, constitutes the most generalized two-phase physical-mathematical mass flow model to date. Three-dimensional, high-resolution simulation results are presented in case when a real two-phase debris mass hits a fluid reservoir that consists of different solid concentrations. Simulations are performed for different time slices and different parameter values. An innovative formulation is employed that provides an opportunity, within a single framework, to simultaneously simulate the sliding two-phase debris/landslide, reservoir, debris impact at reservoir, tsunami generation, amplification and propagation, mixing and separation between the solid and fluid phases. The results show formation and propagation of very special solid- and fluid-structures in the reservoir, propagation of the submarine debris mass and turbidity currents, tsunami impacts at coastal lines, and complex interactions between the subaerial, tsunami and submarine debris waves, and reservoir walls. The employed modeling and simulation techniques can adequately describe the dynamics of solid-fluid mixture flows and particle transports in submarine environments, coastal regions, mountain lakes, rivers, reservoirs, and hydroelectric power plants. The simulation results show that the amount of grain in the reservoir plays a significant role in controlling the overall dynamics of the tsunami waves, and submarine debris flow. These findings substantially increase the understanding of three-dimensional complex multi-phase systems and flows and allow for the proper modeling of landslide and debris induced tsunami, dynamics of turbidity currents and sediment transports, with associated applications to engineering and hazard mitigation plans.

List of Symbols

$\mathcal{A}$	mobility number.
b	basal surface of flow.
C_{DG}	generalized drag coefficient.
$\mathcal{C}$	virtual mass coefficient.
f	stands for fluid phase.
$\mathcal{F}$	fluid-like contribution in generalized drag, C_{DG}.
$\mathcal{G}$	solid-like contribution in generalized drag, C_{DG}.
g	gravity constant.
$\mathbf{g}$	acceleration due to gravity.
g^x, g^y, g^z	components of gravitational acceleration.
H	typical height of debris flow.
h	debris flow height, $h = h_s + h_f$.
h_f	fluid contribution to flow height, $h_f = \alpha_f h$.
h_s	solid contribution to flow height, $h_s = \alpha_s h$.
$\mathbf{I}$	identity matrix.
J	exponent for linear or quadratic drag.
K, K_x, K_y	earth pressure coefficients.
L	typical extent of debris flow.
m_f	fluid momentum flux, $m_f = \alpha_f h u_f$.
m_s	solid momentum flux, $m_s = \alpha_s h u_s$.
$\mathbf{M}$	interfacial momentum transfer.
M	a parameter depending on Reynolds number.
N_R	Reynolds number, $N_R = \sqrt{gL}\rho_f H/\alpha_f \eta_f$.
$N_{R_\mathcal{A}}$	quasi-Reynolds number/mobility number.
p	fluid pressure.
$\mathcal{P}$	parameter combining solid-like and fluid-like drag contributions.
p_{b_f}	effective fluid pressure at base.
p_{b_s}	effective solid pressure at base.
Re_p	particle Reynolds number, $Re_p = \rho_f d \mathcal{U}_T/\eta_f$.

$\mathbf{S}$	shear stress.
$\mathcal{S}$	source terms.
s	solid-phase.
t	time.
$\mathbf{T}$	total stress.
$\mathbf{u}_f$	velocity for fluid, $\mathbf{u}_f = (u_f, v_f, w_f)$.
$\mathbf{u}_s$	velocity for solid, $\mathbf{u}_s = (u_s, v_s, w_s)$.
$\mathcal{U}_s$	particle sedimentation velocity.
$\mathcal{U}_T$	terminal velocity of a particle.
$\mathbf{W}$	vector of conservative variables, $\mathbf{W} = (h_s, h_f, m_s, m_f)^t$.
x, y, z	spatial coordinates.
α_f	volume fraction for fluid.
α_s	volume fraction for solid.
$\beta_{x_s},\ \beta_{y_s}$	lateral hydraulic pressure parameters for solid.
$\beta_{x_f},\ \beta_{y_f}$	lateral hydraulic pressure parameters for fluid.
γ	density ratio, $\gamma = \rho_f/\rho_s$.
δ	basal friction angle.
ε	aspect ratio, $\varepsilon = H/L$.
ζ	channel slope angle.
η_f	fluid viscosity.
μ	basal friction coefficient, $\mu = \tan\delta$.
ξ	vertical distribution of α_s.
ρ	debris bulk density.
ρ_s	solid-phase density.
ρ_s	fluid-phase density.
$\boldsymbol{\tau}_f$	extra stress for fluid.
$\boldsymbol{\tau}_s$	extra stress for solid.
ϕ	internal friction angle.
χ	vertical shearing of fluid velocity.
∇	gradient operator.
$\otimes$	tensor product.

Publications

A. Published Papers

1. Kafle, J., Kattel, P., Pokhrel, P. R., Khattri, K. B., Gurung, D. B., Pudasaini, S. P., 2013: Dynamic Interaction Between a Two-Phase Submarine Landslide and a Fluid Reservoir. *Int. J. Lsld. Env.* 1(1), 35-36.

2. Kattel, P., Kafle, J., Khattri, K. B., Pokhrel, P. R., Gurung, D. B., Pudasaini, S. P., 2013: Dynamic,s of Three-Dimensional, Two-Phase Landslides and Debris Flows. *Int. J. Lsld. Env.* 1(1), 39-40.

3. Khattri, K. B., Pokhrel, P. R., Kafle, J., Kattel, P., Gurung, D. B., Pudasaini, S. P., 2013: Some New Insights into the Fluid Flows in Debris Material and Porous Landscape. *Int. J. Lsld. Env.* 1(1), 43-44.

4. Pokhrel, P. R., Khattri, K. B., Kattel, P., Kafle, J., Gurung, D. B., Pudasaini, S. P., 2013: Enhanced Descriptions of Real Two-Phase Landslides and Debris Flows. *Int. J. Lsld. Env.* 1(1), 75-76.

B. Submitted Papers

1. Kafle, J., Kattel, P., Pokhrel, P. R., Khattri, K. B., Gurung, D. B., Pudasaini, S. P., 2013: Dynamic Interaction Between a Two-Phase Submarine Landslide and a Reservoir.

2. Kattel, P., Kafle, J., Khattri, K. B., Pokhrel, P. R., Gurung, D. B., Pudasaini, S.P., 2013: Dynamic Simulation of Three-dimensional, Two-phase Landslides and Debris Flows.

3. Pokhrel, P. R., Khattri, K. B., Kattel, P., Kafle, J., Gurung, D. B., Pudasaini, S. P., 2013: Real Two-Phase Landslides and Debris Flows: Enhanced Simulations.

Presentations

1. Kafle, P., 2013 : *Mathematical modelling and simulation of dynamic interactions between a two-phase submarine landslide and a fluid reservoir*
   In: The DAAD Partnership Activities Workshop organized by Department of Natural Sciences, School of Science, Kathmandu University on "Numerical Methods for Ordinary and Partial Differential equations", September 2-13, 2013, Kathmandu University Dhulikhel, Kavre, Nepal.

2. Kafle, J., Kattel, P., Pokhrel, P. R., Khattri, K. B., Gurung, D. B., Pudasaini, S. P., 2013: *Dynamic interaction between a two phase submarine landslide and a fluid reservoir.*
   In: The 11th International Symposium on Mitigation of Geo-disasters in Asia (MGDA-11), 22-28 October, 2013, Kathmandu and Pokhara, Nepal.

3. Kattel, P., Kafle, J., Khattri, K. B., Pokhrel, P.R., Gurung, D. B., Pudasaini, S. P., 2013: *Dynamics of three-dimensional, two phase landslides and debris flows.*
   In: The 11th International Symposium on Mitigation of Geo-disasters in Asia (MGDA-11), 22-28 October, 2013, Kathmandu and Pokhara, Nepal.

4. Khattri, K. B., Pokhrel, P. R., Kafle, J., Kattel, P., Gurung, D. B., Pudasaini, S. P., 2013: *Some new insights into the fluid flows in debris material and porous landscape.*
   In: The 11th International Symposium on Mitigation of Geo-disasters in Asia (MGDA-11), 22-28 October, 2013, Kathmandu and Pokhara, Nepal.

5. Pokhrel, P. R., Khattri, K. B., Kattel, P., Kafle, J., Gurung, D. B., Pudasaini, S. P., 2013: *Enhanced descriptions of real two phase landslides and debris flows.*
   In: The 11th International Symposium on Mitigation of Geo-disasters in Asia (MGDA-11), 22-28 October, 2013, Kathmandu and Pokhara, Nepal.

6. Kafle, J., Kattel, P. , Pokhrel, P. R., Khattri, K. B., Gurung, D. B., Pudasaini, S. P., 2014: *A two-phase, 3D subaerial debris-flow impinging a reservoir: Dynamics of induced tsunami and submarine debris flows.*
   In: The 5th National Conference of Mathematics (NCM-2014), Nepal Mathematical Society, January 28-30, 2014, Surkhet, Nepal.

7. Kattel, P., Kafle, J., Pokhrel, P. R., Khattri, K. B., Gurung, D. B., Pudasaini, S. P., 2014: *Physical-mathematical modeling and high-resolution simulations of a real two-phase, three dimensional debris flow dynamics.*
   In: The 5th National Conference of Mathematics (NCM-2014), Nepal Mathematical Society, January 28-30, 2014, Surkhet, Nepal.

8. Khattri, K. B., Pokhrel, P. R., Kafle, J., Kattel, P., Gurung, D. B., Pudasaini, S. P., 2014: *Some exact and numerical solutions for fluid flows in debris and porous media with sub-diffusive and sub-advective Model.*
   In: The 5th National Conference of Mathematics (NCM-2014), Nepal Mathematical Society, January 28-30, 2014, Surkhet, Nepal.

9. Pokhrel, P. R., Khattri, K. B., Kattel, P., Kafle J., Gurung, D. B., Pudasaini, S. P., 2014: *General phase-eigenvalues for two-phase mass flows and their implications in enhanced simulations.*
   In: The 5th National Conference of Mathematics (NCM-2014), Nepal Mathematical Society, January 28-30, 2014, Surkhet, Nepal.

List of Figures

Contents

Chapter 1

Introduction

1.1 Essence of Advanced Study of Submarine Landslides

Subaerial and submarine landslides and debris flows are effectively two-phase flows of solid particles mixed with fluid and are very important sediment transport mechanisms. Examples include, sediment transport in hill slopes, in hydraulic reservoirs and channels, and submarine environments. From the environmental and industrial point of view advanced knowledge of the evolution of the solid and fluid-phases are very important including the huge landslides in the coastal areas and particle transport in hydraulic plants [99]. Submarine landslides are commonly observed huge mass wasting processes. They constitute one of the most important mechanisms for sediment movement from shallow to deep marine environments, and in shaping continental margins. Examples include Mauritania Slide Complex, which is one of the largest events on the Atlantic margin (area $\sim$ 30,000 km^2, volume 600 km^3, run-out 300 km; Antobreh and Krastel, 2007 [2]; Henrich et al., 2001 [39]; Foerster et al., 2010 [24]). Another important scenario is the subaerial debris flows hitting the fluid environments [99], e.g., the large 3700 B.P. Eibsee rock-ice avalanche (4×10^8 m^3 in volume) in Zugspitze (where the rock-ice avalanche plunged into Eibsee) entrained water and lake sediment and largely turned into a debris flow. This could have generated water waves (tsunami) in the Eibsee (lake) and the subsequent debris flood.

Although recently research has been focused towards evaluating the landslide-induced tsunami generation and risks (Haugen et al., 2005) [38], not much is known about tsunami deposits. There is a direct threat to submarine installations, including oil platforms, pipelines, cables, and wind installations. These offshore resource exploitations and constructions require detailed hazard assessments for engineering and environmental projects.

Therefore, the societal interest is increasing on mapping, modeling and simulation of submarine landslides [99].

This dissertation focuses on the simultaneous dynamic simulation of an idealized three-dimensional and two-phase subaerial debris flow, the resulting tsunami generation and propagation upon debris impact at the reservoir, the subsequent submarine debris flow along the reservoir basin, and the entire analysis of all three types of waves and their complex interactions. To do so, a generalized two-phase debris flow model (Pudasaini, 2012) [98] will be applied and simulated together with a high resolution shock capturing scheme.

1.2 Problem Statement

Due to geophysical, geological, geotechnical, environmental and cultural importance, considerable attention has been drawn in the past to investigate the mechanism of slope failure and movements, material properties, modeling, numerical simulations, debris impact, tsunami generation, inundation, and associated mitigation strategies [99]. Examples include the 1958 Lituya Bay Megatsunami (Alaska) generated by an earthquake-induced landslide and the 1963 Vajont landslide (Italy) induced megatsunami (Miller, 1960 [82]). However, due to multiple complexities, these events are still poorly understood in terms of dimensions, phases and mechanics [99]. Debris flows and induced super tsunamis are extremely destructive and dangerous natural hazards (Tinti et al., 2005 [125]; Weiss et al., 2009 [127]). So, there is a significant need for reliable methods for predicting the dynamics, the runout distances, and the inundation areas of such events as well as prevention and reduction of such disasters including their socio-economic aspects. On the one hand, existing studies mainly concentrate on the description of the slide and depositional processes (Foerster et al., 2010 [24]). On the other hand, modeling and simulation of tsunami triggered by landslides, run-ups, and inundation is still an emerging field and different modeling approaches may lead to very different results (Pudasaini, 2012 [98]; Pudasaini and Miller, 2012a and 2012b [106, 107]).

The real two-phase debris mass flows were simulated by Pudasaini (2012, 2014) [98, 99] and by Pudasaini and Miller (2012a, b) [106, 107] for the explicit evolution of the solid and the fluid volume fractions as the debris mass collapses and slides down the slopes, for both the subaerial and submarine debris flows. A detailed analysis of the geometrically two-dimensional, two-phase subaerial debris flows impacting a two-dimensional reservoir, tsunami generation and propagation of the surface tsunami waves and submarine land-

slides have been presented previously [99, 107]. This dissertation analyzes in detail on how a three-dimensional and two-phase subaerial debris mass penetrates a fluid reservoir, generates tsunami, and finally how it moves and deposits on bottom of the reservoir basin.

1.3 Aim and Objectives

This dissertation aims to advance further by primarily focusing on the complex dynamics of a two-phase subaerial debris flow sliding down an idealized three-dimensional surface plunging into a quiescent fluid reservoir with different solid concentrations with particular emphasis on the dynamics of the submarine debris flow with respect to the available and changing volume fraction of the solid in the reservoir. Another important aspect of the simulation is to investigate the complex interactions between the internal submarine debris wave and the surface tsunami and their dynamic impacts in the coastal lines, and the reservoir dams.

The simultaneous dynamics of the two-phase, geometrically three-dimensional subaerial debris flow, the resulting tsunami generation and propagation upon debris impact at a fluid reservoir or a lake, the subsequent submarine debris flow, and the analysis of all three types of waves and their complex interactions will be studied here by applying a generalized two-phase debris flow model (Pudasaini, 2012) [98].

Particularly, the mechanism of complex wave generation and interactions between the solid and the fluid phases in the reservoir and lakes will be analyzed. The generation, amplification and propagation of super tsunami waves, debris flows at the bottom floor, particle transport in hydraulic channels, and the integrity of hydroelectric power plants will be focused. These basic three-dimensional, two-phase simulation results presented here for subaerial debris flows impacting a reservoir and thus generating tsunami waves, and the complex interactions between the submarine debris wave and the tsunami wave, to date, have not been available for geometrically three-dimensional, real two-phase flows.

1.4 Research Methodology and Approaches

1.4.1 Simulations of Landslide Induced Tsunamis/Submarine Debris Flows

Lynett and Liu (2002) [74] developed a mathematical model to describe the generation and propagation of submarine landslide generated water waves. It consists of a depth-

integrated continuity equation and momentum equations which include full nonlinear, but weakly frequency dispersion effects. Two main differences between the tsunami generation mechanism of a submarine landslide and a submarine earthquake was pointed out in this model:

(i) the duration of a landslide is much longer, indeed the time history of the sea floor movement will affect the characteristic of the generated wave, and cannot be considered just as an initial impulsive condition.

(ii) the typical wavelength of the tsunami generated by landslide is shorter, therefore, the frequency dispersion could be important even in the wave generation region.

1.4.2 Advanced Mathematical Model and Numerical Method

The correct description of these waves near the source is the key to the accurate modeling and prediction of tsunami propagation, resulting coastal hazard, and eventual mitigation. This elevated awareness of the need for better understanding of submarine landslides is coupled with great advances in submarine mapping, sampling and monitoring technologies. Great advances in numerical simulation techniques of submarine landslide kinematics and tsunami propagation, have also lead to increased understanding and predictability of submarine landslide consequences [9, 34, 107].

Subaerial and submarine debris flows are multiphase, gravity-driven flows consisting of a broad distribution of grain sizes mixed with fluid. The rheology and flow behavior varies depending on the sediment composition and the percentage of solid and fluid phases [98]. Research in recent years focused on different aspects of single- and two-phase debris avalanches and debris flows and induced tsunami (see, e.g., Pudasaini, 2014 [99]), which was recently advanced by Pudasaini (2012) [98] with a comprehensive theory that accounts for interactions between the solid and the fluid. The model, which includes buoyancy, also includes three new and important dominant physical aspects of solid-volume-fraction-gradient-enhanced non-Newtonian viscous stress, virtual mass, and generalized drag. The two-phase model has been applied to simulate flows of debris mixture sliding down an inclined channel that extends to the horizontal run-out (Pudasaini, 2012 [98] ; Pudasaini and Miller, 2012a, 2012b [106, 107]).

Here, to simulate the dynamic interaction between a three-dimensional and two-phase submarine landslide and a fluid reservoir, the two-phase physical-mathematical model (Pudasaini, 2012) [98] will be employed and solved numerically together with the widely applied and well-validated high-resolution shock-capturing numerical scheme, namely, the

Total Variation Diminishing (TVD) Non-Oscillatory Central (NOC) Scheme (Pudasaini, 2012 [98] ; Pudasaini and Miller, 2012a, 2012b [106, 107]). Such an innovative and unified approach allows for the adequate modeling of debris induced tsunami and submarine sediment transport.

1.5 Expected Outcome and Implications

The results obtained in this dissertation will demonstrate that the general two-phase debris flow model [98] is able to adequately describe the complex dynamics of three-dimensional and two-phase subaerial debris flows; particle-laden and dispersive flows; sediment transports; debris induced tsunamis and submarine debris flows; turbidity currents and associated sophisticated phenomena including the solid and fluid waves and their complex interactions and dynamic impacts. It will be shown that the amount of solid grains in the reservoir plays a significant role in controlling the overall dynamics of the submarine debris flow and the tsunami wave. This novel result can be used to generate early warning signals in coastal regions, and also to prevent possible catastrophic dam collapses, e.g., the hydro-power dam prone to be hit by landslides. Furthermore, total impact force in the reservoir dam can be calculated with the help of solid and fluid velocities, and the evolving phase-densities for the solid and the fluid phases. The findings add substantial and fundamental values for the dynamical understanding of complex multi-phase systems and flows, proper modeling of run-out distances, geomorphological interpretation of past events, and hazard prediction and mitigation in debris-flow and debris avalanche prone mountain slopes. These results indicate potentially wide applicability of the model to a variety of two-phase geophysical mass flows, including particle-laden and dispersive flows, sediment transport, and debris flows [40, 99, 107]. Broadly speaking, the results can find applications in sedimentology, submarine geodynamics, the integrity of hydroelectric power plants, and hazard mitigation.

Some simulation results related to our work can also be found in Kafle et al. (2013) [58] and Kafle et al. (2014) [59]. More advanced simulations with more complex eigenvalues of the model system, geometrically three-dimensional simulation results for flows of a real two-phase debris material down an inclined surface and some exact solutions to reduced model can be found in Pokhrel (2014) [94] and Pokhrel et al. (2013, 2014) [95, 96]; Kattel (2014) [60] and Kattel et al. (2013, 2014) [61, 62]; Khattri (2014) [64] and Khattri et al. (2013) [65] respectively.

1.6 Thesis Structure

Chapter 2 provides a general introduction to two-phase debris flows and tsunamis. In Chapter 3, physical-mathematical model for landslide, debris flow and tsunami will be presented. Chapter 4 explains two-dimensional high-resolution numerical simulation method. Numerical simulation results for geometrically three-dimensional subaerial and submarine two-phase debris flows impacting reservoirs and thus, generating tsunami waves are presented in Chapter 5. Detailed discussions on the simulation results are also presented in Chapter 5. Finally, Chapter 6 contains the summary of this work.

Chapter 2

Two-Phase Debris Flows and Induced Tsunamis

2.1 Submarine Debris Flow and Tsunami

Subaerial and submarine landslides and debris flows are very dangerous sediment transport events. Sediment transport in hill slopes, in hydraulic channels and submarine environments are some examples of subaerial and submarine mass movements [1, 23, 24, 27, 38, 73, 77, 82, 83, 99]. These mass movements are effectively two-phase flows as a mixture of solid particles and the viscous fluid [93, 97, 98, 103, 108]. Precise knowledge of the evolution of the solid and the fluid-phases are very important from both the environmental and industrial prospective. Examples include the huge landslides and debris flows in the coastal and mountain regions, and particle transport in fluids such as the mountain lakes, rivers, reservoirs and hydro-electric power plants [106, 107]. The information of submarine debris wave speed can be useful for the design of early warning strategies in the coastal regions [99].

Firstly, introduction of the tsunami trigger, types, and impacts are briefly discussed. Tsunami generated by landslides and debris flows are another aspect of discussion. With reference to the landslides and debris flows, mountain lakes, and artificial reservoirs, some aspects of tsunami scenarios and hazards in Nepal are presented. Then, with a few examples of related hazards from Nepal, some protection and mitigation measures against landslides and debris flows are mentioned. As a very quick introduction of the state of the art of the field, different and influential modeling approaches are mentioned for geophysical mass flows, including the single-phase models, quasi two-phase models, two-phase models, and a general two-phase mass flow model. Finally, a need of advanced dynamic

simulations of landslide induced tsunami and submarine debris flows are presented briefly with a general two-phase mass flow model.

2.2 Tsunamis: Triggers, Types and Impacts

The word tsunamis comes from the Japanese, with the meaning "harbor wave". The tsunamis are long water waves triggered by a sudden disturbance of the floor or surface of ocean, sea or lakes, which is generally caused by earthquakes, volcanic eruptions, or landslides. When long wave tsunamis enter the harbor, this causes the excitation of the water body, called seiches [9]. The same phenomenon occurs when a landslide impacts a closed lake or a fluid reservoir or a fjord. Both energy and momentum can take tsunami waves thousands of kilometers across the open ocean, carrying destructive power on far shores hours after the impulse generating event, such as the devastating 2004 Indian Ocean tsunami[1]. In deep water conditions, tsunamis can travel at celerities of 400-500 kmh^{-1}, or even faster, because, in simple situation the wave celerity is given by $c = \sqrt{gH}$, where g is the gravitational acceleration and H is the ocean depth, say 6000 m [9]. The wave heights can be on the order of some meters, and the wavelengths of the order of hundreds of kilometers [9, 34]. Sometimes there appears to be just one wave but often there are multiple waves traveling a few to possibly several minutes apart. Tsunamis can produce high wave run-ups sufficient to flood around the coastal areas far beyond the coastal line thereby threatening the coastal population and destroying the coastal cultivation and infrastructure[2].

Tsunami Generated by Seismicity and Landslides: The seismic and landslide induced tsunami generation mechanisms are fundamentally different. There are two main differences between tsunami waves triggered by landslides and by seismic displacements of the sea floor. A landslide takes more time to stop its movement, on the order of several minutes longer, as compared to the sea floor seismic motion [1, 9]. The other difference is in the source area involved in a seismic floor deformation which is larger than that of an area covered by a (submarine) landslide movement initiation. Tsunami hazard is usually limited to the near-field generation area, in terms of coastal run-up, in view of typical slide volumes [1]. The volcano collapses involving huge volumes (on the order of hundreds of km^3 of material) have occurred in the past that could have the potential of triggering tsunamis large enough to strike coasts far away from the generation area, even over transoceanic distances [1].

[1] www.abc.net.aunews2013-06-18...india-monsoon-floods4763808.

[2] http:/earthobservatory.nasa.govNaturaslHazardsview.phd?id=78117.

Tsunami occurs when there is a sudden large displacement of water. There are three main causes of tsunami generation: seismic activity, subaerial and submarine landslides, and asteroid impacts. Seismic activity is the most common cause of tsunamis. Both tectonic and subduction earthquakes in and near the ocean may create tsunamis [1, 9, 111]. During a tectonic earthquake, the sea floor becomes deformed, forcing a displacement of water. In a subduction earthquake, tectonic plates slip against each other, creating a disturbance, and resulting in a massive displacement of water. Submarine landslides can also cause tsunamis. Submarine landslides occur during earthquakes and the explosion or implosion of underwater volcanoes. In case of subaerial landslide, the debris mass can also trigger massive water movement when the landslide impacts a fluid body, resulting in a tsunami. Tsunamis from asteroid and comet impacts in the ocean are less frequent.

2.3 Tsunamis Generated by Landslides and Debris Flows

Gravitational flows like submarine and subaerial landslides, debris avalanches and pyroclastic flows from volcanoes are frequently reported as the sources of tsunami waves. The catastrophic landslides impacting ocean coast, sea, rivers and more restricted water bodies, such as lakes, fjords, or artificial reservoirs can induce very dangerous tsunamis, which are a particular type of tsunami waves, called mega tsunami [1, 9, 12, 28, 29, 63, 82, 83, 99, 107]. The landslide tsunamis are water waves created by mass flows, either initiated underwater or subaerial. Some major geophysical mechanisms that are responsible for landslide related tsunami generations are submarine landslides, or slumps, rock/debris flows and pyroclastic flows [1]. In contrast to tsunami waves triggered by a submarine landslide, the subaerial landslides produce splashes and complex three dimensional water flows in the vicinity of the landslide impact area [1, 9, 58, 82].

In general, landslide tsunamis are related to the vertical displacement of the landslide, which may reach several thousand meters. Submarine mass movements represent major offshore geo-hazards due to their destructive and tsunami-generation potential. This potential possesses a threat to human life as well as to coastal, near shore and offshore engineering structures [99, 107]. There is a direct threat to submarine installations, including oil platforms, pipelines, cables, and wind installations. These offshore resource exploitations and constructions require detailed hazard assessments for engineering and environmental projects [99]. Oil industries, hydrocarbon exploration, and production activities have recently been moved further into deep water (Krastel et al., 2006 [68],

Geersen et al., 2011 [27]). The further interest in studying submarine slides is because of capability of slides to modify the architectural and sedimentological characteristics of submarine channels and levees as they are often connected to potential deep sea hydrocarbon reservoirs (Antobreh and Krastel, 2007 [2]). Therefore, the societal interest is increasing on mapping, modeling and simulation of submarine landslides [24, 99, 107].

So, understanding the dynamics of landslide tsunamis are very important both for the safety of lives and the infrastructures near the potential impact areas, and also for the construction of the artificial reservoirs in the mountain and valleys as the reservoir dams must withstand the worst possible scenarios of the wave dynamics and their impacts at the dam walls and embankments [99]. One prominent example is the Three Gorges Reservoir in China (see, Fig. 2.1).

The Three Gorges Reservoir (TGR) in China is an area that includes a large number of landslides and also susceptible to impacts by landslides (Fig. 2.1). TGR is the largest artificial reservoir with capacity of running the largest hydro-electric power generation ($22,500$ MW) plant worldwide. Especially, the landslides developed in Jurassic stratum [81]. The behavior of the slow-moving landslides in the Jurassic red-strata has recently been analyzed by Miao et al. (2014) [81]. It was discovered that there are two differing processes in all landslides that took place in TGR [81]. They are: sliding process with variable shear speeds of soils within the sliding zone and in the steady state with different durations. It was revealed that the shear strength is positively dependent on the shear rate and can be recovered within short time after the ceasing of shear and this can reduce the reactivation of landslide. Also, the landslide in this area shows delay response to the rainfall or fluctuation of water level in the reservoir. This indicates the importance of the detailed and advanced study of the subaerial landslides and debris mass impacting the reservoir, waves generation and their impacts to the stability of the embankment and reservoir walls and dams [58, 99, 107].

Different Phases of Landslide Induced Tsunami: The phenomenon of generation of tsunami waves due to the impact of subaerial landslide into water is very complex, with several different physical aspects. It can be understood in four different phases [99, 107]:

(i) The landslide starts moving, accelerates and then enters into water.

(ii) Then, the landslide impacts the water body. This is the cause of the impulsive wave generation, due to the energy exchange mechanism between the landslide material and the water. This results in a hydrodynamic impact vacuum, or crater (see, e.g., Mohammed and Fritz, 2010 [84]; Pudasaini and Miller, 2012b [107]; Pudasaini, 2014

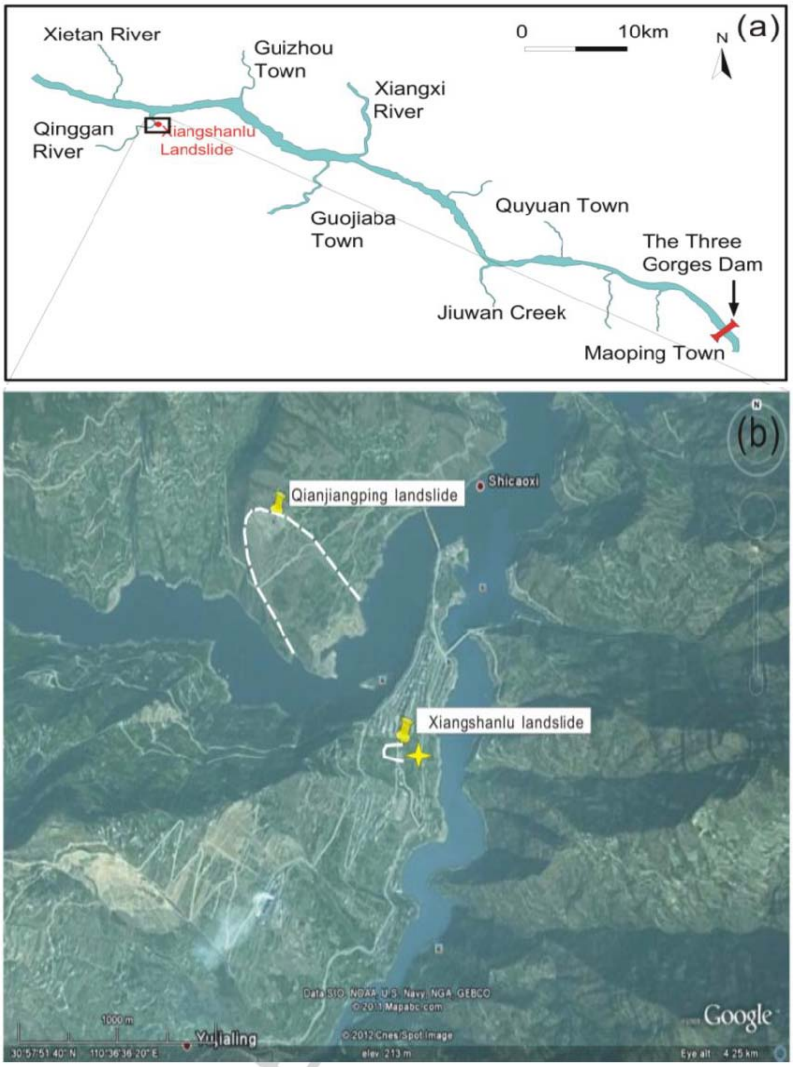

Figure 2.1: Xiangshanlu landslide (as indicated by yellow asterisk) nearby Qianjiangping landslide, which occurred on July 14, 2003, 22 people died. (a) Location of the landslide in Three Gorges Reservoir; located on the left bank of Tongguluo River. It has covered an area of 3.3×10^4 m^2. The landslide volume has been estimated to be 1.56×10^5 m^3. (b) The details of landslide locations (Images from Miao et al., 2014 [81]).

[99]). The volume, impact velocity, density of landslide mass, shape of the front, and slope inclination angle are some important parameters associated with the landslide that influence the characteristic features of the water wave generation and motion.

(*iii*) The waves propagate into the reservoir, or in the open sea, presenting a wave energy dispersion which is in longitudinal, crosswise and vertical directions.

(*iv*) Finally, impulsive wave run-up may cause the severe damage of coastal areas by flood and inundation whereas, in the case of the mountain lakes and artificial reservoirs

(Fig. 2.1), the dam can be overtopped thereby flooding the downstream areas, or the dam may break due to unprecedented wave impact onto the reservoir dam walls [99, 107]. This may produce catastrophic debris flows, hyper-concentrated floods, and mud flows in the downstream [61].

Thus, landslide tsunami generation includes processes of debris or landslide initiation (or, triggering), its motion, interaction with water, and induced water surface deformation, including the possible wave breaking [99, 107]. These mass flows depend strongly on the material properties as well as on site geometry [1].

2.4 Mountain Rivers, Lakes and Reservoirs: Tsunami Scenarios and Hazards in Nepal

Debris and mud flows are multiphase, gravity driven flows consisting of randomly dispersed interacting phases. In the geophysical context they consist of solid components with different grain size and shape mixed with liquid. Landslides, debris flows, tsunamis, are some examples of mass flows in nature whereas similar mass flows take place in pharmaceutical and agricultural industries [103]. Debris flow, is a frequently happening phenomenon in mountainous regions, occurs when masses of loose and poorly sorted sediments, rocks and fine material are agitated, breaks off, and mixed with water. The flow surges down slopes in response to gravity force, and further be mixed with water that may turn it into a debris flood [76, 86]. A typical surge of debris flow may have a steep front or a leading head with the densest slurry with the highest concentration of boulders and the greatest depth. A progressively more dilute and shallower tail follows this head [53, 76, 108]. However, which part of the debris flow behaves more like a solid and which part behaves more like a fluid depends on many dynamical aspects and flow configurations, including the initial and boundary conditions, topography, initial amount of the solid and the fluid, and how the solid (or fluid) evolves during the motion [98, 106, 107].

Being a mountainous country, Nepal is frequently hit by catastrophic avalanches, landslides and debris flows, mainly during the Monsoon season. The most recent and detrimental debris flow events in Nepal is the detachment and collapse of the rock-ice wall in the Mount Annapurna IV in the West Himalaya in Nepal, and the subsequent landslide and avalanche on May 5, 2012. This developed into a fluidized debris flow, and finally turned into a debris flood and mud flow when it plunged into and mixed with the Seti River, Pokhara valley, in Kaski District, Nepal, Fig. 2.2. The catastrophic flood traveled nearly about 20 kilometers in about 35 minutes and it took away the lives of 71 people.

Figure 2.2: The bank of the Seti river in Kharapani, Kaski District, Pokhara valley in the west Nepal, after the destruction by the debris flood on 5th May, 2012. On the left bank there remains a substantial deposition of the debris mass (Photo: Field excursion during the symposium, MGDA-11).

This flow produced tens of devastating surges of debris floods.

However, we have been alarmed of many similar disasters in future by this particular disaster. It may happen in any other parts in Nepal, and in the Himalayas, in the Alps, Rockies, or the Andes. The phenomena involved in this type of debris flow and flash flood have not only created a keen interest in the scientific community for the purpose of understanding these complex, dangerous, and disastrous natural events in the high and lesser Himalayas, but also for the purpose of understanding the catastrophe mechanisms and mitigations of the potential future losses in similar hazardous zones in Nepal and the Himalayas. In the context of Nepal, the research on the dynamics of landslides, avalanches, debris flows, debris floods, mud flows, and flash floods, are very relevant [7, 103]. The recent *11th International Symposium on Mitigation of Geo-disaster in Asia (MGDA-11) held in Kathmandu and Pokhara from 22nd-28th October, 2013, Nepal*, has highlighted the increasing need for the relevant fundamental, scientific and technological research in the Himalaya.

Glacial lakes are potentially dangerous sources of glacial lake outburst floods. A Glacial Lake Outburst Flood (GLOF) is a sudden release of a huge amount of water, many orders of magnitude higher than the normal flow, from a lake formed at the snout of a glacier due to a breach of the moraine dam [19]. Glacial lakes are of two types: Supra-glacial lakes

Figure 2.3: Dig Tsho glacial lake in western part of the Sagarmatha National Park, Khumbu Himal, Nepal. The Dig Tsho GLOF event of 4th August, 1985, occurred when an ice avalanche hit the glacier surface and suddenly fell into the lake [46].

and Clean-ice glacial lakes [46]. Supra-glacial lakes form on the glaciers' surface which are almost covered by huge debris mass which are either moving very slowly or completely stagnant. Clean-ice glacial lakes are formed on the steeply sloping glaciers which have very less debris on the surface. The large glacier lakes in Nepal are Tsho Rolpa, Imja Tsho and Thulagi Lake. These lakes began to form about 50 to 60 years ago at the same time [46].

In Nepal, till the sudden outburst of the Dig Tsho Lake in the 4th August, 1985, there was no enough attention drawn towards this type of potential phenomenon. The Dig Tsho is a glacial lake in western part of the Sagarmatha National Park, Khumbu Himal, Solukhumbu, Nepal, which is formed by the end moraine of Langmoche glacier (see, Fig. 2.3). The Bhote Koshi river receives the meltwater of the Dig Tsho [46]. The Dig Tsho GLOF event occurred when it was triggered by an ice avalanche that hit the glacier surface and suddenly fell into the lake. This sudden outburst destroyed the nearly completed Namche Small Hydroelectric Project and 14 bridges causing more than $3 million worth of damage and disrupted the downstream community for several months. Though it was one of the smaller clean-ice glacier lakes, it showed that even small glacial and mountain lakes may be dangerous [46].

Glacial lake outburst floods and related debris flows represent a serious threat of natural catastrophe in high mountainous areas across the globe [4, 19, 26]. Consequently, assessing

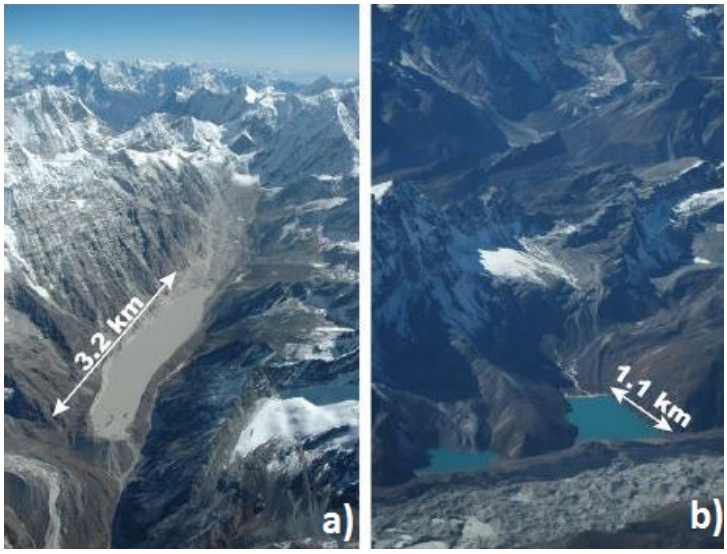

Figure 2.4: Glacial lakes and their potential hazards in Nepal: **a**) Tsho Rolpa, a moraine-dammed lake, and **b**) Gokyo Tsho, a glacier dammed lake in November 2007 [26].

the likely risk of a GLOF from individual glacial lakes is also essential. Though detailed in situ surveys are able to figure out the potential of outburst flooding from individual glacial lakes (Fujita et al., 2008 [25]; Reynolds, 1999 [109]), it is impractical to perform such ground-based investigations, on the hundreds of Himalayan glacial lakes. In Nepal, glaciated mountains may be highly susceptible to the climatic changes and impose great threats to the downstream population and settlement. Nepal has experienced 24 events in the recent past and many of them have damaged lives and physical infrastructures, e.g., the Bhote Koshi Sun Koshi GLOFs of 1964 and 1981 and the Dig Tsho GLOF of 1985 [46]. In particular, 44 glacial lakes in Bhutan and Nepal have been identified as potentially dangerous glacial lakes. In addition to the studies evaluating GLOF probability, risk assessment is also an important aspect for the GLOF-relevant research. GLOF is responsible for huge loss of lives and physical properties [4, 91, 116, 117, 129][3,4].

One of the most popular lakes which has high risk of GLOF in Nepal is Tsho Rolpa lake situated in Dolakha District, in the eastern part of Nepal at an altitude of 4580 m from sea level, has drawn attention for its potential outburst [46]. The lake is an example of moraine-dammed lake (see, Fig. 2.4**a**) that has been formed due to the glacial melting

[3]IPCC, Climate change 2007 synthesis report. In: Pachauri, R.K., Reisinger, A. (Eds.), Contribution of Working Groups I, II and III to the Fourth Assessment Report of the Intergovernmental Panel on Climate Change. IPCC, Geneva, 104 pp.

[4]G. Rees: Glaciar retreat and glacier lake outburst floods in the Himalaya: WATCH-HighNoon Open Science Seminar Future of water resources in India under a changing climate 13-14 May 2009.

Figure 2.5: Imja Tsho lake, Mt. Ambulapcha is seen in the background [46].

in the Himalayas over the last 50 years. It is the only glacial lake in Nepal that has been subjected to mitigation measures of the possible damages or adverse consequences. Canals had been constructed for removing water from the river at the rate of 6000 liters per second, and this rate is slowly being increased. A total of 17 sirens have been placed in appropriate areas, to warn people of the danger of the lake burst[5]. Over the last decade, the expansion of Tsho Rolpa is minimal but Imja Tsho has remarkably expanded. Similarly, Gokyo Tsho is an example of glacier-dammed lake (see, Fig. 2.4**b**) [46].

Imja Tsho is one of the large glacier lakes which is located in the eastern Nepal Himalayas, Solukhumbu District of Nepal. It has formed on the lower tongue of the Imja Glacier, south of Lhotse and Island Peak (see, Fig. 2.5). It is drained through the end moraine that forms the lake dam by the Imja Khola, one of the main tributaries of the Dudh Koshi river [46].

Thulagi Lake is another large glacial lake which is situated in Manang district, at the end of the Thulagi Glacier to the southwest of Mount Manaslu in the headwaters of the Dona Khola, a tributary of the Marsyangdi river. Several hydropower projects are planned downstream of it in the Marsyangdi river basin. So, it has drawn much attention in the recent year. Two projects, the Marsyangdi Hydropower Project in Tanahun district and the Middle Marsyangdi Hydropower Project in Lamjung district, have already been commissioned and an Upper Marsyangdi Hydropower Project there is in the planning stage [46]. Thulagi Lake started to form about 50 years ago when small supra-glacial lakes

[5]http:/nepalitimes.comnews.php?id=11629#UqB_uSeKm1s.

Figure 2.6: Overview of Thulagi Glacier and glacial lake in 1992 (left) and 2009 (right); the red line shows expanded area by glacier melt [46].

began to enlarge and coalesce (Fig. 2.6). Now, it is more than 2 km long. It is a long, debris-covered glacier with a 40 m high cliff [46].

There are hundreds of big mountain rivers, lakes, high Himalayan glacial lakes, and several artificial reservoirs created for the hydro-electric power generation plants in Nepal, and also in other parts of the Himalayas [91, 117, 129]. These may severely be hit by the sudden breaking off of the large hanging glaciers, landslides, debris flows and rock-slides, thereby triggering glacial lake outburst floods, and tremendous water waves, debris flows and mud flows that rapidly cascade the steep mountain torrents as the *Mountain Tsunami*. Devastating mountain tsunamis and associated debris surges have been witnessed in the Badrinath-Kedarnath area in the North-West state of Uttarakhanda, India during the 2013 Monsoon season[6]. Another catastrophic flash flood has recently devastated the Seti river in Kaski District, Pokhara, Nepal on 5th May, 2012.

These and similar flows in future, may penetrate mountain lakes, reservoirs and rivers, then turn into submarine landslide and debris flows. When the mixing with water is intense, they become particle transporting floods, and sediments are transported in and by water [98, 99, 107]. These events may severely damage environments, water supply and aquatic systems, and hydro-electric power generating plants. One example is the erosion on the power generating turbine in the Chilime Hydropower plant in Rasuwa District,

[6]www.abc.net.aunews2013-06-18...india-monsoon-floods4763808.

Figure 2.7: Ghatta house (left) and Ghatta (right): Traditional water mill for grinding grain made in local level near Sunkoshi River, whose Nepali name is Ghatta, the massive runner stone disc. Water is diverted from a stream or river and flows down a rectangular chute called dunde, towards the Ghattas turbine, called *Madani*. The vertical shaft of the turbine runs in the vertical direction through the floor of the ghatta house and horizontally rotates the upper runner stone of a pair of grinding stones. Grain is stored above the runner stone in the hanging silo and exits out through a feeder mechanism at the bottom of the silo in a control manner into a central hole of the upper runner stone, and is then grund between the pair of stones (Photo: Field excursion during the symposium, MGDA-11).

Central Nepal Himalaya[7].

Not only the modern industrial facilities are affected, more often and largely so are the traditional grinding mills (called *Ghatta*, the massive runner stone disc, Fig. 2.7) that are still widely used in the rural areas in Nepal to produce flour, e.g., from corn, wheat, and millet grains and other cereals[8]. Ghatta turbine, called *Madani*, that rotates in a horizontal plane, is a Kaplan type. The rotational energy of a Ghatta is also being used as a battery charging station. Such a renewable energy source has the potential to bring electrical lighting to the many parts of the Himalayas that remain unelectrified[9]. Water-powered mills are commonly used in agro-processing and small scale hydroelectricity. According to Nepals Center for Rural Technology (CRT), over 25,000 of these water mills (Ghattas) are operating throughout remote Nepal. Traditionally such power is only

[7]floodlist.comasianepal-july-2013-update.

[8]L. K. Shrestha, G. R. Shrestha, and R. Munankami. Improving traditional water mills. LIESA, 2005.

[9]Manual of Rural Technology with Implications for Mountain Tourism prepared by CRTN and published by ICIMOD December 1997.

used for running the Ghatta[10,11]. Ghattas can also be found throughout India, Pakistan, China, and even parts of Turkey. There are an estimated 200,000 traditional water mills in India alone (referred to there as a gharat, a chuksor, a panchaki or a chuthak)[12,13].

These power generating facilities and irrigation channels are examples in Nepal where landslides, debris flows and floods cause great damages with adverse effects to the local population, economy, agriculture and landscape.

2.5 Protection and Mitigation Measures Against Landslides and Debris Flows

Mountainous countries like Nepal frequently suffer a huge amount of losses of lives and properties every year because of unprecedented destructive impacts of avalanches, landslides, debris flows, mud flows and debris floods both in the northern mountain slopes and valleys, and the southern Terai plains [103]. Such events mainly take place during the monsoon season of the year. Otherwise, snow avalanche may take place in Winter, or in Spring. The increasing population and growing developmental activities have put pressure on developers and planners to build infrastructures even in such an area that have potentially high risk of geo-physical mass flows like debris flows, landslides, mud flows and induced tsunami. The protection measures against such detrimental events are very essential (Pudasaini and Hutter, 2007 [103]).

The protection and mitigation measures may differ depending on the slope angles, slope orientation, topography, civil structures and the objects' nature that are supposed to be protected like a highway, a road, a railway track, a house, a village or a whole town. The main target of research activities on dynamics of geophysical mass flows is to protect human lives, their properties and other physical infrastructures that are at the high risk of debris flows and other similar events [11, 21, 41, 85, 103]. The protective measures should be of high quality to withstand any possible impacts of mass flows.

In the context of Nepal, different engineering and bio-engineering defense techniques like, debris flow catch dams, vegetation plantation and wire barriers are being installed and

[10]Annual Report of IWM Programme (2004), CRTN, February 2005.

[11]Case prepared by CRTN for NGO Capacity Development Project supported by INFORSE, 2005.

[12]Improvement of Water Mills (Ghattas) in Hilly Areas of Nepal for Rural Applications, An Overview, April 2000.

[13]Annual Reports and Publications, 200304, published by Alternative Energy Promotion centre, HMGNepal.

Figure 2.8: (a) Rock anchoring structure at Khawa, Dhulikhel, in the Araniko Highway, central Nepal, for protecting the road by stabilizing the slope. (b) Bio-engineering system utilized to control the slope (Photo: Field excursion during the symposium, MGDA-11).

applied for protecting area either from the previously catastrophic-hit areas, or also landslide and debris flow prone areas (Fig. 2.8) [10, 11, 31, 122]. The methods are mainly in action along the major highways connecting Kathmandu, the capital of Nepal with other places. Countries with mountainous area had acquired ample experiences to deal with snow avalanches, debris flow, landslide and to avoid high risk long before scientists started to work on this topic [103]. However, with increasing human activities and fatalities, it is essential to protect the society and civil structures with advanced scientific and technological methods.

In Nepal, mitigation and protection measures are being taken against landslide and debris flow hazards [14, 20, 21]. However, it is still a great challenge for the engineers and practitioners to properly understand the complex flow dynamics and design and install appropriate mitigation measures and strategies and defence structures in hazard hit or prone areas. The most important aspect of the mitigation and protection measures is that they are very expensive [35, 41, 85, 103]. So, proper understanding of these mitigation and defence measures is must before they are constructed to make sure that they function properly and for a long time. This requires the advanced and more accurate knowledge of the complex flow dynamics including the flow depth, velocity distribution, impact and dynamic pressures and flow obstacle interactions (Fig. 2.9) [10, 16, 17, 31, 99, 103]. Although the conditions and the protection measures have been improved for some years,

Figure 2.9: (a) Large scale landslide width of the 755 m on the north of Bahrabise and located on the left bank of Sunkoshi River along the Araniko Highway, central Nepal. (b) Gabion is being constructed to stabilize the slope to protect the part of Araniko Highway from further landslides (Photo: Field excursion during the symposium, MGDA-11).

but it again started deteriorating in some places. The worse example is a large scale landslide near Bahrabise of Araniko highway. In fact, the landslide was activated by the road construction, and it has been causing a sever problem since the beginning of the construction of the Araniko Highway. Every year, the landslides occur and the preventive measures have not been effective there.

2.6 Review of Field: Different Modeling Approaches of Geophysical Mass Flows

2.6.1 Single-Phase Models

Visco-plastic Models: Avalanches [103], debris flows [50], landslides [70], or submarine avalanches [36] are catastrophic events characterized by the flow of a mixture of liquid and solid particles down a slope. Several modeling approaches have been developed in the past to describe the dynamics of such geophysical mass flows. Some early approaches considered the mixture as a non-Newtonian fluid described by a Bingham plastic, or a Hershel Bulkley rheology [45, 47, 50, 90]. Although the Bingham plastic, or the Hershel Bulkley models might be relevant for pure mud flows as a mixture of fine sediment par-

ticles and water, the single-phase approach may not be appropriate when a significant amount of coarse granular materials are also involved in the flow [50, 54]. In this case, a relative motion between the fluid phase and the granular skeleton often develops, which induces gradients of fluid pressure that may dramatically affect the flow [54, 110, 112].

Grain-Inertial and Macro-Viscous Models: The other spectrum of modelling was presented by the pioneering work of Bagnold who developed a dilatant or, grain-inertial, and macro-viscous flow rheology [3, 50, 97]. Newtonian, two or three parameter yield strength fluids and power law, or dilatant fluids are commonly used rheological models while describing debris flows as a single-phase continuum [97]. If the shear and normal stresses in the mixture (suspension) vary quadratically with the shear-rate, the flow is said to satisfy Bagnold's grain-inertia flow. If this relation is linear, then the motion is said to satisfy Bagnold's macro-viscous flow which is the same as the Newton's law of viscosity. These flow laws were derived by Bagnold in 1954 with his novel experiments in an annular coaxial cylinder rheometer where he evaluated the effects of grain interaction in the suspension. For more on this and the applications of the Bagnold's law [8, 97, 103, 118] is referred. Pudasaini (2011) [97] constructed several analytical solutions for debris flows and avalanches based on the Bagnold's grain-inertial and macro-viscous laws, and the solutions are well compared with experimental and field data. However, Bagnold's model may not be applicable in complex flow situations, such as naturally buoyant flows [50, 98].

Frictional Granular Flow Models: Savage and Hutter (1989, 1991) [113, 114], were probably the first to develop a pioneering continuum mechanical model for the full description of the flow of a finite mass of frictional granular material down a rough inclined slope. This model is based on the Mohr-Coulomb frictional rheology [33, 100, 102, 103, 113, 123]. The model consists of a set of depth-averaged mass and momentum balance equations that describes the complete evolution of a granular flow or, an avalanche, from its post-critical state to the final deposition in the run-out zone. The model is mainly based on the assumption of a thin-layer flow which means that the dynamics in the flow depth direction can be neglected in comparison to the dynamics along the sliding surface. From a physical point of view, this is equivalent to say that the momentum transfer mainly takes place in the down-slope and the cross-slope directions, and that the momentum transfer in the flow depth direction can be neglected. So, this model is akin to the hydraulic shallow water model, but the difference here is that the model by Savage and Hutter is developed for the flow of frictional granular material which, during the flow, can exhibit some special properties such as extending (e.g., right after the flow inception when the flow rarefies) and contracting (e.g., during flow obstacle interactions, and deposition process, or the

converging flows) modes of deformations. Importance of the extending and contracting behaviour is mentioned in Pudasaini and Kroener (2008) [105]. However, for simple flow situations, and far from depositions, such behaviour may have minimal effects [31, 105]. Subsequently, the Savage and Hutter model has been extended to geometrically two- and three-dimensional configurations, including simple to complicated basal topographies and also for flows in rotating drums with applications to pharmaceuticals and process engineering (Gray, 2001 [30]), and for snow and rock avalanches (Mergili et al., 2012 [80] ; Zwinger et al., 2003 [130]) in natural slopes. For detail on this, see Pudasaini and Hutter (2003, 2007)[102, 103]. However, there are other models in use, including the hydraulic, Newtonian, mass point, Voellmy-Salm and extended Voellmy-Salm, random kinetic energy models, statistical, and discrete element models, to name a few [6, 103].

2.6.2 Quasi Two-Phase Models

In reality, debris flows are such complex systems that a description by any single constitutive equation is highly improbable [97]. The relative motion between the fluid and the granular matrix can be created by different mechanics such as, the development of gradients of hydrostatic pressure when the surface of the liquid is inclined with respect to the horizontal [50, 51, 88], the presence of underground springs and the presence of heterogeneities in the granular media [75]. Two-phase granular-fluid mixture flows are characterized primarily by the relative motion and interaction between the solid and fluid phases.

As an important step in the model development, the frictional granular flow model of Savage and Hutter (1989) [113] was further extended to incorporate the effect of the interstitial fluid by Iverson (1991) [50], Iverson and Denlinger (2001) [53] for simple geometry, and by Pudasaini et al. (2005) [108] down a generally curved and twisted channel. Iverson and Denlinger (2001) [53] and Pudasaini et al. (2005) [108] utilized equations that allow basal pore fluid pressure to evolve and include viscous effects. The emerging equations are then so structured that the dry limit ($\lambda_f = 0$, see below) recovers the Savage and Hutter (1989) [113] model, while the fluid limit ($\lambda_f = 1$) generates the purely viscous equations appropriate for a slush or a viscous flood. The former constitute a purely hyperbolic, the later a mixed hyperbolic-parabolic system of partial differential equations. These equations contain a scale dependent dimensionless quantity N_R (Iverson, 1997 [50]; Iverson and Denlinger, 2001 [53]; Pudasaini et al., 2005 [108]) which is the fluid volume fraction weighed Reynolds number. The physical explanation of these debris flow models is based on the recognition that the fluid stress significantly contributes to the dynamics

of the flow. From the prospective of the soil mechanics, where the viscous effects of the fluid are generally ignored, here the inclusion of the pore pressure plays a significant role. Since the viscous contribution is added, it stabilizes the numerics because the viscous stresses, and the introduced diffusion equation for the pressure, generate parabolicity into the system of model equations [53, 108].

However, the Coulomb mixture models (Iverson, 1997 [50], Iverson and Denlinger, 2001 [53]) are only quasi two-phase or, virtually single-phase debris bulk models, because they neglect differences between the fluid and solid velocities. Thus, drag force could not be generated. Furthermore, a major and ad-hoc assumption is made in Iverson (1997) [50], Iverson and Denlinger (2001) [53], Pudasaini et al. (2005) [108], and Fernandez-Nieto et al. (2008) [22]. That is, they assume that total stress ($\mathbf{T}$) can be divided into the solid and the fluid constituents by introducing a factor λ_f such that the partial solid and fluid stresses are given by $(1-\lambda_f)\mathbf{T}$ and $\lambda_f\mathbf{T}$, respectively. Moreover, in these models, λ_f (ratio between the basal pore fluid pressure and the total basal normal stress, i.e., the pore pressure ratio [42]) is treated phenomenologically as an internal variable whose physical foundation is often discussed from different prospectives or, even questioned [22, 43, 44, 93]. Also, in these models, volume fraction of the solid is not a dynamical field variable [43, 44]. By formally constructing the eigenvalues associated with a system designed to describe a real two-phase mass flow model Pudasaini (2012) [98], and Pokhrel (2014) [94] revealed that debris motion is characteristically a two-phase flow phenomena, and that such flows may only be rigorously described by applying a real two-phase debris flow model (Pitman and Le (2005) [93]; Pudasaini, 2012 [98]) instead of an effectively single-phase debris bulk model.

2.6.3 Two-Phase Models

Berzi and Jenkins (2008a) [5] considered the steady and fully developed flows of particles and fluid down a slope. They made the assumption that the fluid phase rheology is described by an eddy viscosity and the granular phase by a shear-rate-dependent friction law (Da Cruz et al., 2005 [13]; Jop et al., 2006 [57]). However, their approach is restricted to steady and fully developed flows only and does not take into account other dynamical aspects, such as dilatancy effects [103], and the transient flow dynamics. Another important mechanism associated with the flow inception is the change in the bulk volume of the solid fraction experienced by the granular skeleton, called dilatancy [103]. To account for this effect, Pailha et al. (2009) [89] proposed a two-phase flow model, which is quantitatively compared with experiments. Based on two-phase flow concepts, several

theoretical models have been developed to describe debris flows (Jackson, 1997 [55]). The dilatancy of the granular layer and the pore pressure feedback mechanism are considered in the models developed by Iverson (2005) [52] and Schaeffer and Iverson (2008) [115]. In their approach, the landslide is described as a rigid block sliding down a slope, the source of dilatancy being localized at the base.

The solid and fluid phase velocities may deviate substantially from each other in real flow situations. This, then, fundamentally affects the whole flow mechanics. Depending on the material involved and the flow configuration, several physical mechanics must be introduced in order to properly model any two-phase mass flows [98]. One of the basic and important aspects is the drag force that incorporates coupling between the phases. As an another innovation in modeling geophysical mass flows, Pitman and Le (2005) [93] developed a depth-averaged two-fluid flow model to describe unsteady and non-uniform flows as a mixture of the solid particles and the fluid.

From rheological point of view, the Pitman and Le model considers Mohr-Coulomb plasticity for the granular phase [113], and the fluid pressure effects for the fluid phase. In terms of modeling the relative motion between the solid and the fluid phases, they introduced the simple drag force based on a relationship between the sedimentation and the terminal velocity of a particle falling in a viscous fluid. The Pitman and Le (2005) [93] model and its variants retain only a fluid pressure gradient and neglect the viscous effects of the fluid phase, another important physical aspect of two-phase flows [98]. However, depending on the constituents forming the fluid phase, which can include silt, clay, and fine particles, the fluid phase in natural debris flows can deviate substantially from an ideal fluid. For example, the viscosity in many natural debris flows can range from 0.001 to 10 Pas or even higher [50, 124]. A small change in the fluid viscosity may lead to substantial change in the dynamics of the debris motion [98].

2.6.4 A General Two-Phase Mass Flow Model

The rheology and flow behavior can vary and depend on the sediment composition and percentage of solid and fluid phases. One phase (e.g., solid) may accelerate relative to another phase (e.g., fluid), thus inducing virtual mass. The amount and gradient of the solid particles considerably influences flow, which can enhance or diminish viscous effects. Depending on the amount of grains and flow situation, the drag force should combine the solid- and fluid-like contributions and also a linear (laminar-type, at low velocity) and quadratic (turbulent-type, e.g., Voellmy drag; at high velocity) drags. To take into account these important aspects of a two-phase mass flow, recently, Pudasaini (2012) [98]

developed a generalized two-phase mass flow model. This model unifies existing avalanche and debris flow theories. The model (Pudasaini, 2012 [98]) covers both the single-phase and two-phase scenarios and includes many essential and observable physical phenomena. In this model, the solid-phase stress is closed by Mohr-Coulomb plasticity, while the fluid stress is modeled as a non-Newtonian viscous stress that is enhanced by the solid-volume-fraction gradient. A generalized interfacial momentum transfer includes viscous drag, buoyancy and virtual mass forces, and a new generalized drag force is introduced to cover both solid-like and fluid-like drags. Strong couplings between solid and fluid momentum transfer are another important aspects of the general two-phase model [98, 99, 106, 107]. The two-phase model is further extended to describe the dynamics of rock-ice avalanches with new enhanced mechanical models [104]. This model explains dynamic strength weakening and includes internal fluidization, basal lubrication, and exchanges of mass and momentum between the phases.

Furthermore, the virtual mass force, that is present in the model equations (3.8)-(3.17), alters flow dynamics by increasing the kinetic energy of the fluid. Newtonian viscous stress substantially reduces flow deformation, whereas non-Newtonian viscous stress may change the overall flow dynamics. Strong non-linear dynamics of the fluid fraction demonstrates the typical state of the two-phase debris flow (Pudasaini, 2012 [98]).

Chapter 3

Physical-Mathematical Model for Landslide, Debris Flow and Tsunami

Modeling the tsunami waves generated by landslides and debris flows and debris avalanches involves the generation mechanism and the water motion close to the impact and the subsequent propagation of the tsunami waves and submarine debris mass movement, the complex wave interactions and the inundation [92, 99, 107]. The comprehensive and generalized physical-mathematical model developed by Pudasaini (2012) [98] is presented to describe the three-dimensional and two-phase landslides and debris flows. The model can be used to simulate the three-dimensional subaerial and submarine two-phase debris flows, and induced tsunami. Starting with the full three-dimensional and two-phase debris flow model equations later a tractable set of reduced depth-averaged equations are discussed which represents a good compromise between accuracy of the results and the computational costs. The boundary conditions applied to generate reduced equations are briefly mentioned. Important features of the two-phase mass flow model are described. Finally, the reduction of the relatively more complex two-phase mass flows equations into relatively simple single-phase Navier-Stokes and hydraulic shallow water equations, and the non-linear tsunami models are mentioned.

3.1 A 3D, Two-Phase Mass Flow Model

The two phases are characterized by distinct material properties: the fluid phase is characterized by its density ρ_f, viscosity η_f, and isotropic stress distribution; the solid phase is characterized by its density ρ_s, internal and basal friction angles ϕ and δ, and anisotropic stress distribution, K (lateral earth pressure coefficient) [98]. These characterizations and the presence of relative motion between phases lead to two different mass and momentum

balance equations for the solid and the fluid phases, respectively. Let $\mathbf{u}_s = (u_s, v_s, w_s)$, $\mathbf{u}_f = (u_f, v_f, w_f)$ and α_s, α_f $(= 1-\alpha_s)$ denote the velocities, and volume fractions for the solid and the fluid constituents, denoted by the suffix s and f, respectively. In the general two-phase debris flow model proposed by Pudasaini (2012) [98], the phase-averaged balance equations for mass and momentum conservations is considered and the following assumptions are made: surface tension is negligible, interfacial solid and fluid pressures are identical to the (true) fluid pressure, the solid and fluid components are incompressible (the true densities are constants), and no phase change occurs [18, 48, 49, 99]. However, the phase change from the solid-phase to the fluid-phase has recently been modeled by developing a new enhanced mechanical model by Pudasaini and Krautblatter (2012) [104].

The full three-dimensional, two-phase debris flow model proposed by Pudasaini (2012) [98] are as follows [32, 102, 103, 113, 123]:

$$\frac{\partial \alpha_s}{\partial t} + \nabla.(\alpha_s \mathbf{u}_s) = 0, \tag{3.1}$$

$$\frac{\partial \alpha_f}{\partial t} + \nabla.(\alpha_f \mathbf{u}_f) = 0, \tag{3.2}$$

$$\frac{\partial}{\partial t}(\alpha_s \rho_s \mathbf{u}_s) + \nabla.(\alpha_s \rho_s \mathbf{u}_s \otimes \mathbf{u}_s) = \alpha_s \rho_s \mathbf{f} - \nabla.\alpha_s \mathbf{T}_s + p\nabla\alpha_s + \mathbf{M}_s, \tag{3.3}$$

$$\frac{\partial}{\partial t}(\alpha_f \rho_f \mathbf{u}_f) + \nabla.(\alpha_f \rho_f \mathbf{u}_s \otimes \mathbf{u}_f) = \alpha_f \rho_f \mathbf{f} - \alpha_f \nabla p + \nabla.\alpha_f \boldsymbol{\tau}_f + \mathbf{M}_f. \tag{3.4}$$

Equations (3.1) and (3.2) are the mass balance equations, and equations (3.3) and (3.4) are the momentum balance equations, where

$$\mathbf{M}_s = \frac{\alpha_s \alpha_f (\rho_s - \rho_f) g}{[\mathcal{U}_T\{\mathcal{P}\mathcal{F}(Re_p) + (1-\mathcal{P})\mathcal{G}(Re_p)\}]^J}(\mathbf{u}_f - \mathbf{u}_s)|\mathbf{u}_f - \mathbf{u}_s|^{J-1} + \alpha_s \rho_f C_{VM}$$
$$\left[\left(\frac{\partial \mathbf{u}_f}{\partial t} + \mathbf{u}_f.\nabla\mathbf{u}_f\right) - \left(\frac{\partial \mathbf{u}_s}{\partial t} + \mathbf{u}_s.\nabla\mathbf{u}_s\right)\right], \tag{3.5}$$

$$|\mathbf{S}| = N\tan\phi, \;\; T_{xx} = K_x T_{zz}, \;\; T_{yy} = K_y T_{zz}, \tag{3.6}$$

$$\boldsymbol{\tau}_f = \eta_f \left[\nabla\mathbf{u}_f + (\nabla\mathbf{u}_f)^t\right] - \eta_f \frac{\mathcal{A}(\alpha_f)}{\alpha_f}\left[(\nabla\alpha_s)(\mathbf{u}_f - \mathbf{u}_s) + (\mathbf{u}_f - \mathbf{u}_s)(\nabla\alpha_s)\right], \tag{3.7}$$

and, $\mathbf{M}_f = -\mathbf{M}_s$, where, $\mathbf{S}$ is the shear stress, N is the normal load, and T_{xx}, T_{yy} and T_{zz} are the normal stress components in the coordinate directions. Similarly, p is the fluid pressure, and $\mathcal{A}$ is the mobility of fluid at interface. There is strong coupling between the solid and the fluid momentum transfer both through the interfacial momentum transfer $\mathbf{M}$, which includes the viscous drag and the virtual mass force C_{VM}, and the enhanced non-Newtonian viscous fluid stress $\boldsymbol{\tau}_f$. C_{VM} can be considered differently depending upon the problem. One of the possibilities is $C_{VM} = \frac{1}{2}\left(\frac{1+2\alpha_s}{\alpha_f}\right)$. In case α_f is very small, we can choose some suitable numerical values for C_{VM}. There are eight equations, with eight unknowns $(u_s, v_s, w_s; u_f, v_f, w_f; \alpha_s, p)$. The system is closed and can be solved numerically.

3.2 Depth Averaged Model Equations

Natural-scale geophysical mass flows may involve masses as large as 10^6 to 10^{13} m^3 [12, 70, 98, 103, 119, 120]. So, the three-dimensional model (3.1)-(3.7) typically may be unmanageable, otherwise, requires huge computational efforts. However, the full three-dimensional models can be made more tractable by assuming that, as observed in nature, globally flows are long (or, wide) relative to their depth, and to use depth-averaging in the z-direction. This is called the thin layer approximation. This is a common rational utilized in developing geophysical mass flows [32, 50, 53, 93, 108, 113]. With this, A set of depth-averaged equations for the flowing mass and momentum transfer for the solid and fluid components can be developed along the sliding surface. In the process of reducing the models from the three-dimension to two-dimension, boundary conditions are applied, that introduces the flow depth. As for single-phase [113], or mixture flows [50, 108], or two-fluid flows [22, 93], it is assumed that solid-fluid mixture, and the solid- and fluid-phase constituents separately satisfy the kinematic free-surface and bottom boundary conditions. The top surface is traction-free, and Coulomb sliding (for solid) and no-slip (for fluid) conditions are satisfied at the flow base [50, 103, 108].

Let depth-averaged velocity components for fluid $\mathbf{u}_f = (u_f,\, v_f)$ and for solid $\mathbf{u}_s = (u_s,\, v_s)$ in the down-slope (x) and the cross-slope (y) direction, respectively, to be computed as functions of space and time. Then, the depth-averaged solid and fluid mass and the momentum balance equations in the down-slope and the cross-slope directions are given by [98]:

$$\frac{\partial}{\partial t}(\alpha_s h) + \frac{\partial}{\partial x}(\alpha_s h u_s) + \frac{\partial}{\partial y}(\alpha_s h v_s) = 0, \tag{3.8}$$

$$\frac{\partial}{\partial t}(\alpha_f h) + \frac{\partial}{\partial x}(\alpha_f h u_f) + \frac{\partial}{\partial y}(\alpha_f h v_f) = 0, \tag{3.9}$$

$$\begin{aligned}\frac{\partial}{\partial t}\left[\alpha_s h(u_s - \gamma\mathcal{C}\,(u_f - u_s))\right] + \frac{\partial}{\partial x}\left[\alpha_s h\left(u_s^2 - \gamma\mathcal{C}(u_f^2 - u_s^2) + \frac{\beta_{x_s} h}{2}\right)\right] \\ + \frac{\partial}{\partial y}\left[\alpha_s h(u_s v_s - \gamma\mathcal{C}(u_f v_f - u_s v_s))\right] = h S_{x_s},\end{aligned} \tag{3.10}$$

$$\begin{aligned}\frac{\partial}{\partial t}\left[\alpha_s\, h\,(v_s - \gamma\mathcal{C}\,(v_f - v_s))\,\right] + \frac{\partial}{\partial x}\left[\alpha_s h(u_s\, v_s - \gamma\mathcal{C}(u_f v_f - u_s v_s))\right] \\ + \frac{\partial}{\partial y}\left[\alpha_s h\left(v_s^2 - \gamma\mathcal{C}(v_f^2 - v_s^2) + \frac{\beta_{y_s} h}{2}\right)\right] = h S_{y_s},\end{aligned} \tag{3.11}$$

$$\frac{\partial}{\partial t}\left[\alpha_f h\left(u_f+\frac{\alpha_s}{\alpha_f}\mathcal{C}(u_f-u_s)\right)\right]+\frac{\partial}{\partial x}\left[\alpha_f h\left(u_f^2+\frac{\alpha_s}{\alpha_f}\mathcal{C}(u_f^2-u_s^2)+\frac{\beta_{x_f}h}{2}\right)\right]$$
$$+\frac{\partial}{\partial y}\left[\alpha_f h\left(u_f v_f+\frac{\alpha_s}{\alpha_f}\mathcal{C}(u_f v_f-u_s v_s)\right)\right]=hS_{x_f}, \tag{3.12}$$

$$\frac{\partial}{\partial t}\left[\alpha_f h\left(v_f+\frac{\alpha_s}{\alpha_f}\mathcal{C}(v_f-v_s)\right)\right]+\frac{\partial}{\partial x}\left[\alpha_f h\left(u_f v_f+\frac{\alpha_s}{\alpha_f}\mathcal{C}(u_f v_f-u_s v_s)\right)\right]$$
$$+\frac{\partial}{\partial y}\left[\alpha_f h\left(v_f^2+\frac{\alpha_s}{\alpha_f}\mathcal{C}(v_f^2-v_s^2)+\frac{\beta_{y_f}h}{2}\right)\right]=hS_{y_f}, \tag{3.13}$$

in which,

$$\beta_{x_s}=\varepsilon K_x p_{b_s},\ \beta_{y_s}=\varepsilon K_y p_{b_s},\ \beta_{x_f}=\beta_{y_f}=\varepsilon p_{b_f},\ p_{b_f}=-g^z,\ p_{b_s}=(1-\gamma)p_{b_f}.$$

The first two equations (3.8)-(3.9) are the depth averaged mass balances for solid and fluid phases, respectively, and the last four equations are the depth averaged momentum balances for solid (3.10)-(3.11) and fluid (3.12)-(3.13), in x- and y-directions, respectively. The source terms are:

$$S_{x_s}=\alpha_s\left[g^x-\frac{u_s}{|\mathbf{u}_s|}\tan\delta p_{b_s}-\varepsilon p_{b_s}\frac{\partial b}{\partial x}\right]-\varepsilon\alpha_s\gamma p_{b_f}\left[\frac{\partial h}{\partial x}+\frac{\partial b}{\partial x}\right]$$
$$+C_{DG}(u_f-u_s)\Big|\mathbf{u}_f-\mathbf{u}_s\Big|^{J-1}, \tag{3.14}$$

$$S_{y_s}=\alpha_s\left[g^y-\frac{v_s}{|\mathbf{u}_s|}\tan\delta p_{b_s}-\varepsilon p_{b_s}\frac{\partial b}{\partial y}\right]-\varepsilon\alpha_s\gamma p_{b_f}\left[\frac{\partial h}{\partial y}+\frac{\partial b}{\partial y}\right]$$
$$+C_{DG}(v_f-v_s)\Big|\mathbf{u}_f-\mathbf{u}_s\Big|^{J-1}, \tag{3.15}$$

$$S_{x_f}=\alpha_f\Bigg[g^x-\varepsilon\Bigg[\frac{1}{2}p_{b_f}\frac{h}{\alpha_f}\frac{\partial\alpha_s}{\partial x}+p_{b_f}\frac{\partial b}{\partial x}-\frac{1}{\alpha_f N_R}\left\{2\frac{\partial^2 u_f}{\partial x^2}+\frac{\partial^2 v_f}{\partial y\partial x}+\frac{\partial^2 u_f}{\partial y^2}-\frac{\chi u_f}{\varepsilon^2 h^2}\right\}$$
$$+\frac{1}{\alpha_f N_{R_{\mathcal{A}}}}\left\{2\frac{\partial}{\partial x}\left(\frac{\partial\alpha_s}{\partial x}(u_f-u_s)\right)+\frac{\partial}{\partial y}\left(\frac{\partial\alpha_s}{\partial x}(v_f-v_s)+\frac{\partial\alpha_s}{\partial y}(u_f-u_s)\right)\right\}$$
$$-\frac{\xi\alpha_s(u_f-u_s)}{\varepsilon^2\alpha_f N_{R_{\mathcal{A}}}h^2}\Bigg]\Bigg]-\frac{1}{\gamma}C_{DG}(u_f-u_s)\Big|\mathbf{u}_f-\mathbf{u}_s\Big|^{J-1}, \tag{3.16}$$

$$S_{y_f}=\alpha_f\Bigg[g^y-\varepsilon\Bigg[\frac{1}{2}p_{b_f}\frac{h}{\alpha_f}\frac{\partial\alpha_s}{\partial y}+p_{b_f}\frac{\partial b}{\partial y}-\frac{1}{\alpha_f N_R}\left\{2\frac{\partial^2 v_f}{\partial y^2}+\frac{\partial^2 u_f}{\partial x\partial y}+\frac{\partial^2 v_f}{\partial x^2}-\frac{\chi v_f}{\varepsilon^2 h^2}\right\}$$
$$+\frac{1}{\alpha_f N_{R_{\mathcal{A}}}}\left\{2\frac{\partial}{\partial y}\left(\frac{\partial\alpha_s}{\partial y}(v_f-v_s)\right)+\frac{\partial}{\partial x}\left(\frac{\partial\alpha_s}{\partial y}(u_f-u_s)+\frac{\partial\alpha_s}{\partial x}(v_f-v_s)\right)\right\}$$
$$-\frac{\xi\alpha_s(v_f-v_s)}{\varepsilon^2\alpha_f N_{R_{\mathcal{A}}}h^2}\Bigg]\Bigg]-\frac{1}{\gamma}C_{DG}(v_f-v_s)\Big|\mathbf{u}_f-\mathbf{u}_s\Big|^{J-1}, \tag{3.17}$$

where,

$$C_{DG} = \frac{\alpha_s \alpha_f (1-\gamma)}{[\varepsilon \mathcal{U}_T \{\mathcal{P}\mathcal{F}(Re_p) + (1-\mathcal{P})\mathcal{G}(Re_p)\}]^J}, \quad \mathcal{F} = \frac{\gamma}{180}\left(\frac{\alpha_f}{\alpha_s}\right)^3 Re_p,$$

$$\gamma = \frac{\rho_f}{\rho_s}, \quad \mathcal{G} = \alpha_f^{M(Re_p)-1}, \quad Re_p = \frac{\rho_f d \mathcal{U}_T}{\eta_f}, \quad N_R = \frac{\sqrt{gL}H\rho_f}{\alpha_f \eta_f}, \quad N_{R_\mathcal{A}} = \frac{\sqrt{gL}H\rho_f}{\mathcal{A}\eta_f}. \quad (3.18)$$

In the above equations, x, y and z are coordinates along the flow directions, and g^x, g^y and g^z are the components of gravitational acceleration. L and H are the typical length and depth of the flow, $\varepsilon = H/L$ is the aspect ratio, and $\mu = \tan\delta$ is the basal friction coefficient. K is the earth pressure coefficient (function of δ and ϕ, basal and internal friction angles of solid), C_{DG} is the generalized drag coefficient, $J = 1$ or 2 represents linear or quadratic drag. $\mathcal{U}_T$ is the terminal velocity of a particle and $\mathcal{P} \in [0, 1]$ is a parameter which combines the solid-like ($\mathcal{G}$) and fluid-like ($\mathcal{F}$) drag contributions to flow resistance. p_{b_f} and p_{b_s} are the effective fluid and solid pressures. γ is the density ratio, $\mathcal{C}$ is the virtual mass coefficient (solid particles induced kinetic energy of fluid phase), η_f is the fluid viscosity, M is a function of the particle Reynolds number (R_{e_p}), χ includes vertical shearing of fluid velocity, and ξ takes into account different distributions of α_s. $\mathcal{A} = \mathcal{A}(\alpha_f)$ is the mobility of the fluid at the interface, and N_R and $N_{R_\mathcal{A}}$ are quasi-Reynolds numbers associated with the classical Newtonian, and enhanced non-Newtonian fluid viscous stresses. Slope topography is represented by $b = b(x, y)$. Coulomb and no slip boundary conditions are employed for the solid and the fluid. Simple linear (laminar-type, at low velocity) or quadratic (turbulent-type, at high velocity) drag is associated with $J = 1$ or 2, respectively.

In (3.8)-(3.13) there are six equations that involve six number of unknowns. So, the numerical integration of these equations is possible. With the given material parameters listed above and the basal topography, $b = b(x, y)$, equations (3.8)-(3.13) permit the computation of debris flow depth h, volume fraction of the fluid α_f (or solid α_s), and the depth-averaged velocity components for solid u_s and v_s, and for fluid u_f and v_f parallel to the basal surface as functions of space and time, provided that the appropriate initial and (numerical) boundary conditions are prescribed.

3.3 Discussion on Important Features of the Model Equations

The model equations (3.8)-(3.17) are written as well structured hyperbolic-parabolic partial differential equations in conservative form [98]. There are several important features

of the model equations. Now, the most important physical aspects and their implications and applicability are discussed by closely following Pudasaini (2012) [98]. More discussion can also be found in Pudasaini (2012) [98], and Pudasaini and Miller (2012a,b) [106, 107].

Inertial and Pressure Terms

Here, some important aspects in the inertial and pressure terms are discussed that are present in (3.10)-(3.13). (i) The terms associated with β in the solid momentum equations (3.10)-(3.11) account for the buoyancy-reduced lateral pressures. The solid load is reduced by the buoyancy force as modeled by the factor $(1-\gamma)$. As the density ratio between fluid and solid approaches unity, the solid normal load vanishes, and hence, the hydraulic pressure gradient due to solids disappears. In this limiting case, the flow is neutrally buoyant [3] and the left-hand sides of (3.10)-(3.11) are purely inertial. (ii) The density ratio γ is present only in solid momentum equations (3.10)-(3.11). (iii) The presence of the virtual mass terms (through $\mathcal{C}$) is remarkable. It provides a strong coupling between the solid and fluid velocity components. The coupling occurs not only between the stream-wise (u_s and u_f) and cross-stream velocity components (v_s and v_f) but there are cross couplings between (u_s, v_s) and (u_f, v_f). However, if the relative acceleration of the solids with respect to the fluid is negligible, then all terms associated with $\mathcal{C}$ vanish. Thus, the velocity coupling induced in the stream-wise and cross-stream-wise directions by the virtual mass is an important feature of the model equations (3.8)-(3.13). Even if all source terms are neglected (i.e., $S_x = 0$, $S_y = 0$), velocity coupling remains effective through the virtual mass terms. The solid volume fraction (α_s) always appears as a multiple of $\mathcal{C}$. (iv) If the relative phase velocity is negligible (i.e., the solid and fluid components are interlocked), then, all the terms associated with $\mathcal{C}$ vanish. In this case, there will be only two momentum balance equations, stream-wise and cross-stream-wise bulk momentum equations, instead of four for the two-phases.

Applied Forces

Applied forces are collected in the source terms for both components. The source terms for the solid momentum equations (3.14)-(3.15) have multiple contributions to force [98]:

(i) gravity, Coulomb friction and the topographic slope gradients. These terms (the first square brackets) appear in model for single-phase (granular) and mixture flows even if $\gamma = 0$ (i.e., the fluid contribution is neglected). If a flow is neutrally buoyant

(this can happen in highly viscous natural debris flows (see, e.g., McArdell et al., 2007 [78])), the contributions due to Coulomb friction, and the basal-surface gradient vanish because the basal surface does not experience any solid load, and the solid shear stress vanishes [98]. Under these conditions of hydrodynamic support of the particles by the fluid, the debris mass is fully fluidized (or lubricated) and moves very economically promoting long travel distances [98].

(*ii*) The terms associated with the second square brackets are due to the buoyancy force that include free-surface and basal-surface gradients.

(*iii*) The generalized drag terms (C_{DG}) associated with uniform flows are described by the last terms, and play an important role in the dynamics of two-phase debris flows as they strongly couple stream-wise solid and fluid velocities [98]. These drag coefficients explicitly incorporate many essential physical parameters. The generalized drag is modeled by a linear combination of $\mathcal{F}$ and $\mathcal{G}$. The behavior depends on the interpolation parameter $\mathcal{P}$ between the contribution of fluid flow through a densely packed solid ($\mathcal{F}$) and the contribution of particles moving through a fluid ($\mathcal{G}$) [98]. For values of $\mathcal{P} > 0$, the generalized drag achieves minimum values (for α_s close to zero), and increases as α_s increases. Large values of $\mathcal{P}$ correspond to fluid flow through the solid, which induces more drag in the flow. Therefore, C_{DG} serves as a generalized drag coefficient for two-phase, viscous debris flows and dispersive, particle-laden flows, and offers ability to simulate a wide spectrum of geophysical mass flows, like flows of lahar, mudflow, mud-flood and hyper-concentrated flows [98, 106, 107]. In four special situations, C_{DG} vanishes: when the relative velocity between solids and fluid is negligible, when the flow is neutrally buoyant or when either solid (pure fluid flow) or fluid volume fraction vanishes (dry grain flow).

The source terms for the fluid-momentum equations (3.16)-(3.17) also have multiple contributions to force [98]. The first three terms in (3.16) appears from the gravity load applied to the fluid phase (first term), the fluid pressure at the bed (second term) and the topographic slope (third term). The fourth group of terms associated with N_R appears from the viscous force contribution of the fluid phase. The fifth group of terms associated with $N_{R_\mathcal{A}}$ occurs because, viscous shear stress is enhanced by the solid-volume-fraction gradient [98]. These are non-Newtonian viscous contributions. In typical situations, the terms associated with N_R may be neglected, e.g., when N_R is sufficiently larger than the velocity diffusion contributions (terms associated with N_R). Even when terms with N_R

are negligible, terms associated with $N_{R_\mathcal{A}}$ may still be important, because they depend on the complex structure of the terms associated with N_{R_A}. In fact, it depends on the second gradients of the solid volume fraction, and the first gradients of the relative motions between the phases. In many flow situations, these gradients can be large enough to control the effect of the factor $1/N_{R_\mathcal{A}}$. For example, when a natural-dam failure or landslide-induced debris flow begins, mixing between solid and fluid phases starts. In this situation, the diffusion coefficient associated with $N_{R_\mathcal{A}}$ can become very large. When bank failure delivers solid material to a relatively low-solid-concentration stream, the solid volume fraction gradient and the relative motion between the solid and the fluid is large [98]. Another typical situation is a submarine debris release or subaerial debris plunging into a river, or a mountain lake or a hydropower dam (see, e.g., Crosta et al. 2004 [12], Strom and Korup, 2006 [120]). In these complex flows, concentration gradients of solids change rapidly [98].

Viscous Dissipations

In case if solid grains are dispersed in a fluid and the grain-grain friction is negligible, the earth pressure coefficient $K = 1\,(\text{i.e.}, \delta = 0,\, \phi = 0,\, \mathcal{F})$, and inclusion of the viscous stresses is important because the grain shear stress terms in x- and y-directions -$\alpha_s(u_s/|\mathbf{u}|_s)\tan\delta\, p_{b_s}$, -$\alpha_s(v_s/|\mathbf{u}|_s)\ \tan\delta\, p_{b_s}$can be neglected. This results in buoyant grain flows which are resisted by viscous and drag forces, and the relative acceleration between solid and fluid components (virtual mass). Because of buoyancy, the basal solid stress, p_{b_s} can also be expressed in terms of the fluid pressure, p_{b_f}. This results in the buoyancy reduced solid load. When the debris mass is neutrally buoyant (i.e., $\gamma = 1$), then the basal solid weight (p_{b_s}) vanishes. In this situation Coulomb friction disappears, the generalized drag coefficient C_{DG} becomes zero and also the basal slope has no effect on solid grains. So, only effective solid forces are due to gravity and the force associated with buoyancy [98].

Moreover, for the fluid phase, the viscous and gravity forces are effective in addition to the force induced by the gradient of the solid volume fraction ($\nabla\alpha_s$), the fluid pressure gradient at the base, and the fluid pressure exerted on the topography (see, (3.16) and (3.17)). The fluid viscous terms, associated with both N_R and $N_{R_\mathcal{A}}$, are as important as the basal (slope) gradient terms $\varepsilon\alpha_s p_{b_s}\partial b/\partial x$ and $\varepsilon\alpha_s p_{b_s}\partial b/\partial y$, the pressure gradient terms $\partial(\alpha_s\beta_x h^2/2)/\partial x$ and $\partial(\alpha_s\beta_y h^2/2)/\partial y$ in solid momentum equations (3.10), (3.11), (3.14) and (3.15) and $\varepsilon\alpha_f\partial(p_{b_f}h^2/2)/\partial x$, $\varepsilon\alpha_f\partial(p_{b_f}h^2/2)/\partial y$ in the fluid momentum equations

(3.12), (3.13), (3.16) and (3.17). Therefore, the viscous terms must also be included in the fluid momentum equations. Since, the viscosity η_f is in the denominator (of N_R and) $N_{R_\mathcal{A}}$, the influence of the terms associated with $N_{R_\mathcal{A}}$ in the fluid momentum equations increases as the magnitude of u_f - u_s increases [98].

The Drag Forces

The generalized drag terms play very important role in the dynamics of three-dimensional and two-phase debris flows as these coefficients (i.e., C_{DG}) explicitly incorporate many essential physical parameters, including the volume fractions of the solid and fluid (i.e., α_s and α_f), the solid and fluid densities (i.e., ρ_s and ρ_f), terminal velocity of solid particles (i.e., $\mathcal{U}_T$), particle diameter, and fluid viscosity η_f [98].

The parameter $\mathcal{P}$ can play a crucial role to fit the data and the model calibration. Two limiting cases are of particular importance: $\mathcal{P} = 0$ is more suitable when solid particles are moving through a fluid. In contrast, $\mathcal{P} = 1$ is more suitable for flows of fluids through dense packing of grains [93]. Thus, the generalized drag coefficient proposed by Pudasaini (2012) [98] helps to simulate a wide spectrum of geophysical mass flows, and also possibly industrial mixture flows [98]. By setting $\mathcal{P} = 0$ and $J = 1$, the drag coefficient of Pitman and Le (2005) [93] can be recovered and $\mathcal{P} = 1$ and $J = 1$ corresponds to the drag coefficient in Pailha and Pouliquen (2009) [89]. This also makes clear that the model equations proposed by Pudasaini (2012) [98] are more general.

Diffusion Process of the Solid Volume Fraction

In (3.16), the expression associated to $N_{R_\mathcal{A}}$ (except $\xi\alpha_s(u_f - u_s)/\varepsilon^2\alpha_f N_{R_A}h^2$) can be written in the form

$$h\left[\frac{\partial}{\partial x}\left\{\frac{2}{N_{R_\mathcal{A}}}(u_f - u_s)\frac{\partial \alpha_s}{\partial x}\right\} + \frac{\partial}{\partial y}\left\{\frac{1}{N_{R_\mathcal{A}}}(v_f - v_s)\frac{\partial \alpha_s}{\partial x}\right\} + \frac{\partial}{\partial y}\left\{\frac{1}{N_{R_\mathcal{A}}}(u_f - u_s)\frac{\partial \alpha_s}{\partial y}\right\}\right].$$

The quantities $(u_f - u_s)/N_{R_\mathcal{A}}$ and $(v_f - v_s)/N_{R_\mathcal{A}}$ are velocity-dependent dynamic diffusion coefficients for the solid volume fraction α_s. So, the intensity of the diffusion of solid volume fraction (α_s) depends mainly on the magnitude of the relative velocity of solid with respect to the fluid. Clearly, there is no diffusion of α_s in case $u_f - u_s = v_f - v_s = 0$. Most of the previous models did not take into account of the evolving solid concentration. The advection of α_s has also been included in the inertial terms of the equations (3.8) and (3.9) as a field variable [98, 99, 107].

3.4 Reduction to Navier-Stokes, Shallow Water and Tsunami Models

3.4.1 Reduction to Navier-Stokes Equations

If the solid contribution is neglected by taking $\alpha_s = 0$, $\alpha_f = 1$, $u_s = 0$, $v_s = 0$, $u_f = u$, $v_f = v$, $\eta_f = \eta$, $S_{x_f} = S_x$, $S_{y_f} = S_y$, $\rho_f = \rho$, then the model equations (3.8)-(3.13) with source term (3.14)-(3.17) reduced to:

$$\frac{\partial h}{\partial t} + \frac{\partial}{\partial x}(hu) + \frac{\partial}{\partial y}(hv) = 0, \tag{3.19}$$

$$\frac{\partial}{\partial t}\left[hu\right] + \frac{\partial}{\partial x}\left[h\left(u^2 + \frac{\beta_x h}{2}\right)\right] + \frac{\partial}{\partial y}\left[huv\right] = hS_x, \tag{3.20}$$

$$\frac{\partial}{\partial t}\left[hv\right] + \frac{\partial}{\partial x}\left[huv\right] + \frac{\partial}{\partial y}\left[h\left(v^2 + \frac{\beta_y h}{2}\right)\right] = hS_y, \tag{3.21}$$

in which, u and v are the velocities, and ρ and η are the density and viscosity of the bulk (fluid), and

$$\beta_x = \beta_y = \varepsilon p_b, \quad p_b = -g^z.$$

Equation (3.19) is the depth-averaged mass balance for the fluid and, (3.20) and (3.21) are the depth-averaged momentum balance equations for the fluid in x- and y-directions, respectively. The source terms are:

$$S_x = \left[g^x - \varepsilon\left[p_b\frac{\partial b}{\partial x} - \frac{1}{N_R}\left\{2\frac{\partial^2 u}{\partial x^2} + \frac{\partial^2 v}{\partial y \partial x} + \frac{\partial^2 u}{\partial y^2} - \frac{\chi u}{\varepsilon^2 h^2}\right\}\right]\right], \tag{3.22}$$

$$S_y = \left[g^y - \varepsilon\left[p_b\frac{\partial b}{\partial y} - \frac{1}{N_R}\left\{2\frac{\partial^2 v}{\partial x^2} + \frac{\partial^2 u}{\partial x \partial y} + \frac{\partial^2 v}{\partial x^2} - \frac{\chi v}{\varepsilon^2 h^2}\right\}\right]\right], \tag{3.23}$$

where,

$$N_R = \frac{\sqrt{gL}H\rho}{\eta}.$$

Equations (3.19)-(3.21) with source terms (3.22)-(3.23) are similar to the (depth-averaged) Navier-Stokes equations in which the fluid viscous stresses are given by the Newtonian law of viscosity that correspond to the terms associates with $1/N_R$ in (3.22) and (3.23).

3.4.2 Reduction to Shallow Water Equations and Tsunami Models

By setting $N_R \to \infty$ (i.e., neglecting the viscous stresses), the above Navier-Stokes-type fluid dynamical equations (3.19)-(3.21) reduce to the non-linear shallow water equations, or the tsunami models, for which the mass and momentum balance equations remain unchanged, but the source terms for the momentum equations (3.22)-(3.23) reduce to:

$$S_x = g^x - \varepsilon p_b \frac{\partial b}{\partial x} - \boldsymbol{\tau}_{b_x}, \tag{3.24}$$

$$S_y = g^y - \varepsilon p_b \frac{\partial b}{\partial y} - \boldsymbol{\tau}_{b_y}, \tag{3.25}$$

where, $\boldsymbol{\tau}_{b_x}, \boldsymbol{\tau}_{b_y}$ are some appropriately chosen basal shear stresses, such as, the hydraulic Chezy friction parameter [15]. Note that, usually, in the simplified situation, the shallow-water models refer to the one with $\partial b/\partial x = 0$, $\partial b/\partial y = 0$, and mainly when the basal shear stress terms are neglected, i.e., $\boldsymbol{\tau}_{b_x} = 0, \boldsymbol{\tau}_{b_y} = 0$.

Furthermore, the linear shallow-water, or the linear tsunami models are reduced from (3.19)-(3.21), by neglecting the non-linear terms. Far from the coastal regions, linear tsunami models are used in which the basal frictions are also ignored. This is so, because, in these regions, the non-linearity and basal frictions can be neglected. This largely reduces the computational costs and complexity.

Chapter 4

Two-Dimensional High-Resolution Numerical Simulation Method

[1]Alongwith the rapid development of computational power in the second half of the 20th century, numerical simulation became powerful and flourished many different methods. To solve the complicated system of equations by numerical techniques, numerical method is the most powerful and convenient way. Here, TVD-NOC schemes which are high resolution shock-capturing schemes are presented. These schemes employ a two-step method with the predictor-corrector steps [103]. In this Chapter, mostly spatially two-dimensional flows are analyzed. Lagrangean integration method is briefly discussed. The two-dimensional non-oscillatory finite difference schemes are described in the Eulerian form. Finally, the TVD-NOC schemes are applied to the two-phase debris flow model equations proposed by Pudasaini (2012) [98].

4.1 Development of 2D Numerical Scheme

To solve the dynamical mass flow equations the numerical methods have been employed and they have their history developed from simple to complex. It started with plane (chute) flows [32, 33, 113, 114] and then later sidewise confinement was removed so as to treat the mass flow as a two-dimensional flow [32, 33, 103, 121, 128]. For avalanche equations, the flow in curved and twisted channels were also incorporated and solved numerically [102, 103]. For different geophysical mass flows, the large deformations, and rapid motions must be considered. So, classical numerical schemes were unable to capture the shock. To address the sudden changes in the flow variables, including velocity

[1]The chapter closely follows Chapter 7 and Chapter 8 of the *Avalanche Dynamics* book by Pudasaini and Hutter (2007) [103].

components and flow depth, modern numerical methods were developed [103, 121, 123].

Savage and Hutter (1989) [113] introduced finite difference schemes, namely Lagrangean and the other Eulerian type to solve the equations of motion describing the finite mass granular avalanche flow down a rough incline, spatially in one-dimension [103]. Lagrangean scheme was found to be simple and sufficient to predict the observable behaviour of the flow [103]. A fixed spatial grid that extends upstream and downstream of the moving pile was used in Eulerian approach that yield the finite velocities upstream and downstream of the pile even at those parts of the bed where there was no material and depth was zero. This became responsible for sudden changes in the velocities corresponding to the front and rear of the pile, which destroys the stability in numerical integration. Artificial viscosity was added to diffuse the instability but the velocities in the regions outside of that occupied by the pile began to affect the results in the region of the pile itself [103]. To tackle with such difficulties, a Lagrangean scheme was developed in which the computational grid advects with the moving material itself. This method turned out to be more simple, more efficient and reliable. However, it was unable to capture the singularities.

Greve and Hutter (1993) [33] also used Lagrangean scheme to compute, numerically the avalanche height, velocity distribution, the front, the rear and in-between positions of the maximum avalanche height for different numerical and material parameter values for a motion of a granular avalanche in a convex and concave chute [103]. As for example, some tradition numerical schemes, include upwind method and second order schemes, include the Lax-Wendroff method and Upwind beam-warming method. In traditional second-order central differencing methods, there arouse oscillations in the numerical solution for physical problems with large gradients of the flow variables.

It is natural to observe shock formations in geophysical mass flows on an inclined surface merging into a horizontal run out zone encountering an obstacle when the velocity becomes subcritical from supercritical state. So, it requires to apply conservative high resolution numerical techniques that are capable to resolve the steep gradients and moving fronts [103, 121, 122, 126].

Second-order Lagrangean finite difference methods do not have total variation diminishing properties. So, they requires explicit additional numerical diffusion. As the grid is advecting, which makes the handling of marginal lines, along which the avalanche thickness must vanish, easy, the Lagrangean integration technique is particularly appropriate for two-dimensional avalanche problems. Besides, the Lagrangean integration technique with

second order accuracy in the spatial finite difference operators and leap frog integration procedure in time yields accurate results whenever only dilational or, only compressional flows prevail.

This integration scheme was developed in the context of avalanche by Koch et al. (1994) [67], and Weiland et al. (1999) [128]. The two dimensional Lagrangean numerical scheme used by Koch et al. (1994) [67] was then improved and further extended by Gray et al. (1999) [32] for the study of the motion of free surface flow of granular avalanches over complex basal topography. Wieland et al. (1999) [128] implemented a mixed type of finite-volume finite difference scheme, explicit in time and spatially two-dimensional Lagrangean scheme to solve depth-averaged equations of the motion developed by Gray et al. (1999) [32]. For this, the avalanche is discretized into a finite number of triangular elements with moving grid that deforms with the motion [103].

4.2 Two-Dimensional NOC Schemes

A Brief Description: A second order accurate extension of Lax-Friedrichs scheme (1954) [69], i.e., one-dimensional non-oscillatory central differencing (NOC) scheme was proposed by Nessyahu and Tadmor (1990) [87]. Its two dimensional extension was proposed by Jiang and Tadmor (1998) [56] followed by some modifications by Lie and Noelle (2003) [72]. This scheme was used for numerical simulation of granular avalanche flows [103]. Since, in numerical schemes only values of the cell averages are available, with the concept of high-resolution methods the distribution of the physical variables over the cell can be reconstructed. The two-dimensional NOC scheme is a predictor-corrector method, as in the one-dimensional case, this consists of two steps: (i) First, the grid values are predicted according to the non-oscillatory reconstructions from the given cell averages. (ii) At the second corrector step, a staggered averaging is introduced, together with the predicted mid-values, to determine the full evolution of these averages. This results in a high-order, non-oscillatory central scheme.

For the sake of simplicity, the x-y-t space is discretized by considering uniform and stationary width Δx, Δy and time step Δt. The discrete mesh points will be denoted by (x_p, y_q, t^n) and are defined as $x_p = p\Delta x$, $p = 0, 1, 2, ...$; $y_q = q\Delta y$, $q = 0, 1, 2, ...$; $t^n = n\Delta t$, $n = 0, 1, 2, ...$, where the mesh cell (x_p, y_q) is bounded by the boundaries $(x_{p\pm\frac{1}{2}}, y_{q\pm\frac{1}{2}})$, where $x_{p+\frac{1}{2}} = x_p + \frac{\triangle x}{2}$, etc. The main feature of this scheme is that the staggered averages at $(x_{p\pm1/2}, y_{q\pm1/2}, t^{n+1})$ are computed by the cell averages at (x_p, y_q, t^n), see Fig. 4.1**a**.

For this, we start with a general two-dimensional conservation law:

$$\frac{\partial w}{\partial t} + \frac{\partial f(w)}{\partial x} + \frac{\partial g(w)}{\partial y} = s(w), \tag{4.1}$$

subject to prescribed initial data, $w(x,\, y,\, t=0) = w_0\,(x,\, y)$. Let $C_{p,q}$ be the $(p,q)^{th}$ cell covered region,

$$C_{p,q} = \left\{ (x,\, y) \,\middle|\, |x - x_p| \leq \frac{\Delta x}{2},\ |y - y_q| \leq \frac{\Delta y}{2} \right\}. \tag{4.2}$$

Further let $U^n_{p,q}$ denote the cell average over this region at time t^n, and

$$\tilde{w}_{p,q}(x,\, y,\, t^n) = U^n_{p,q} + \sigma^x_{p,q}(x - x_p) + \sigma^y_{p,q}(y - y_q),\ \text{for}\ \ (x,y) \in C_{p,q}, \tag{4.3}$$

be a piecewise linear reconstruction over the cell, where $\sigma^x_{p,q}$ and $\sigma^y_{p,q}$ respectively denote the discrete slopes of U in the x- and y-directions which are determined by a TVD-limiter [71], or a central, Essentially Non-Oscillatory (ENO) cell reconstruction [37]. In the TVD schemes, they are the TVD slope limiters and in the ENO schemes they are the mean slopes of the high-order interpolations over the cells [103].

The piecewise linear cell reconstructions are at most of second-order accuracy. With the help of ENO schemes, it is possible to construct a polynomial approximation over the cell that is accurate pointwise to higher order. In the ENO schemes were first developed by Harten (1983) [37], the cell reconstructions are approximated by an essentially non-oscillatory high-order accurate polynomial interpolation of a piecewise smooth function from its cell averages. So, it is a generalization of the TVD method of piecewise linear cell reconstructions. The second-order ENO scheme results in a piecewise linear cell reconstruction, equivalent to a TVD method with a cell reconstruction determined by some suitable limiters. In what follows, the third-order quadratic ENO cell reconstruction is employed, for details see Harten (1983) [37], Pudasaini and Hutter (2007) [103] and, Wang et al. [126].

Let $U_{p+1/2,\,q+1/2}$ be the staggered average. Then, integration of (4.1) over $C_{p+1/2,\,q+1/2} \times [t^n,\, t^{n+1}]$ provides

$$\begin{aligned}
U^{n+1}_{p+1/2,\,q+1/2} &= \frac{1}{\Delta x\,\Delta y}\int_{x_p}^{x_{p+1}}\int_{y_q}^{y_{q+1}} w(x,\, y,\, t^n)dx\,dy \\
&- \frac{1}{\Delta x \Delta y}\int_{t^n}^{t^{n+1}}\int_{y_q}^{y_{q+1}} \left(f(x_{p+1},\, y,\, t) - f(x_p,\, y,\, t)\right) dy\,dt \\
&- \frac{1}{\Delta x \Delta y}\int_{t^n}^{t^{n+1}}\int_{x_p}^{x_{p+1}} \left(g(x,\, y_{q+1},\, t) - g(x,\, y_q,\, t)\right) dx\,dt \\
&+ \frac{1}{\Delta x \Delta y}\int_{t^n}^{t^{n+1}}\int_{x_p}^{x_{p+1}}\int_{y_q}^{y_{q+1}} s(x,\, y,\, t)dx\,dy\,dt.
\end{aligned} \tag{4.4}$$

We can now split the first integral on the right-hand side of (4.4) into the four parts as:

$$\int_{x_p}^{x_{p+1}}\int_{y_q}^{y_{q+1}} w(x,\, y,\, t^n)\, dx\, dy = \iint\limits_{C^{SW}_{p,q}} w(x,\, y,\, t^n)\, dx\, dy + \iint\limits_{C^{SE}_{p+1,q}} w(x,\, y,\, t^n)\, dx\, dy + \iint\limits_{C^{NE}_{p+1,q+1}} w(x,\, y,\, t^n)\, dx\, dy + \iint\limits_{C^{NW}_{p,q+1}} w(x,\, y,\, t^n)\, dx\, dy. \tag{4.5}$$

As shown in Fig. 4.1**b**, the four cells are defined by:

$$\begin{aligned} C^{SW}_{p,q} &:= C_{p+1/2,q+1/2} \cap C_{p,q}, \\ C^{SE}_{p+1,q} &:= C_{p+1/2,q+1/2} \cap C_{p+1,q}, \\ C^{NE}_{p+1,q+1} &:= C_{p+1/2,q+1/2} \cap C_{p+1,q+1}, \\ C^{NW}_{p,q+1} &:= C_{p+1/2,q+1/2} \cap C_{p,q+1}. \end{aligned} \tag{4.6}$$

If we begin with the intersection cell $C^{SW}_{p,q}$, by using the reconstructed polynomial (4.3) and the discrete slopes $\sigma^x_{j,k}$ and $\sigma^y_{j,k}$ of U, the first term on the right-hand side of (4.5) can be written as [103]:

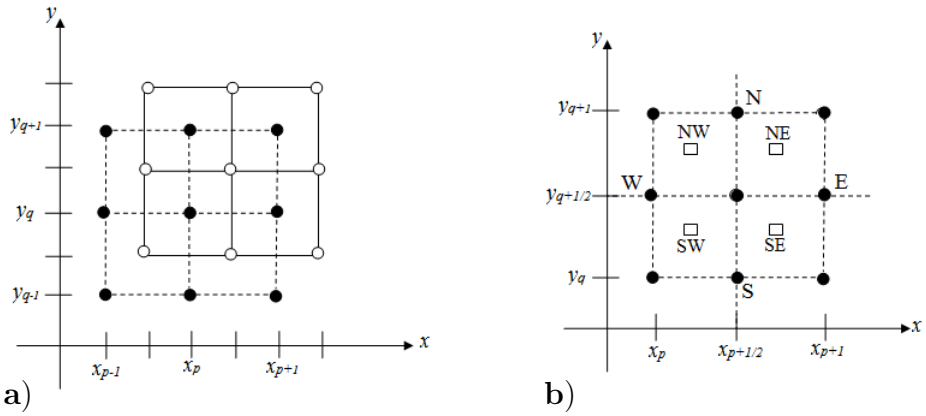

Figure 4.1: **a**) The two-dimensional NOC scheme with the staggered grid: The staggered averages at $(x_{p\pm1/2}, y_{q\pm1/2}, t^{n+1})$, denoted by "$\circ$", are computed by the averages at (x_p, y_q, t^n), represented by "$\bullet$". **b**) The two-dimensional NOC scheme and a floor plan of the staggered grid where, the cell $C_{p+1/2,\,q+1/2}$ consists of four intersecting cells $C_{p,q}$, $C_{p+1,q}$, $C_{p+1,q+1}$ and $C_{p,q+1}$, denoted by $C^{SW}_{p,q}$, $C^{SE}_{p+1,q}$, $C^{NE}_{p+1,q+1}$ and $C^{NW}_{p,q+1}$, respectively. "$\bullet$" indicates the computed cell center and "$\square$" denotes the center of the intersecting cell. The numerical fluxes are considered as the values across the corresponding faces, east (E), north (N), west (W) and south (S), respectively. (The figure has been reproduced from Pudasaini and Hutter (2007) [103]).

$$\frac{1}{4}U^n_{p,q} + \frac{\Delta x}{16}\sigma^x_{p,q} + \frac{\Delta y}{16}\sigma^y_{p,q}. \tag{4.7}$$

The same procedure applied in counterclockwise direction results the remaining terms on the right-hand side of (4.5) as [103]:

$$\begin{aligned}
&\frac{1}{4}U^n_{p+1,q} - \frac{\Delta x}{16}\sigma^x_{p+1,q} + \frac{\Delta y}{16}\sigma^y_{p+1,q},\\
&\frac{1}{4}U^n_{p+1,q+1} - \frac{\Delta x}{16}\sigma^x_{p+1,q+1} - \frac{\Delta y}{16}\sigma^y_{p+1,q+1},\\
&\frac{1}{4}U^n_{p,q+1} + \frac{\Delta x}{16}\sigma^x_{p,q+1} - \frac{\Delta y}{16}\sigma^y_{p,q+1}.
\end{aligned} \tag{4.8}$$

In the next step numerical fluxes corresponding to the points $x_{p+1}, x_p, y_{q+1}, y_q$ for (4.4) on the east and west surfaces for the flux function f, and north and south surfaces for the flux function g are computed, see, Fig. 4.1**b**. These are approximated by the midpoint quadrature rule for second-order accuracy by integrating with respect to time along with the second-order rectangular rule for the spatial integration across the corresponding face. So, the flux at the east face is:

$$\frac{1}{2}\frac{\Delta t}{\Delta x}\left\{f\left(U^{n+1/2}_{p+1,q}\right) + f\left(U^{n+1/2}_{p+1,q+1}\right)\right\}. \tag{4.9}$$

Similarly, the other three fluxes in the counterclockwise direction are [103]:

$$\begin{aligned}
&\frac{1}{2}\frac{\Delta t}{\Delta y}\left\{g\left(U^{n+1/2}_{p,q+1}\right) + g\left(U^{n+1/2}_{p+1,q+1}\right)\right\},\\
&\frac{1}{2}\frac{\Delta t}{\Delta x}\left\{f\left(U^{n+1/2}_{p,q}\right) + f\left(U^{n+1/2}_{p,q+1}\right)\right\},\\
&\frac{1}{2}\frac{\Delta t}{\Delta y}\left\{g\left(U^{n+1/2}_{p,q}\right) + g\left(U^{n+1/2}_{p+1,q}\right)\right\}.
\end{aligned} \tag{4.10}$$

Predictor-Step: Now, by making the use of the conservation law (4.1) to compute $U^{n+1/2}_{j,k}$, (4.9)–(4.10) gives [56, 87, 103]:

$$U^{n+1/2}_{j,k} = U^n_{j,k} - \frac{\Delta t}{2}\left(\sigma^f\right)^n_{j,k} - \frac{\Delta t}{2}\left(\sigma^g\right)^n_{j,k} + \frac{\Delta t}{2}s\big(U^n_{j,k}\big), \tag{4.11}$$

where σ^f and σ^g are the discrete slopes of the fluxes f and g.

By the non-oscillatory TVD limiters or ENO interpolations, or by the Jacobians, these can be determined as,

$$\left(\sigma^f\right)^n_{j,k} = \left(\frac{\partial f(w)}{\partial w}\right)^n_{j,k}\sigma^x_{j,k}, \qquad \left(\sigma^g\right)^n_{j,k} = \left(\frac{\partial g(w)}{\partial w}\right)^n_{j,k}\sigma^y_{j,k}, \tag{4.12}$$

where $\sigma^x_{j,k}$ and $\sigma^y_{j,k}$ are the discrete slopes of U [56, 87, 103].

Now, the integration of the source term is needed. Combining contributions from the four intersecting cells, and approximating by the values at the centers of all the four intersecting cells [103], (Fig. 4.1**b**), we get

$$\begin{aligned}
&\frac{1}{\Delta x \Delta y}\int_{t_n}^{t^{n+1}}\int_{x_p}^{x_{p+1}}\int_{y_q}^{y_{q+1}} s(x,\, y,\, t)dy\, dx\, dt \\
&= \frac{\Delta t}{4}\left\{ s\left(U^{n+1/2}_{p+1/4,q+1/4}\right) + s\left(U^{n+1/2}_{p+3/4,q+1/4}\right)\right. \\
&\qquad \left. + s\left(U^{n+1/2}_{p+3/4,q+3/4}\right) + s\left(U^{n+1/2}_{p+1/4,q+3/4}\right)\right\}. \qquad (4.13)
\end{aligned}$$

Using a Taylor series expansion to compute the values of $U^{n+1/2}_{p+1/4,q+1/4}$, we get

$$U^{n+1/2}_{p+1/4,q+1/4} = U^{n+1/2}_{p,q} + \frac{\Delta x}{4}\left(\sigma^x\right)^n_{p,q} + \frac{\Delta y}{4}\left(\sigma^y\right)^n_{p,q}. \qquad (4.14)$$

Hence, continuing in counterclockwise direction, all the arguments appearing in (4.13) are obtained as [103]:

$$\begin{aligned}
U^{n+1/2}_{p+1/4,q+1/4} &= U^{n+1/2}_{p,q} + \frac{\Delta x}{4}\left(\sigma^x\right)^n_{p,q} + \frac{\Delta y}{4}\left(\sigma^y\right)^n_{p,q}, \\
U^{n+1/2}_{p+3/4,q+1/4} &= U^{n+1/2}_{p+1,q} - \frac{\Delta x}{4}\left(\sigma^x\right)^n_{p+1,q} + \frac{\Delta y}{4}\left(\sigma^y\right)^n_{p+1,q}, \\
U^{n+1/2}_{p+3/4,q+3/4} &= U^{n+1/2}_{p+1,q+1} - \frac{\Delta x}{4}\left(\sigma^x\right)^n_{p+1,q+1} - \frac{\Delta y}{4}\left(\sigma^y\right)^n_{p+1,q+1}, \\
U^{n+1/2}_{p+1/4,q+3/4} &= U^{n+1/2}_{p,q+1} + \frac{\Delta x}{4}\left(\sigma^x\right)^n_{p,q+1} - \frac{\Delta y}{4}\left(\sigma^y\right)^n_{p,q+1}.
\end{aligned} \qquad (4.15)$$

Corrector-Step: The results in (4.7)-(4.8) and (4.9)-(4.10) show that the two-dimensional NOC scheme has the first-order predictors (4.11), (4.15), and the second-order corrector steps, for the cell-mean value at the staggered grid point $(x_{p+1/2},\, q_{q+1/2},\, t^{n+1})$ [103]

$$
\begin{aligned}
&U^{n+1}_{p+1/2,\,q+1/2} \\
&= \frac{1}{4}\left\{U^{n}_{p,q}+U^{n}_{p+1,q}+U^{n}_{p+1,q+1}+U^{n}_{p,q+1}\right\} \\
&+\frac{\Delta x}{16}\left\{\sigma^{x}_{p,q}-\sigma^{x}_{p+1,q}-\sigma^{x}_{p+1,q+1}+\sigma^{x}_{p,q+1}\right\} \\
&+\frac{\Delta y}{16}\left\{\sigma^{y}_{p,q}+\sigma^{y}_{p+1,q}-\sigma^{y}_{p+1,q+1}-\sigma^{y}_{p,q+1}\right\} \\
&-\frac{\Delta t}{2\Delta x}\left\{f\left(U^{n+1/2}_{p+1,q}\right)+f\left(U^{n+1/2}_{p+1,q+1}\right)-f\left(U^{n+1/2}_{p,q}\right)-f\left(U^{n+1/2}_{p,q+1}\right)\right\} \\
&-\frac{\Delta t}{2\Delta y}\left\{g\left(U^{n+1/2}_{p,q+1}\right)+g\left(U^{n+1/2}_{p+1,q+1}\right)-g\left(U^{n+1/2}_{p,q}\right)-g\left(U^{n+1/2}_{p+1,q}\right)\right\} \\
&+\frac{\Delta t}{4}\left\{s\left(U^{n+1/2}_{p+1/4,q+1/4}\right)+s\left(U^{n+1/2}_{p+3/4,q+1/4}\right)\right. \\
&\qquad \left.+s\left(U^{n+1/2}_{p+3/4,q+3/4}\right)+s\left(U^{n+1/2}_{p+1/4,q+3/4}\right)\right\}. \qquad (4.16)
\end{aligned}
$$

Thus, this resulting scheme is a high-order accurate non-oscillatory, and also strongly depends on the reconstructed discrete slopes, σ^x, σ^y, σ^f and σ^g.

CFL Condition: For the sake of numerical stability, the schemes (4.11) and (4.16) must satisfy the Courant-Friedich-Levy (CFL) condition:

$$\max\left(\frac{\Delta t}{\Delta x}\frac{\partial f}{\partial w},\ \frac{\Delta t}{\Delta y}\frac{\partial g}{\partial w}\right)\leq 1/2. \qquad (4.17)$$

This condition has been confirmed by numerical tests performed by Jiang and Tadmor (1998) [56] with the simple linear scalar advection equation [103].

4.3 Application of 2D Shock-Capturing Methods to the General Two-Phase Debris Flows

Here, the two-dimensional NOC scheme discussed at §4.2 is applied to the two-dimensional general two phase debris flows down an inclined channel proposed by Pudasaini (2012) [98]. The model equations (3.8)-(3.13) are again mentioned:

$$\frac{\partial}{\partial t}(\alpha_s h)+\frac{\partial}{\partial x}(\alpha_s h u_s)+\frac{\partial}{\partial y}(\alpha_s h v_s)=0, \qquad (4.18)$$

$$\frac{\partial}{\partial t}(\alpha_f h)+\frac{\partial}{\partial x}(\alpha_f h u_f)+\frac{\partial}{\partial y}(\alpha_f h v_f)=0, \qquad (4.19)$$

$$\frac{\partial}{\partial t}\left[\alpha_s h(u_s-\gamma\mathcal{C}\left(u_f-u_s\right))\right]+\frac{\partial}{\partial x}\left[\alpha_s h\left(u_s^2-\gamma\mathcal{C}(u_f^2-u_s^2)+\frac{\beta_{x_s}h}{2}\right)\right]$$
$$+\frac{\partial}{\partial y}\left[\alpha_s h(u_s v_s-\gamma\mathcal{C}(u_f v_f-u_s v_s))\right]=hS_{x_s}, \tag{4.20}$$

$$\frac{\partial}{\partial t}\left[\alpha_s\, h\left(v_s-\gamma\mathcal{C}\left(v_f-v_s\right)\right)\right]+\frac{\partial}{\partial x}\left[\alpha_s h(u_s\, v_s-\gamma\mathcal{C}(u_f v_f-u_s v_s))\right]$$
$$+\frac{\partial}{\partial y}\left[\alpha_s h\left(v_s^2-\gamma\mathcal{C}(v_f^2-v_s^2)+\frac{\beta_{y_s}h}{2}\right)\right]=hS_{y_s}, \tag{4.21}$$

$$\frac{\partial}{\partial t}\left[\alpha_f h\left(u_f+\frac{\alpha_s}{\alpha_f}\mathcal{C}(u_f-u_s)\right)\right]+\frac{\partial}{\partial x}\left[\alpha_f h\left(u_f^2+\frac{\alpha_s}{\alpha_f}\mathcal{C}(u_f^2-u_s^2)+\frac{\beta_{x_f}h}{2}\right)\right]$$
$$+\frac{\partial}{\partial y}\left[\alpha_f h\left(u_f v_f+\frac{\alpha_s}{\alpha_f}\mathcal{C}(u_f v_f-u_s v_s)\right)\right]=hS_{x_f}, \tag{4.22}$$

$$\frac{\partial}{\partial t}\left[\alpha_f h\left(v_f+\frac{\alpha_s}{\alpha_f}\mathcal{C}(v_f-v_s)\right)\right]+\frac{\partial}{\partial x}\left[\alpha_f h\left(u_f v_f+\frac{\alpha_s}{\alpha_f}\mathcal{C}(u_f v_f-u_s v_s)\right)\right]$$
$$+\frac{\partial}{\partial y}\left[\alpha_f h\left(v_f^2+\frac{\alpha_s}{\alpha_f}\mathcal{C}(v_f^2-v_s^2)+\frac{\beta_{y_f}h}{2}\right)\right]=hS_{y_f}, \tag{4.23}$$

where,

$$\beta_{x_s}=\varepsilon K_x p_{b_s},\quad \beta_{y_s}=\varepsilon K_y p_{b_s},\quad \beta_{x_f}=\beta_{y_f}=\varepsilon p_{b_f}\quad p_{b_f}=-g^z,\quad p_{b_s}=(1-\gamma)p_{b_f},$$

with the source terms s_{x_s}, s_{x_f}, s_{y_s} and s_{y_f}. The above six equations can be written in a compact vectorial form, as [98, 103]

$$\frac{\partial\mathbf{T}(\mathbf{w})}{\partial t}+\frac{\partial\mathbf{f}\left(\mathbf{w}\right)}{\partial x}+\frac{\partial\mathbf{g}\left(\mathbf{w}\right)}{\partial y}=\mathbf{s}(\mathbf{w}), \tag{4.24}$$

where, $\mathbf{w}$ denotes the vector of conservative variables h_s, h_f, $m_{x_s}(=h_s u_s)$, $m_{x_f}(=h_f u_f)$, $m_{y_s}(=h_s v_s)$ and $m_{y_f}(=h_f v_f)$. Also, $\mathbf{f}$ and $\mathbf{g}$ are the transport fluxes in the x- and y-directions, respectively, and $\mathbf{s}$ is the source term, i.e.,

$$\mathbf{T}(\mathbf{w})=\begin{pmatrix} h_s \\ h_f \\ m_{x_s}-\gamma\mathcal{C}\left(m_{x_f}h_s/h_f-m_{x_s}\right) \\ m_{y_s}-\gamma\mathcal{C}\left(m_{y_f}h_s/h_f-m_{y_s}\right) \\ m_{x_f}+\mathcal{C}\left(m_{x_f}h_s/h_f-m_{x_s}\right) \\ m_{y_f}+\mathcal{C}\left(m_{y_f}h_s/h_f-m_{y_f}\right) \end{pmatrix},\quad \mathbf{w}=\begin{pmatrix} h_s \\ h_f \\ m_{x_s} \\ m_{y_s} \\ m_{x_f} \\ m_{y_f} \end{pmatrix},$$

$$\mathbf{f}=\begin{pmatrix} m_{x_s} \\ m_{x_f} \\ m_{x_s}^2/h_s-\gamma\mathcal{C}\Big(m_{x_f}^2h_s/h_f^2-m_{x_s}^2/h_s\Big)+\beta_{x_s}h_sh/2 \\ m_{x_s}m_{y_s}/h_s-\gamma\mathcal{C}\Big(m_{x_f}m_{y_f}h_s/h_f^2-m_{x_s}m_{y_s}/h_s\Big) \\ m_{x_f}^2/h_f+\mathcal{C}\Big(m_{x_f}^2h_s/h_f^2-m_{x_s}^2/h_s\Big)+\beta_{x_f}h_fh/2 \\ m_{x_f}m_{y_f}/h_f+\mathcal{C}\Big(m_{x_f}m_{y_f}h_s/h_f^2-m_{x_s}m_{y_s}/h_s\Big) \end{pmatrix},$$

$$\mathbf{g}=\begin{pmatrix} m_{y_s} \\ m_{y_f} \\ m_{x_s}m_{y_s}/h_s-\gamma\mathcal{C}\Big(m_{x_f}m_{y_f}h_s/h_f^2-m_{x_s}m_{y_s}/h_s\Big) \\ m_{y_s}^2/h_s-\gamma\mathcal{C}\Big(m_{x_f}^2h_s/h_f^2-m_{y_s}^2/h_s\Big)+\beta_{y_s}h_sh/2 \\ m_{x_f}m_{y_f}/h_f+\mathcal{C}\Big(m_{x_f}m_{y_f}h_s/h_f^2-m_{x_s}m_{y_s}/h_f\Big) \\ m_{x_f}^2/h_f+\mathcal{C}\Big(m_{y_f}^2h_s/h_f^2-m_{y_s}^2/h_s\Big)+\beta_{y_f}h_fh/2 \end{pmatrix}, \quad \mathbf{s}=\begin{pmatrix} 0 \\ 0 \\ hS_{x_s} \\ hS_{y_s} \\ hS_{x_f} \\ hS_{y_f} \end{pmatrix}, \tag{4.25}$$

where these expressions are computed in the conservative variables. The main advantage of writing the two-phase debris flow model in standard, well-structured conservative form is that the higher-order shock-capturing (TVD-NOC) scheme can directly be applied to the model equation [98], as the main target of this section.

From (4.16), the cell average $\mathbf{w}_{p+1/2,\,q+1/2}^{n+1}$ at $\left(x_{p+1/2}, y_{q+1/2}, t^{n+1}\right)$ is given by [103]

$$\begin{aligned}
&\mathbf{w}_{p+1/2,\,q+1/2}^{n+1} \\
&\quad=\frac{1}{4}\left\{\mathbf{w}_{p,q}^{n}+\mathbf{w}_{p+1,q}^{n}+\mathbf{w}_{p+1,q+1}^{n}+\mathbf{w}_{p,q+1}^{n}\right\} \\
&\quad+\frac{\Delta x}{16}\left\{\mathbf{w}_{p,q}^{x}-\mathbf{w}_{p+1,q}^{x}-\mathbf{w}_{p+1,q+1}^{x}+\mathbf{w}_{p,q+1}^{x}\right\} \\
&\quad+\frac{\Delta y}{16}\left\{\mathbf{w}_{p,q}^{y}+\mathbf{w}_{p+1,q}^{y}-\mathbf{w}_{p+1,q+1}^{y}-\mathbf{w}_{p,q+1}^{y}\right\} \\
&\quad-\frac{\Delta t}{2\Delta x}\left\{\mathbf{f}\left(\mathbf{w}_{p+1,q}^{n+1/2}\right)+\mathbf{f}\left(\mathbf{w}_{p+1,q+1}^{n+1/2}\right)-\mathbf{f}\left(\mathbf{w}_{p,q}^{n+1/2}\right)-\mathbf{f}\left(\mathbf{w}_{p,q+1}^{n+1/2}\right)\right\} \\
&\quad-\frac{\Delta t}{2\Delta y}\left\{\mathbf{g}\left(\mathbf{w}_{p,q+1}^{n+1/2}\right)+\mathbf{g}\left(\mathbf{w}_{p+1,q+1}^{n+1/2}\right)-\mathbf{g}\left(\mathbf{w}_{p,q}^{n+1/2}\right)-\mathbf{g}\left(\mathbf{w}_{p+1,q}^{n+1/2}\right)\right\} \\
&\quad+\frac{\Delta t}{4}\left\{\mathbf{s}\left(\mathbf{w}_{p+1/4,q+1/4}^{n+1/2}\right)+\mathbf{s}\left(\mathbf{w}_{p+3/4,q+1/4}^{n+1/2}\right)\right. \\
&\qquad\left.+\mathbf{s}\left(\mathbf{w}_{p+3/4,q+3/4}^{n+1/2}\right)+\mathbf{s}\left(\mathbf{w}_{p+1/4,q+3/4}^{n+1/2}\right)\right\}.
\end{aligned} \tag{4.26}$$

In (4.26), we take $j=p,\ p+1$ and $k=q,\ q+1$, and

$$\mathbf{w}_{j,k}^{x}=\boldsymbol{\sigma}_{j,k}^{x}, \qquad \mathbf{w}_{j,k}^{y}=\boldsymbol{\sigma}_{j,k}^{y} \tag{4.27}$$

are the mean discrete derivatives over the cell in the x- and y-directions, respectively. The cell average at time level $t^{n+1/2}$, as in (4.11), is given by:

$$\mathbf{w}_{j,k}^{n+1/2} = \mathbf{w}_{j,k}^{n} + \frac{\Delta t}{2}\left(\frac{\partial \mathbf{w}}{\partial t}\right)_{j,k}^{n}, \tag{4.28}$$

by using conservation law (4.1). In (4.28), the temporal derivative is approximated by

$$\left(\frac{\partial \mathbf{w}}{\partial t}\right)_{j,k}^{n} = -\left(\sigma^{\mathbf{f}}\right)_{j,k}^{n} - \left(\sigma^{\mathbf{g}}\right)_{j,k}^{n} + \mathbf{s}\left(\mathbf{w}_{j,k}^{n}\right), \tag{4.29}$$

where, $\sigma^{\mathbf{f}}$ and $\sigma^{\mathbf{g}}$ are the one-dimensional discrete slopes of the fluxes.

By applying the cell reconstructions along with the predicted values (4.28), the arguments for the source term in (4.26) are given by [103]:

$$\begin{aligned}
\mathbf{w}_{p+1/4,q+1/4}^{n+1/2} &= \mathbf{w}_{p,q}^{n+1/2} + \frac{\Delta x}{4}\mathbf{w}_{p,q}^{x} + \frac{\Delta y}{4}\mathbf{w}_{p,q}^{y},\\
\mathbf{w}_{p+3/4,q+1/4}^{n+1/2} &= \mathbf{w}_{p+1,q}^{n+1/2} - \frac{\Delta x}{4}\mathbf{w}_{p+1,q}^{x} + \frac{\Delta y}{4}\mathbf{w}_{p+1,q}^{y},\\
\mathbf{w}_{p+3/4,q+3/4}^{n+1/2} &= \mathbf{w}_{p+1,q+1}^{n+1/2} - \frac{\Delta x}{4}\mathbf{w}_{p+1,q+1}^{x} - \frac{\Delta y}{4}\mathbf{w}_{p+1,q+1}^{y},\\
\mathbf{w}_{p+1/4,q+3/4}^{n+1/2} &= \mathbf{w}_{p,q+1}^{n+1/2} + \frac{\Delta x}{4}\mathbf{w}_{p,q+1}^{x} - \frac{\Delta y}{4}\mathbf{w}_{p,q+1}^{y}.
\end{aligned} \tag{4.30}$$

The CFL Condition: The NOC scheme developed above must satisfy the CFL condition

$$\frac{\Delta t}{\Delta x}\left|C^{\max}\right| < \frac{1}{2}, \qquad \text{for all} \quad p, \tag{4.31}$$

with the possible global maximum wave speeds

$$C^{\max} = \max\{C_s^{\max}, C_f^{\max}\},\ C_s^{\max} = \max\{\lambda_1, \lambda_2\},\ C_f^{\max} = \max\{\lambda_3, \lambda_4\},$$

over the whole computational domain (in the x-direction), where $\lambda_{1,2}, \lambda_{3,4}$ are the associated general wave speeds for the solid and the fluid phases in the two-phase mass flows [94]:

$$\lambda_{(1,2)} = \frac{-g_1 \pm \sqrt{g_1^2 - 4h_1}}{2}, \tag{4.32}$$

$$\lambda_{(3,4)} = \frac{-g_2 \pm \sqrt{g_2^2 - 4h_2}}{2}, \tag{4.33}$$

where

$$g_{(1,2)} = \frac{a \pm \sqrt{a^2 - \dfrac{8b}{3} + 4y_s}}{2}, \tag{4.34}$$

$$h_{(1,2)} = \frac{y_s + \dfrac{b}{3} \pm \sqrt{\left(y_s + \dfrac{b}{3}\right)^2 - 4d}}{2}. \tag{4.35}$$

and, y_s is given by

$$y_s = 2\left(\frac{a^2 d}{2} + \frac{c^2}{2} + \frac{b^3}{27} - \frac{abc}{6} - \frac{4bd}{3}\right)^{\frac{1}{3}},$$

where,

$$\begin{aligned}
a &= -2(u_s + u_f), \\
b &= u_s^2 + 4u_s u_f + u_f^2 - h_s(\beta_{x_s} + 0.5\beta_{x_f}) - h_f(\beta_{x_f} + 0.5\beta_{x_s}), \\
c &= -2u_s u_f^2 - 2u_s^2 u_f + 2h_s\beta_{x_s} u_f + h_s\beta_{x_f} u_s + 2h_f\beta_{x_f} u_s + h_f\beta_{x_s} u_f, \\
d &= -0.5h_f\beta_{x_s} u_f^2 - h_s\beta_{x_s} u_f^2 - 0.5h_s\beta_{x_f} u_s^2 - h_f\beta_{x_f} u_s^2 + 0.5h_s^2\beta_{x_s}\beta_{x_f} \\
&\quad + h_s h_f\beta_{x_s}\beta_{x_f} + 0.5h_f\beta_{x_s}\beta_{x_f} + u_s^2 u_f^2.
\end{aligned}$$

For detailed derivations of these wave general speeds, one may to Pokhrel (2014) [94]. Similarly, eigenvalues associated with the y-direction can be obtained in the same manner [101].

Chapter 5

Simulation of Two-Phase Submarine Debris Flow and Super Tsunami

5.1 Some Aspects of Submarine Debris Flow and Tsunami

Numerical methods to solve avalanche and debris flow models have been developed from simple to complex and their history reflects as much the learning experience as that of the derivation of the equations themselves [103]. Early studies dealt with single-phase one-dimensional flows. Later sidewise confinement was relaxed allowing for the (geometrically) two- and three-dimensional simulations of rapid granular flows. Two-phase mass flow simulations are relatively new. The real two-phase debris mass flows were simulated by Pudasaini (2012, 2014) [98, 99] and by Pudasaini and Miller (2012a, b) [106, 107] for the first time for the explicit evolution of the solid and the fluid volume fractions as the debris mass collapses and slides down the slopes, for both the subaerial and submarine debris flows in geometrically two-dimensions. Particularly, Pudasaini and Miller (2012b) [107] and Pudasaini (2014) [99] simulated two-dimensional flows in which the two-phase subaerial debris flows hit the still reservoir in the downstream that produces tsunami waves as impact and the submarine debris mass slides along the bathymetric surface of the reservoir. Firstly, these simulations are briefly discussed. Then, it is advanced further by simulating two-phase, three-dimensional subaerial flows impacting a fluid reservoir. Three-dimensional tsunami generation, amplification, propagation, submarine debris flows, and the complex interactions between the tsunami and submarine debris waves have been analyzed in detail. Simulations are performed for different time steps and different parameter values. Some observable natural phenomena have been sim-

ulated here for the first time by using the real two-phase debris flow model of Pudasaini (2012) [98] together with a high resolution shock capturing scheme [103] applied to the real two-phase mass flow simulations [99, 107].

5.2 Two-Dimensional Simulation

There have been several research works in the field of debris flows and tsunamis. However, explicit simulation of real two-phase debris flow is relatively new. Recently, by using the general two-phase debris flow model by Pudasaini (2012) [98], Pudasaini and Miller (2012b) [107] and Pudasaini (2014) [99] simulated the two-dimensional tsunami waves generated by the impact of the subaerial two-phase debris mass at the still fluid reservoir in the downstream. They studied, in detail, the subaerial and submarine debris flows, and the tsunami generated by the debris impact at lakes, and oceans. This two-phase debris flow model is advantageous as compared to the classical single-phase, or quasi-two-phase models. The advantage is that the initial mass can be divided into several parts by appropriately considering the solid volume fraction [99, 107]. These parts include a dry (landslide or, rock slide), a fluid (water or, muddy water; e.g., reservoir, rivers), and a general debris mixture material as required in real flow simulations. By means of this formulation, the sliding debris or landslide, the water lake or reservoir, the impact of the debris at the lake or reservoir, the tsunami initiation and propagation, the mixing and the separation of solid and fluid phases and the sediment transport and deposition process in the bathymetric surface can be simulated simultaneously and within a single framework [99].

Let us consider a two-phase subaerial debris flow that hits a quiescent fluid reservoir in the downstream as shown in Fig. 5.1. The upper part of the channel is inclined at $\zeta = 45°$. The initial triangle is uniformly filled with homogeneous mixture of 50% solid and 50% fluid. The reservoir consists of 98% fluid and 2% solid grains. The parameter values are: $\phi = 35°$, $\delta = 15°$, $\rho_f = 1,100$ kgm^3, $\rho_s = 2,500$ kgm^3, $N_R = 150,000$, $N_{R_{\mathcal{A}}} = 30$, $Re_p = 1$, $\mathcal{U}_T = 1$, $\mathcal{P} = 0.5$, $J = 1$, $\chi = 3$, $\xi = 5$, $\mathcal{C} = 0.5$ [107]. In this simulation (Fig. 5.1) the two-phase debris mass slides down and hits the reservoir and the water wave called tsunami, is generated. The fluid mass is mixed with water whereas the solid mass moves along and is deposited in the bottom of the reservoir. Two-phase subaerial debris flow hits a fluid reservoir ($t = 2$ s, i.e., panel **b**), generates tsunami wave, and a submarine debris wave continues to slide down. Orange and blue colors indicate volume fractions of solid and fluid. At $t = 5$ s (panel **c**), tsunami wave is found to be amplified, with an increasing hydrodynamic impact vacuum [99, 107]. There are three complex flows

taking place together: subaerial debris flow in the upstream, submarine debris flow in the downstream and at the reservoir floor, and the surface tsunami wave. At $t = 5$ s (panel **c**), the horizontal basin of the reservoir is hit by the submarine debris and the tsunami becomes a super wave. At $t = 7$ s (panel **d**), the submarine debris wave is moving much faster than the tsunami wave. At $t = 9$ s (panel **e**), a left-going water wave starts, and the hydrodynamic vacuum is found to be decreasing. It is observed that the submarine debris already hits the right wall of the dam but the tsunami is still following the debris mass. This time gap may be used to generate early warning signals [99]. At $t = 10$ s (panel **f**), the submarine debris hits the distal dam wall and a shock wave of debris material is generated that propagates upstream [107].

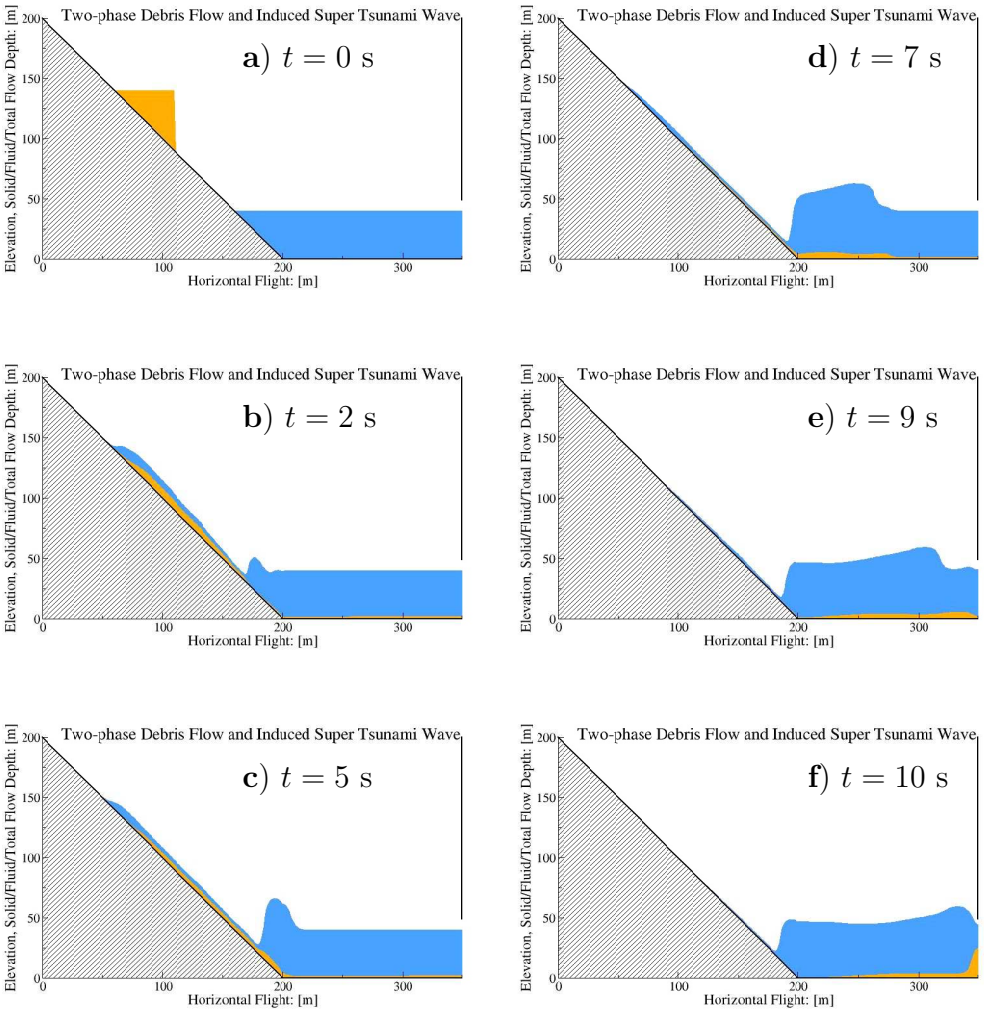

Figure 5.1: Two-phase subaerial debris flow hits a fluid reservoir, generates tsunami wave, and a submarine debris wave continues to slide down. Orange and blue colors indicate volume fractions of solid and fluid (Pudasaini and Miller, 2012b [107]).

5.3 Three-Dimensional Simulation

Here, focus is made on three-dimensional, two-phase flows and associated phenomena by simulating some basic three-dimensional subaerial and submarine debris flows, tsunami generation due to landslide impacts, and the submarine debris motion. Three-dimensional simulations are required for the description of the real flows in nature.

5.3.1 Numerical Method

As mentioned before, with the advancements of the numerical methods and computing techniques, scientific computing has perhaps become a dominant approach in describing and analyzing complex systems expressible in standard mathematical form, such as the non-linear partial differential equations governing an underlying process. In their full form, solving the model equations (3.8)-(3.13) analytically is not possible and would require further simplifications [64, 65, 66, 97, 103]. More appropriate would be to solve the equations numerically, by converting the physical problem in continuum mechanics expressed in terms of PDEs into a discrete form.

The model equations (3.8)-(3.13) are a set of well-structured, non-linear hyperbolic-parabolic partial differential equations in conservative form with complex source terms [98]. These model equations compute the debris depth h, solid volume fraction α_s, velocity components for solid u_s, v_s in x- and y-direction, and for fluid u_f, v_f in x- and y-directions, respectively, as functions of space and time. This facilitates numerical integration even when shocks are formed in the field variables [106, 107]. The model equations are solved in conservative variables $\mathbf{W} = (h_s, h_f, m_s, m_f)^t$, where $h_s = \alpha_s h$, $h_f = \alpha_f h$ are the solid and fluid contributions to the debris, or the flow height; and $m_s = \alpha_s h u_s$, $m_f = \alpha_f h u_f$, are the solid and fluid momenta. The high-resolution shock-capturing Total Variation Diminishing Non-Oscillatory Central (TVD-NOC) scheme explained in Chapter 4 is implemented [17, 97, 103, 123]. Advantages of the applied innovative and unified simulation technique for the real two-phase debris flows and the corresponding computational strategy have been explained in Pudasaini and Miller (2012b) [107] and Pudasaini (2014) [99] for two-dimensional simulations. This technique has been extended in Kattel et al. (2013) [61], Kattel (2014) [62] and Kattel et al. (2014) [60] for basic three-dimensional subaerial flows, and here, for submarine debris flows and subsequent tsunamis for more realistic and complex three-dimensional situations.

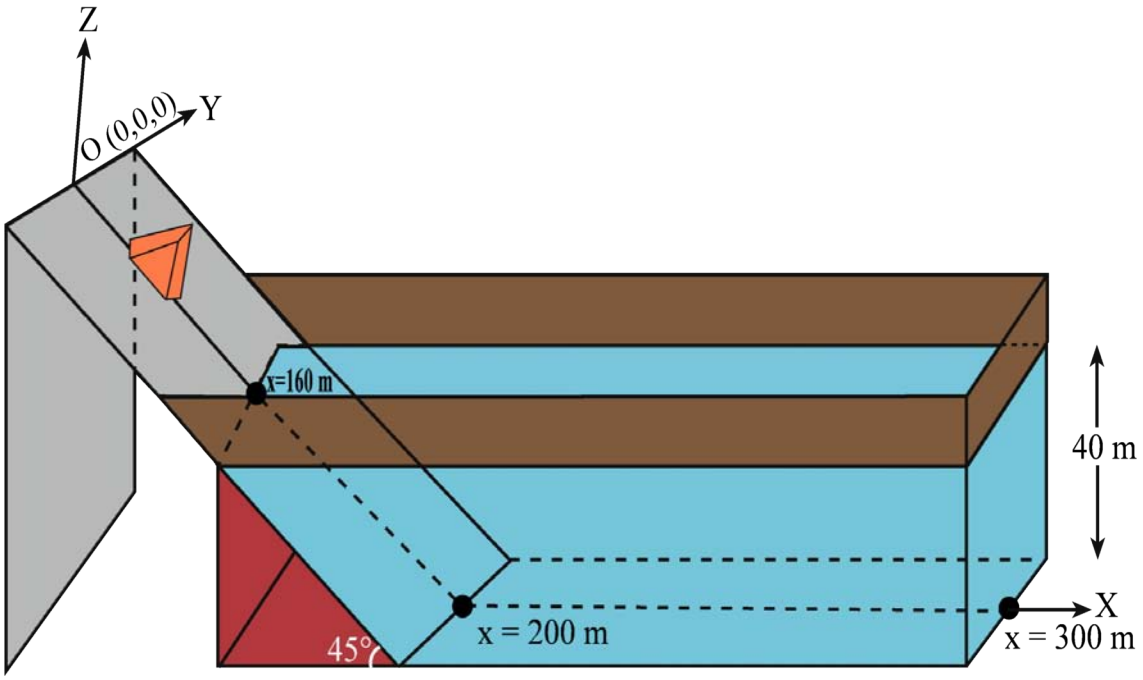

Figure 5.2: A sketch of the initial configuration of a debris mass on an inclined slab and a fluid reservoir in the downstream. As the debris moves down the slope and hits the fluid reservoir the tsunami waves will be generated (Kafle et al., 2014 [58]).

5.3.2 Simulation Set-up and Parameters

For simulation, a two-phase subaerial debris flow that hits a fluid reservoir in the downstream (Fig. 5.2) has been considered. The upper part of the channel is inclined ($\zeta = 45°$) and is flat in the lateral direction. The left end of the reservoir meets an inclined surface (plane) as shown in the Fig. 5.2. Initially, the left end of the reservoir has the water height zero, which, due to the slope, gradually increases to its maximum of $h = 40$ m from the down-slope coordinate $x = 160$ m to $x = 200$ m. Beyond this, the initial fluid height remains constant, i.e., $h = 40$ m from $x = 200$ m to $x = 300$ m.

The initial debris mass in the upper part of slope is uniformly distributed with homogeneous mixture of 70% solid and 30% fluid. The other parameter values chosen for simulation are [107]: $\phi = 35°$, $\delta = 15°$, $\rho_f = 1,100$ kgm^3, $\rho_s = 2,500$ kgm^3, $N_R = 277,500$, $N_{R_\mathcal{A}} = 5$, $Re_p = 1$, $\mathcal{U}_T = 1$, $\mathcal{P} = 0.5$, $J = 1$, $\chi = 0$, $\xi = 0$, $\mathcal{C} = 0$.

5.3.3 Simulation Results and Discussion

Simulation results for the evolution of the subaerial and submarine debris flows, and the tsunami generation by the debris impact and the subsequent complex fluid waves have

been presented here. The state of the solid (or, fluid) volume fraction is essential for the correct prediction of the turbidity currents, sediment transport and deposition in the subaerial and submarine environments [99]. Here, some basic results are presented in terms of the total debris depth (the sum of the solid and the fluid heights) along with the separate evolutions of the solid and the fluid phases, the penetration of the debris into the reservoir, and the motion of the submarine debris flows, and the complex wave interactions. For simplicity, the simulation results are plotted (Fig. 5.3 to Fig. 5.12) with a bird's eye perspective. However, the colour map clearly provides necessary information about the flow depth and the mass distribution. Here, for visualization, the colour patches are generated by filling the gaps between the contours.

I. Initially Constant Concentration of Solid in the Reservoir

Figure 5.3 shows that as the two-phase subaerial debris flow hits a still fluid reservoir, a tsunami wave is generated, and a submarine debris wave continues to propagate. A detailed analysis of the dynamics of the two-phase submarine debris is presented in [99, 107] for the two-dimensional flows. Here, the analysis is focused on the three-dimensional total debris depth evolution on the inclined surface, the instant when the flow impinges the fluid reservoir and the complex three-dimensional tsunami wave generation and their propagation off the impact region, both in the longitudinal direction and the lateral directions.

Initially at $t = 0$ s, (panel **a**), the debris material is released from a laterally-spanned triangular-wedge ($100 \leq x \leq 150$; $-10 \leq y \leq 10$). At $t = 0.5$ s (panel **b**), the debris just hits the center of the left coast of the reservoir to generate a tsunami. However, until now, the debris mass is only stretching and moving on the inclined plane, mainly in the down-slope direction, but also in the cross-slope direction, and that the reservoir yet remains unaffected. At this stage, as the mass has been continuously spread on the inclined plane, the subaerial debris depth has been substantially decreased.

The interesting point to observe here is the special evolution of the (subaerial) total debris: the debris height increases quickly from the front to the main body of the debris mass whose maximum height appears to be closer to the frontal part of the debris than to the middle part (Kafle et al., 2014 [59]). Then, the debris height decreases to form a relatively long tail in the back of the moving debris mass. These are the observed phenomena in the real two-phase debris mass movements [50, 98, 106, 108]. Such phenomenon has already been simulated for the real two-phase, but two-dimensional debris flows, in Pudasaini (2012) [98], Pudasaini et al. (2012a) [106] and Pudasaini (2014) [99]. However, this type

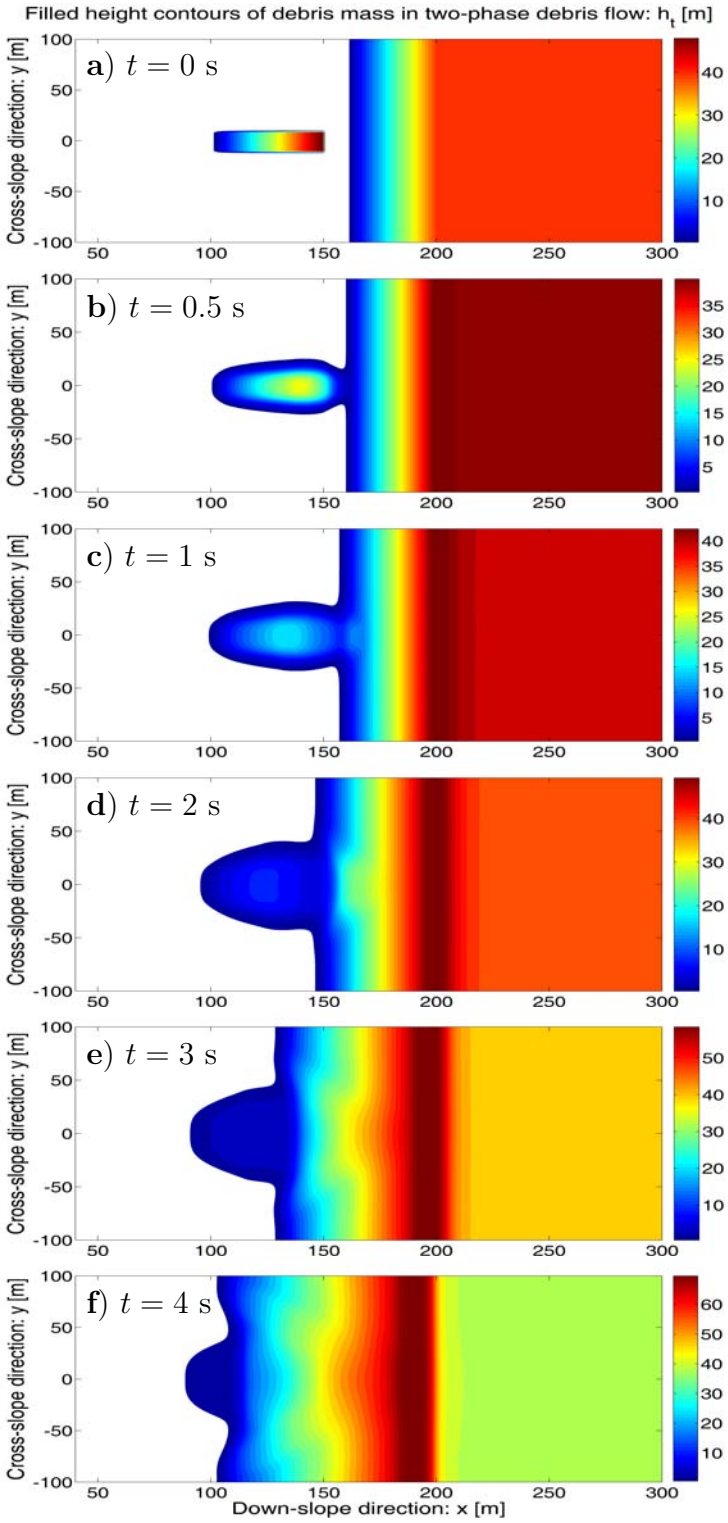

Figure 5.3: Total height of debris flow when the reservoir initially contains 2% solid grains. At $t = 0$ s, initial debris material (30% solid grains and 70% fluid) is released. At $t = 0.5$ s, the debris spreads downslope and crossslope directions and just hits the center of the left coast of the reservoir to generate a tsunami. At $t = 1$ s, the debris continues to hit the reservoir with higher momentum, the tsunami wave has been created in the vicinity of the impact. At $t = 2$ s and $t = 3$ s, the tsunami wave is amplified.

of special three-dimensional debris flow front surge-head followed by a long tail in the three-dimensional flow configuration, has for the first time, been systematically simulated and discussed in Kattel et al. (2013) [61], Kattel (2014) [60] and Kattel et al. (2014) [62].

As the debris hits the reservoir, the debris mass slides down the bathymetric slope as a submarine debris flow [99, 107] and the tsunami wave propagates. As the debris continues to hit the reservoir with higher momentum ($t = 1$ s, panel **c**), the tsunami wave has been created in the vicinity of the impact, and is amplified ($t = 2$ s, panel **d**) and more and more fluid mass from the left of the reservoir is pushed to the forward (right) and laterally. This produces a three-dimensional hydrodynamic impact vacuum, or crater [107], which increases in time and continues for quite a while. At a further instant, three complex flows occur simultaneously; including (*i*) subaerial debris flow in the upstream region, (*ii*) submarine debris flow in the downstream and in the reservoir basin, and (*iii*) a super tsunami wave on the surface of the reservoir. The height of the water surface has been substantially increased due to the tsunami wave and the pushing of the water to the right (up to a bit more than $x = 200$ m) resulting to the maximum fluid height of about 50 m around $x = 200$ m.

However, from a bit more than $x = 200$ m to 300 m, the height of the water surface remains unchanged (40 m). Amplified three-dimensional tsunami waves are clearly observed at $t = 2$ s, $t = 3$ s and $t = 4$ s (panels $\mathbf{d} - \mathbf{f}$). The tsunami waves propagate in all three directions, as seen from the wavy colour maps. As the momentum intensity of the incoming subaerial mass decreases ($t = 4$ s), the tsunami wave also propagates a bit to the upslope. However, the height of the water wave on the left margin is very low (as indicated by the dark blue) as compared to the height of the total mass in other regions. Therefore, the tsunami wave now also propagates to the left to decrease the impact crater; the wave also moves (disperses) to the lateral direction and the maximum material depth now occurs quite close to $x = 200$ m, which before (for $t = 3$ s, panel **e**) was further right of $x = 200$ m. These basic, but observable natural phenomena have been simulated here for the first time with a real two-phase, and three-dimensional model (Pudasaini, 2012 [98]) by using a high resolution shock capturing scheme [99, 107].

To understand further the dynamics and also the impact of liquid and solid phases separately, Fig. 5.4 and Fig. 5.5 are referred, respectively. Figure 5.4 plots the evolution of the fluid-phase only, as extracted from the total debris from Fig. 5.3. Qualitatively, the total and the fluid-only geometric evolutions are similar. This is so, because, with respect to the amount of the fluid in the reservoir, the fluid component (volume fraction) dominates the solid and thus, the total and the fluid phase evolutions are similar. In

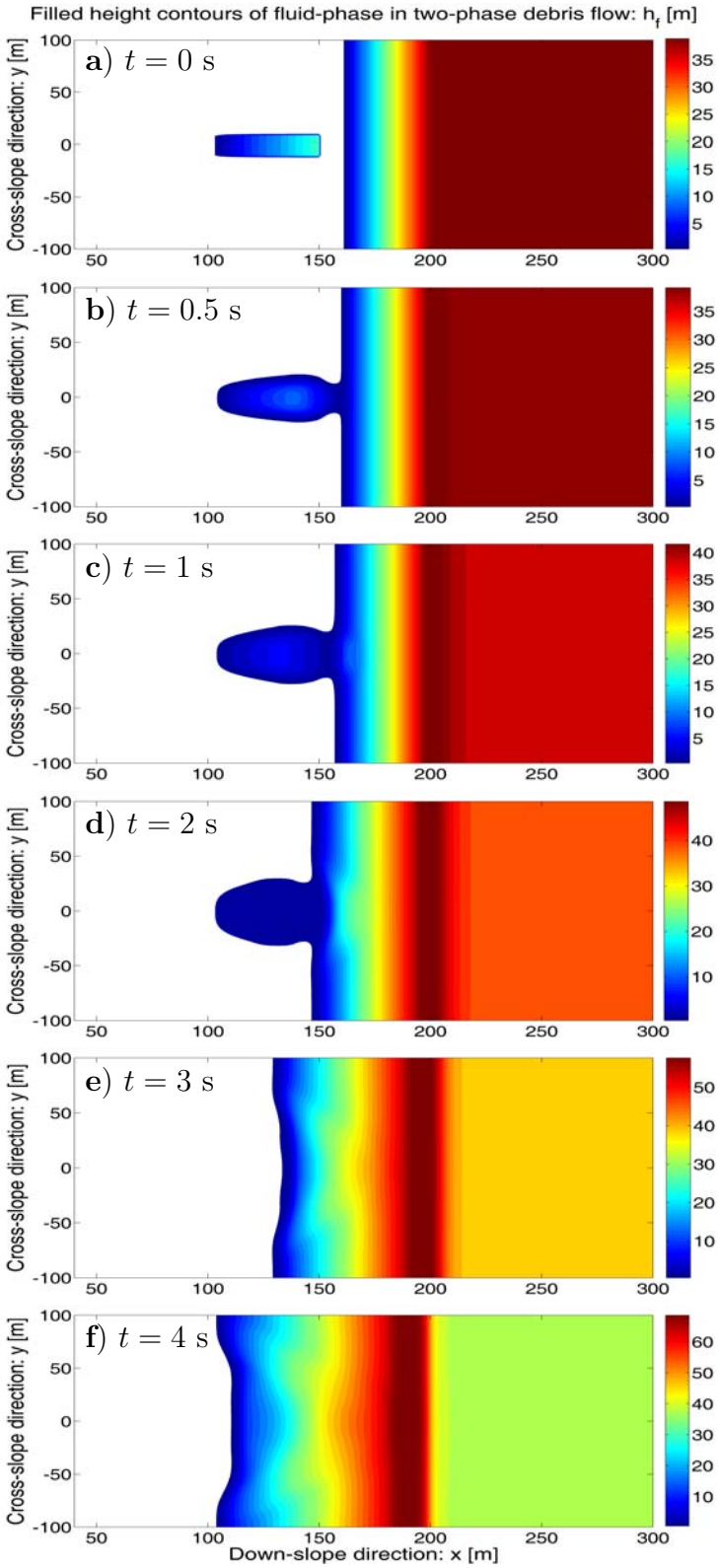

Figure 5.4: Dynamics of the fluid component of Fig. 5.3: Evolution of the fluid-phase only when the reservoir initially contains 2% grain and 98% water. The fluid component dominates the solid and thus the total (Fig. 5.3) and fluid evolutions, here, are similar. In about $t = 3$ s, the fluid mass has almost been mixed-up with the fluid in the reservoir.

about $t = 3$ s, the fluid mass has almost been connected or mixed-up with the fluid in the reservoir. This has created tsunami waves that can be seen both in the simulation of the total mass in Fig. 5.3 and the fluid-only mass in Fig. 5.4. Moreover, the tsunami wave that mainly started at time $t = 2$ s (panel **d**), the tsunami amplitudes in both figures has substantially increased at $t = 3$ s, in panels **e**. This is even more so at panels **f** at $t = 4$ s, where the waves propagate both in the longitudinal and lateral directions, thus, hitting the coastal lines and generating the reflections. However, due to the scaling, the effects of the solid component is not visible in Fig. 5.4.

One of the most important aspects of the real two-phase subaerial debris flows and landslides models simulating their plunging into the water body is the ability to separate investigation and analysis of the solid and the fluid phases both in the subaerial and the submarine environments, mainly in the fluid reservoir, fjords, lakes and ocean. This would not be possible with the single-phase landslide, or avalanche models describing the impacting at the reservoir, or any fluid body. The unified modeling and simulation framework presented by Pudasaini (2012, 2014) [98, 99], and Pudasaini and Miller (2012b) [107] offered this unique possibility. This is required for the detailed and separate study of the particle and sediment transports in fluids such as in the reservoir and aquatic systems, and for the more accurate analysis of the particle transport in the hydroelectric power generating plants and the erosion, e.g., cased by the impacts of the particles on the turbine blades and runners.

For this purpose, the flow behaviour of the solid-only has been presented in Fig. 5.5 as extracted from the total debris from Fig. 5.3. Qualitatively, the dynamics of the total debris (Fig. 5.3) and the fluid-phase (Fig. 5.4) are similar. However, the dynamics of the solid-phase is completely different, mainly in the reservoir, as seen in Fig. 5.5. By analyzing the evolution of the solid-phase, the dynamics of the submarine debris flows, and turbidity currents can be adequately described [99]. So, with respect to Fig. 5.5, it is important to explain the overall dynamics, shape evolution and the propagation of the solid-phase.

There are geometrically many interesting and dynamically many important features in Fig. 5.5. As the mass is released, the front is rarefied, mainly due to the pressure associated with the depth, and also gravity. But, due to the support of the mass from the front and the material frictions, the rear part takes some time to disperse and to slide downslope. The front seems to be accelerating from time $t = 0.5$ s (panel **b**) until $t = 2$ s (panel **d**), then the impact at the reservoir resulted in the deceleration of the front of the solid-mass. Although after the mass collapse, the front is propagating downslope, from

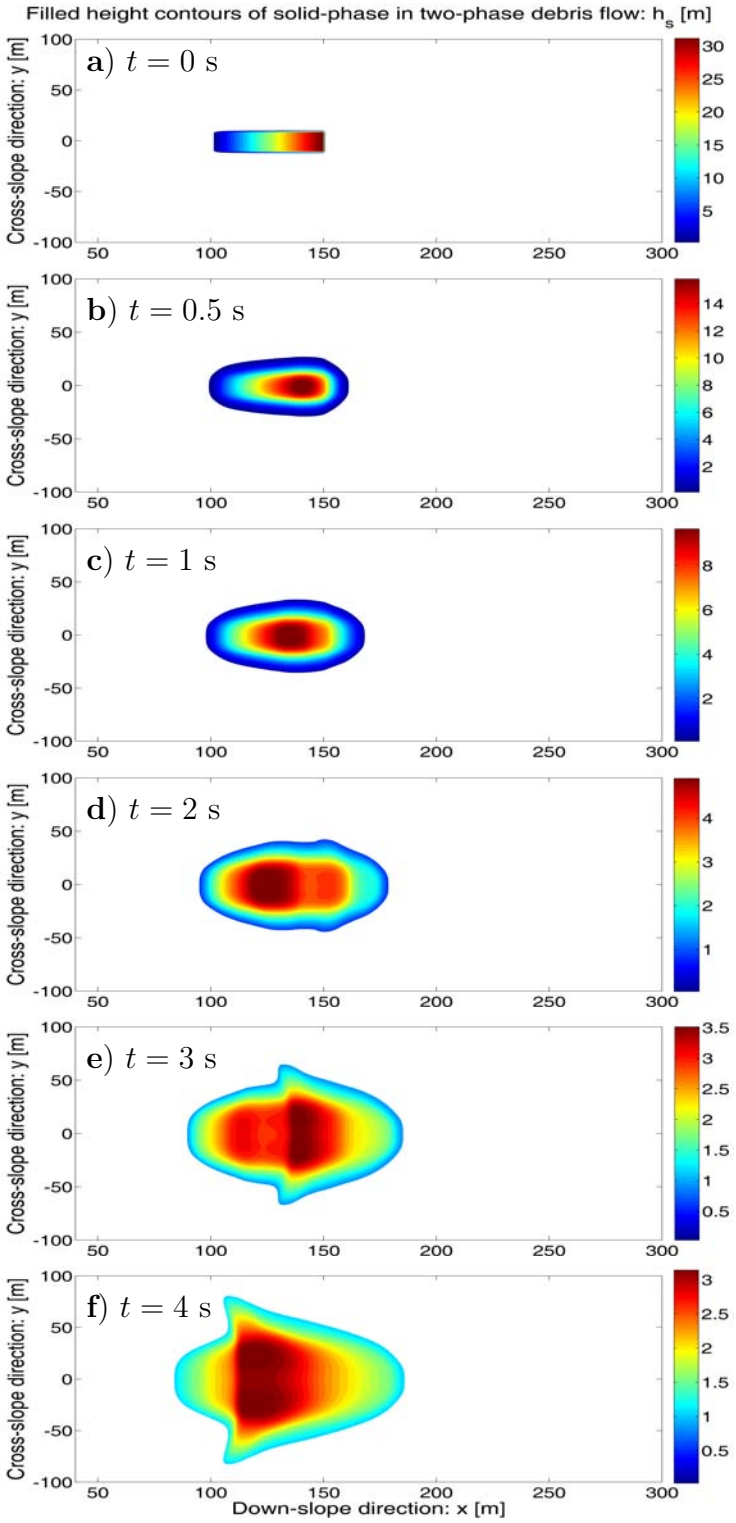

Figure 5.5: Dynamics of the solid component of Fig. 5.3: Evolution of the solid-phase only when initially the reservoir contains 2% grains and 98% water. As soon as mass is released, the front is rarefied and accelerates from time $t = 0.5$ s until $t = 2$ s and the again decelerates. From $t = 2$ s to $t = 4$ s, the solid mass forms a very special forward propagating cone-shaped solid-wave which is similar to a laterally wide and curved barchan-dune form or which is also very close to bell-shaped wave.

time $t = 0.5$ s (panel **b**) to $t = 2$ s (panel **d**), the position of the relative maximum height moves a bit upslope. However, this does not mean that the absolute and the initial maximum is propagating upslope. At time $t = 3$ s (panel **e**), the maximum height position moves downslope, because around this time, the initial solid mass in the backside of the pile, has also been sheared and moved to the downslope direction. Until $t = 2$ s (panel **d**), the solid maximum was elongated in the longitudinal direction.

However, at $t = 3$ s (panel **e**), due to the impact of the subaerial (solid) mass at the reservoir, the solid mass has also been sheared in the cross-slope direction resulting in the cross-wise elongation of both the solid mass from the front to the middle portion until the place where the impact has influenced the dynamics, and also changing the orientation of the maximum solid mass from the longitudinal direction to the lateral direction. Due to the impact induced lateral (along y-direction) spreading of the solid mass, at time $t = 4$ s (panel **f**), again, the relative position of maximum moves a bit back, and two longitudinally-oriented local relative solid maxima are formed. These structures are symmetric to the central line ($y = 0$) of the channel.

Another important aspect is the geometrical shape change of the mass during the slide and motion, mainly its deformation. This is particularly interesting as soon as the debris mass hits the fluid reservoir at time $t = 2$ s (panel **d**). Due to the impact at the fluid reservoir, from $t = 2$ s (panel **d**) to $t = 4$ s (panel **f**), this forms a forward propagating cone-shaped solid-wave. This is due to the fact that, before the debris impact at the reservoir, the solid-phase characteristically was elongated in the down-slope direction. As soon as the subaerial mass impacted the reservoir, the solid (as well as the fluid) mass was also pushed (sheared) to the lateral (y) direction. However, since the debris is plunged into the reservoir, such a forward facing, propagating and expanding complex conical-wave was developed and that evolved as the debris mass continues to impact the reservoir and the debris slides along the basal surface of the reservoir. Fig. 5.5 also shows the propagation of the turbidity current and somehow diffused solid waves.

II. Change in the Solid Concentration in the Reservoir

Now, the effects of the amount of grain in the reservoir to the tsunami generation, and submarine debris mass movements are analyzed in detail for different time slices.

Figure 5.6 describes the result for the evolution of the total debris mass when the subaerial debris mass, as in Fig. 5.3, hits the reservoir at time $t = 0.5$ s. But, now, for panel **a**, the reservoir contains 100% water and 0% solid grain, for panel **b**, the reservoir contains 90% water and 10% solid grains, and for panel **c**, the reservoir contains 80% water and 20%

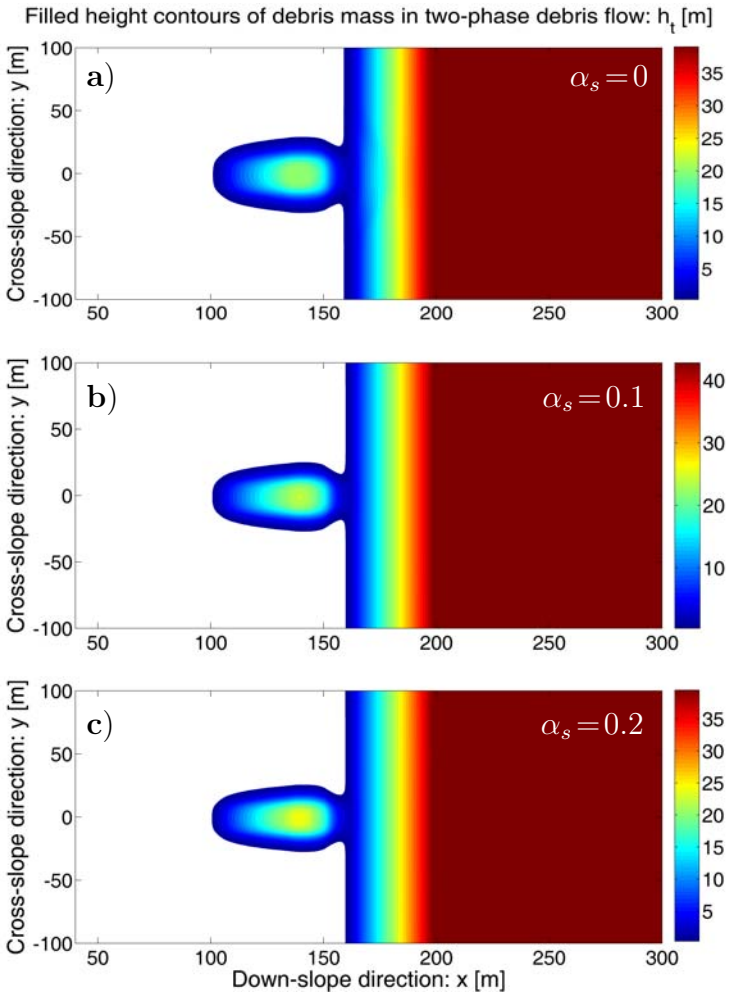

Figure 5.6: Total height of the debris mass flow at time $t = 0.5$ s when the subaerial two-phase debris has just hit the fluid reservoir. Initially, the reservoirs in panel **a**, panel **b**, and panel **c**, respectively, contain 0%, 10%, and 20% solid grains, while the initial subaerial debris consists of 70% solid grains as in Fig. 5.3.

solid grains. At time $t = 0.5$ s, the debris mass just hits the center of the left coast of the reservoir. So, there is no substantial difference between the three panels as the tsunami has not yet been fully produced, and the debris mass has not yet been penetrating the fluid reservoir.

Figure 5.7 displays the total debris depth for time $t = 1$ s in which the initial conditions are the same as in Fig. 5.6. At this time, the debris mass continues hitting the reservoir. The tsunami wave has clearly been produced in panel **a**, that is also evident by the increased water depth in the reservoir by the pushed water and wave to nearly 45 m (forward direction). However, in other two panels, the reservoir water has been pushed a bit to the right and the water depth has been increased considerably, nevertheless the

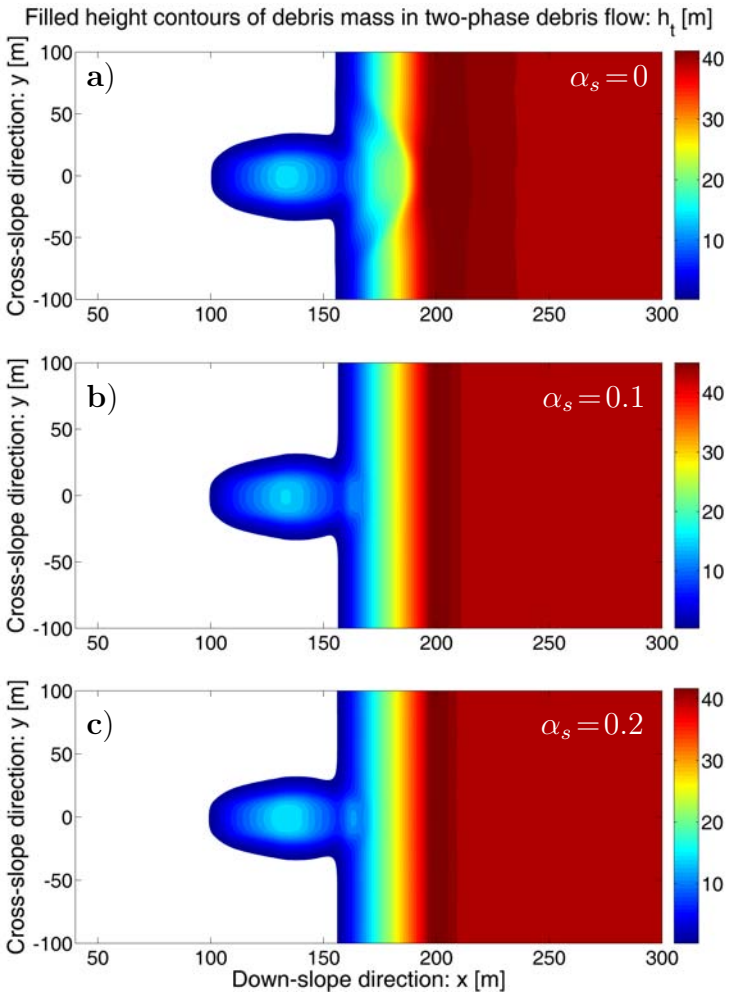

Figure 5.7: Total height of debris flow at time $t = 1$ s when initially the reservoir contains 0% grain in panel **a**, 10% grain in panel **b** and 20% grain in panel **c**.

tsunami has not yet been developed. This indicates that tsunami, with less intensity, is produced as the percentage of the grain constituent increases in the reservoir. This is due to the fact that less number of grains in the reservoir implies, e.g., less drag and less friction, leading to the less disturbed forward motion of the fluid in the reservoir.

Now, Fig. 5.8 is for the total height of the debris mass flow at time $t = 2$ s after the subaerial two-phase debris has hit the fluid reservoir. Initially, the reservoirs in panel **a**, panel **b**, and panel **c**, respectively, contain 0%, 10%, and 20% solid grains, while the initial subaerial debris consists of 70% solid grains. Large deformations and waves with large amplitude are seen in the reservoir in panel **a**. However, panel **b** and panel **c** are similar with small waves. In panel **a**, the tsunami wave is propagating along the channel (downstream) with the largest amplitude transversely curved wave in the central part of the channel. There are two other smaller waves propagating to the lateral coastal direc-

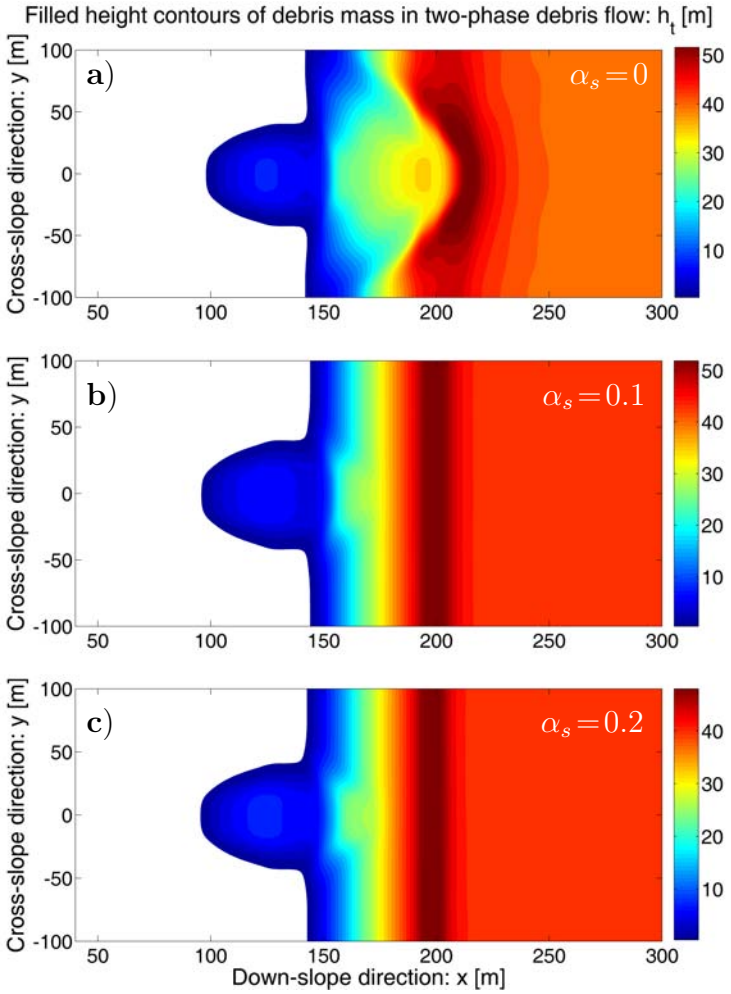

Figure 5.8: Total height of the debris mass flow at time $t = 2$ s after the subaerial two-phase debris has hit the fluid reservoir. Initially, the reservoirs in panel **a**, panel **b**, and panel **c** contains 0%, 10%, and 20% solid grains, respectively, while the initial subaerial debris consists of 70% solid grains. Large deformations and large amplitude transversely curved waves are seen in the reservoir in panel **a**. Panel **b** and panel **c** are similar with small waves.

tions of the reservoir. From panel **a** to panel **c**, it can be seen that tsunami propagation towards the right coast (forward direction) increases with the decrease of the percentage of solid grain in the reservoir.

At time $t = 3$ s (see, Fig. 5.9), although panel **b** and panel **c** are similar and the waves are just a bit more amplified than the waves in the corresponding panels in Fig. 5.8, there are large changes between the panel **a**, here and the corresponding panel **a** in Fig. 5.8. The tsunami wave now propagates in all four directions. There are four waves. Two large amplitude waves are formed close to the lateral walls of the reservoir dam. The

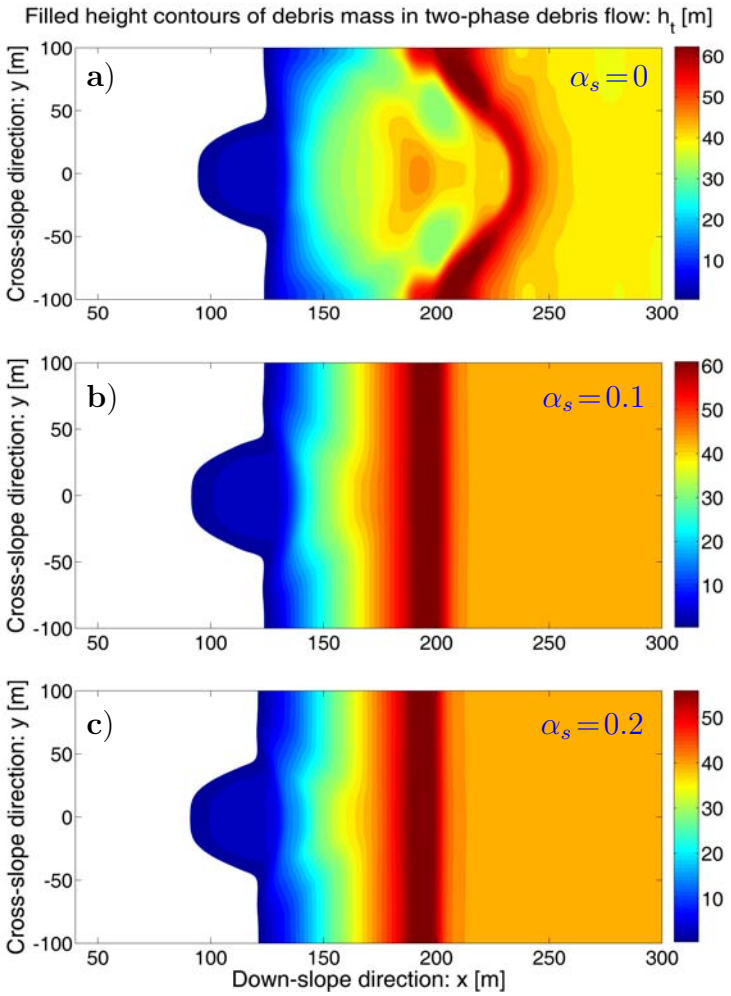

Figure 5.9: Total height of debris flow at time $t = 3$ s after debris hit the reservoir. Tsunami wave now propagates in all three directions. Initially, the reservoirs in panel **a**, panel **b**, and panel **c** contain 0%, 10%, and 20% solid grains respectively, while the initial subaerial debris consists of 70% solid grains. Among the three tsunami waves in panel **a**, two large amplitude waves are close to the lateral walls of the reservoir and the third is at the central region of the channel. A fourth low amplitude concave upward wave is propagated upslope. In panel **b** and panel **c**, waves are amplifying and propagating.

largest amplitude of the waves are due to the reflected waves from the side walls of the reservoir. There is a third local maximum wave height at the central region of the channel (around $x = 200$ m). All the waves are propagating forward. A fourth (concave upward) wave has been formed just behind the impact region. This is the low amplitude wave and propagates upslope by filling the vacuum of the impact creator as the momentum of the impacting subaerial debris decreases. The maximum height of the tsunami is nearly 62 m at panel **a** (0% solid grain and 100% fluid), nearly 60 m at panel **b** (10% solid grains

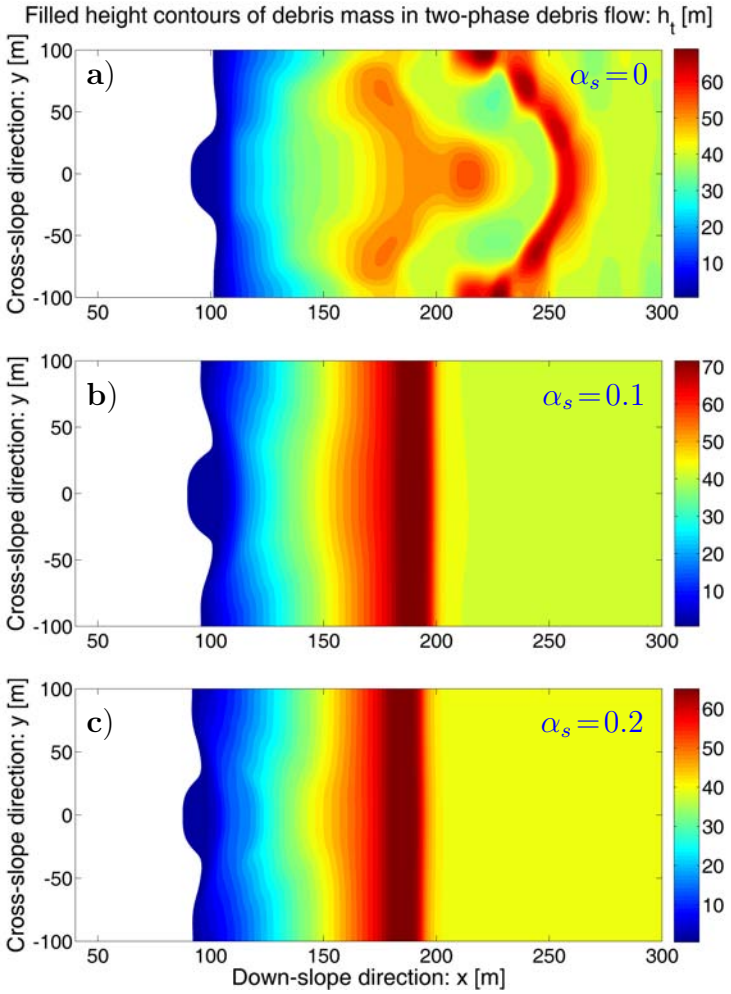

Figure 5.10: Total height of debris flow at time $t = 4$ s after debris hits the reservoir. Initially, the reservoir in panel **a** does not contain any grain, whereas the reservoirs in panel **b** and panel **c** contain 10% and 20% grains. In all three panels, subaerial materials have been fully integrated with the reservoir. In panel **b** and panel **c**, the waves are relatively small and are mainly pushed in the downstream direction whereas in panel **a**, there are several tsunami waves; the main tsunami wave shows a rapidly forward propagating concavely curved annulus-type structure. There are complex wave propagations, reflections and interactions, as observed mainly in the forward propagating disturbance of the reservoir fluid.

and 90% fluid) and close 55 m at panel **c** (20% solid grains and 80% fluid).

At time $t = 4$ s (see, Fig. 5.10), the tsunami continues moving further with wide area and now, towards the right coast. Now, all the subaerial materials have been fully integrated with the reservoir. Again, here, in panel **b** and panel **c**, the waves are relatively small and are mainly pushed in the downstream direction. Panel **b** and panel **c** are similar.

However, there are many interesting dynamics in panel **a**. There are large and several tsunami waves. The main tsunami wave shows a rapidly forward propagating concavely curved annulus-type structure. There are complex wave propagations, reflections and interactions, as observed mainly in the forward propagating disturbance of the reservoir fluid. Large amplitudes of the wave are seen near the lateral side walls of the reservoir between $x = 200$ m to $x = 260$ m. However, there are other three small amplitude waves propagating downstream, and also a bit in the cross-stream directions, forming a connected-triangular-structure between $x = 150$ m to $x = 225$ m. Furthermore, since the material coming from the subaerial inclined slope has now been seized, there is another new low amplitude wave propagating to the upstream direction to fill the crater formed by the subaerial debris impact. So, all together, there are three complex self-inter-connected surface tsunami waves. In between these three waves, the fluid level is relatively low. At the same time, there is another wave, namely the submarine debris wave, that propagates along the bottom of the reservoir. This has been shown in Fig. 5.11 to Fig. 5.12 and explained later.

The reservoir in panel **a** (Fig. 5.10) does not contain any grain, whereas the reservoirs in panel **b** and panel **c**, respectively, contain 10% and 20% grains. Now, the further important aspect is that, with the increasing concentration of the solid in the reservoir, the rear position of the upstream propagating tsunami wave moves more to the left. This clearly shows that, the drag and friction are increased with the increasing amount of the grains in the reservoir thereby hindering the forward motion of the fluid. So, in this situation, the fluid is forced a bit to move backward with the increasing amount of grains in the reservoir. The important point here is that, the amount of grain in the reservoir plays very crucial role in the formation of the tsunami waves, wave structure, amplitude, complex wave interactions, and the entire dynamics of the solid and fluid phases in the reservoir.

Thus, the tsunami intensity decreases when percentage of solid grain in reservoir increases. So, by increasing the solid grain percentage in the reservoir, the solid and fluid dynamics in the reservoir and, the impact force in the embankments, reservoir walls, and hydraulic channels can be controlled.

III. Full Dynamics with the Pure Water Reservoir

As discussed earlier, the resulting tsunami generation, amplification and propagation with different percentage of solid grains in the reservoir, it is observed that the magnitude of the tsunami waves were much higher and well intensified when the solid grain percentage was low. This motivates for the study of the full solid, fluid, and total debris dynamics

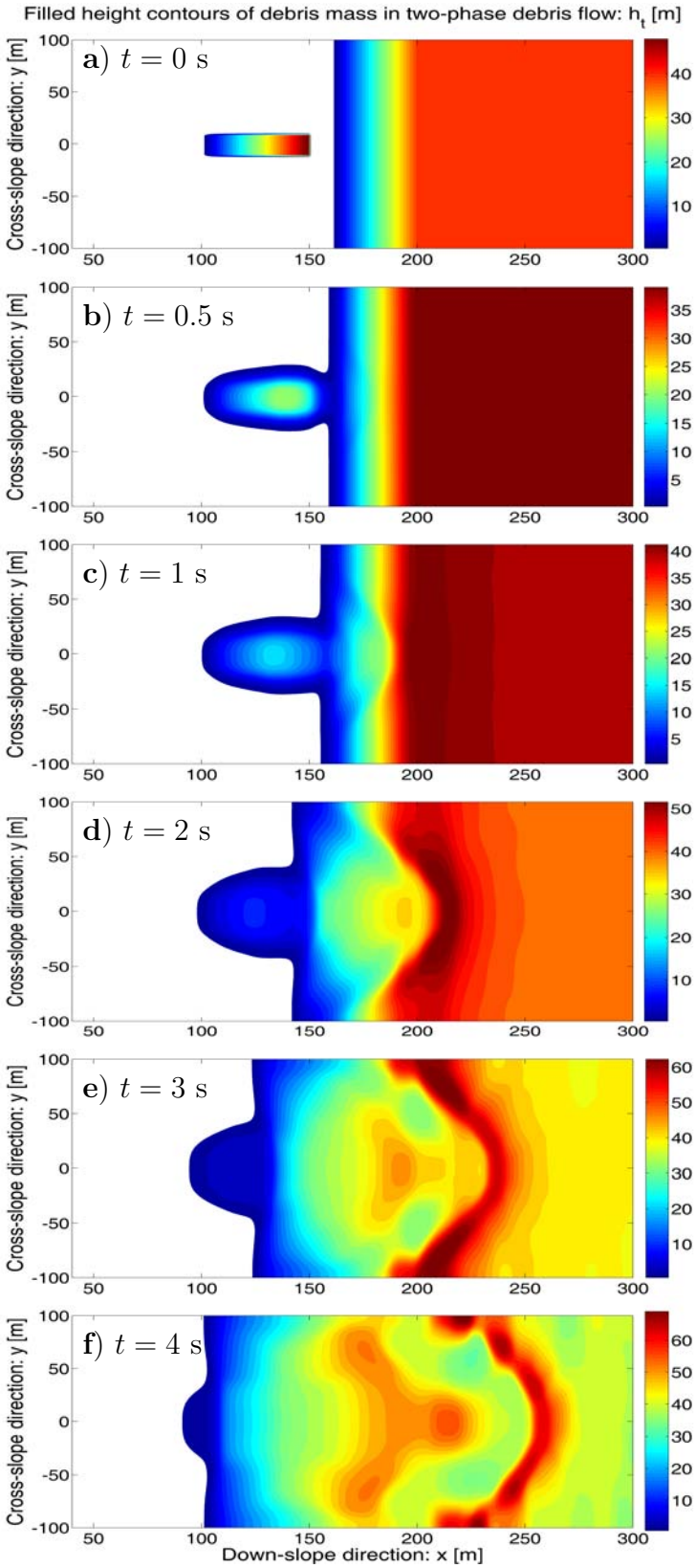

Figure 5.11: Total height of the debris mass when initially the reservoir contains 0% solid grain, so water only, while the initial subaerial debris consists of 70% solid grains. As time elapses, the formation, amplification, propagation, reflection and intersection of coupled three-dimensional tsunami waves are observed as subaerial two-phase debris mass impacts the quiescent water reservoir.

with pure water in the reservoir as an idealized applied problem, e.g., hydropower generating reservoir.

Now, the phenomena for solid, fluid and the total debris are separately analyzed, when the reservoir consists of pure water, so no solid grain. In the previous paragraphs, it has already been discussed about the dynamics of the flow and waves in panels **a** from Fig. 5.6 to Fig. 5.10. In Fig. 5.11, as the time progresses, the total debris mass hits the left coast of the reservoir more and more. Tsunami waves are clearly seen from $t = 1$ s (panel **c**). Water in the reservoir is also continuously pushed towards the right coastal line. The tsunami is more intensified and propagating towards the right coast. The fluid reservoir is pushed forward after $t = 1$ s (panel **c**). Tsunami waves with large amplitude are propagating towards the right coast. There are two other similar waves propagating to the lateral coastal sides. After $t = 3$ s (panel **e**), the tsunami waves propagate in all three directions, two waves with higher amplitude are formed near the lateral walls of the dam, whereas the third wave has been generated at the central region of channel. At $t = 4$ s (panel **f**), it is observed that the subaerial debris bulk is almost integrated with the fluid in the reservoir. Then, the submarine debris waves continues to propagate. The complex wave propagations, reflections and interactions are also observed in the forward propagating disturbance of fluid in the reservoir. The main tsunami wave shows a forward rapid propagating concave annalus type curved structure.

Figure 5.12 plots the dynamics of solid part only when there is no grain in the reservoir. In early stages the solid mass dispersed mainly in the longitudinal direction. The solid debris mass disperses in the lateral direction as the time progresses. As soon as the debris mass collapses, the solid part advects downslope and at the same time, it also disperses laterally. The advection and spreading can be clearly seen from $t = 0.5$ s (panel **b**). The relative solid maximum is a bit pushed back after $t = 2$ s (panel **d**). This is due to the impact of the debris mass with the reservoir. At $t = 3$ s (panel **e**), the solid relative maximum advected downslope again starts and continues. The stretching and the thinning of the solid mass in the debris in the front part starts from $t = 3$ s (panel **e**). More solid mass is mixed with the water in the reservoir after $t = 4$ s (panel **f**). However, the rare part is not moving forward substantially.

At $t = 2$ s (panel **d**), it is observed that the relative solid maximum at the center moves a bit back but at $t = 3$ s (panel **e**), this has moved forward. Surprisingly, it is again pushed back at $t = 4$ s (panel **f**). This implies that the material and fluid wave in the reservoir are substantially affecting the solid mass distribution in the reservoir. However, the colour maps tell us that the solid height is continuously decreasing as time progresses, thereby

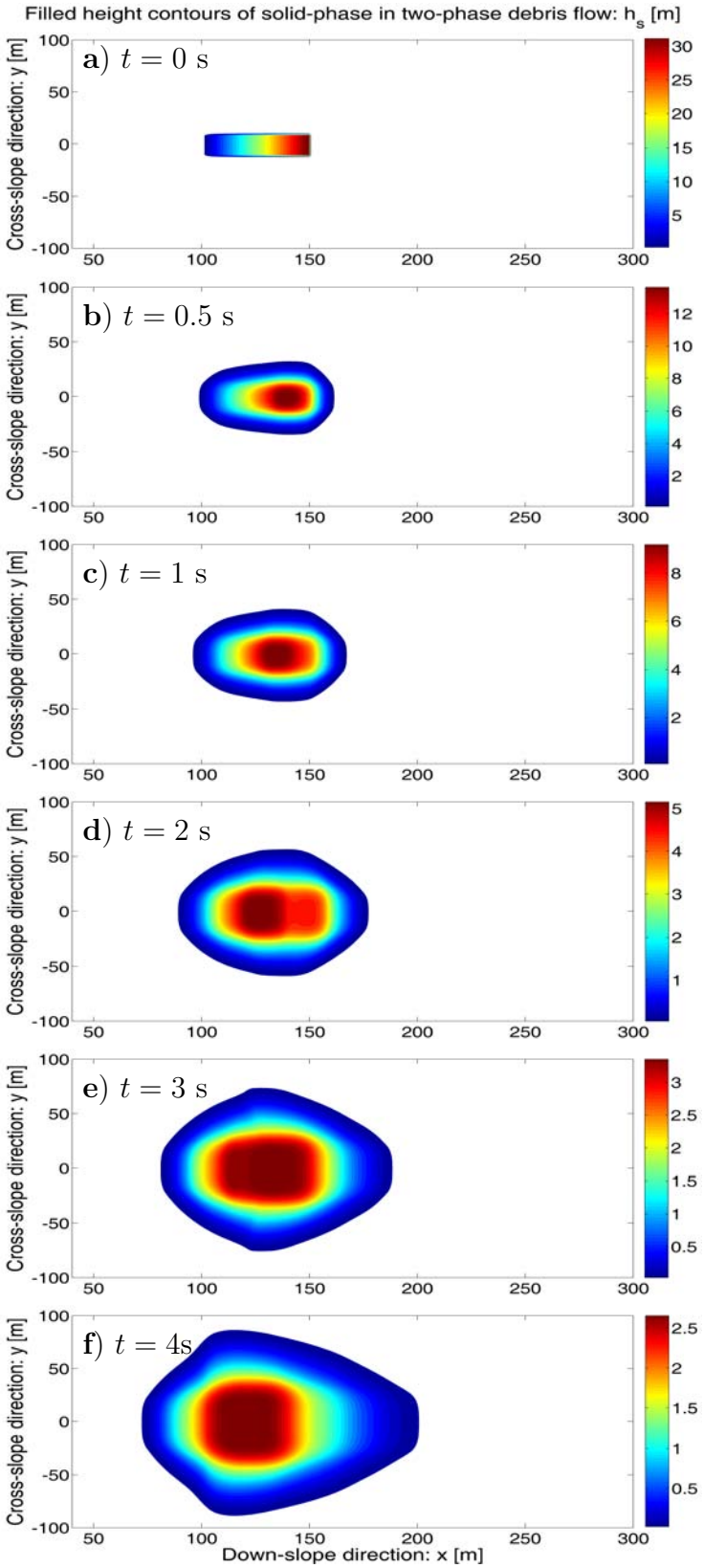

Figure 5.12: Dynamics of solid component of Fig. 5.11: Evolution of the solid-phase only when initially the reservoir contains no solid grain, while the initial subaerial debris consists of 70% solid grains.

showing the substantial dispersion and movement of the solid mass both longitudinally and laterally in the subaerial and submarine region.

In Fig. 5.5, the two lobes in the lateral direction were clearly seen in 3 s (panel **e**), whereas, in Fig. 5.12, the lobes could not be formed. Importantly, in Fig. 5.12, the solid mass is more dispersed in both lateral and longitudinal directions due to less drag and less friction associated with pure water in the reservoir. The most important aspect here is direct comparison between Fig. 5.5 for which the reservoir consist of 2% solid and Fig. 5.12 for which the reservoir consist of only pure fluid (water).

The evolution of solid reveals largely different dynamics, the form and mass distribution. Stretchy difference evolution began mainly after the subaerial debris impact the reservoir at about $t = 1s$ (panel **c**). Since in Fig. 5.12 reservoir consists of only pure water, as the debris impacts and penetrates the reservoir, solid mass is a bit dispersed in the marginal area, but maintains large central longitudinally oriented plateau like solid shock structure, which was not observed from $t = 1$ s (panel **c**) to $t = 4$ s (panel **f**) in Fig. 5.5. The maximum position in panel **f** in Fig. 5.5 is around $x = 110$ m, whereas in panel **f** in Fig. 5.12, it is elongated in x-direction between about $x = 100$ m to $x = 140$ m. This may strike in Fig. 5.12 the reservoir consists of pure water, the submarine debris can move with less dispersion, in a form of an internal shock wave, with the maximum position much further than in Fig. 5.5 where due to the presence of solid grains in the reservoir, the submarine debris and also solid mass is dispersed forming more like a turbidity current.

Another important aspect of Fig. 5.5 is the formation of the laterally sheared forward propagating very special cone shape solid wave (barchan-dune form, or bell type wave). This structure in Fig. 5.5 has been produced due to the drag and the enhanced viscous stress in the reservoir associated with solid grains. However, since Fig. 5.12, the reservoir has no solid grain, such a special structure could not be formed there. Hence, the dynamics of the submarine debris flow is largely influenced by the amount of the solid grain in the reservoir.

Figure 5.13 plots the dynamics of the fluid part only when there is no grain in the reservoir. As in Fig. 5.4, the fluid component dominates the solid, so, the dynamics of the total debris mass and the fluid only are similar. In both figures, fluid mass completely mixes with the fluid height that can be seen in the reservoir. In Fig. 5.4 where there was 2% grains in the reservoir, the tsunami waves were seen in $t = 2$ s (panel **d**), but in Fig. 5.13, the tsunami waves are seen already after $t = 1$ s (panel **c**). Unlike in Fig. 5.4, there are several local maxima of the fluid heights can been seen from time $t = 3$ s (panel **e**) to

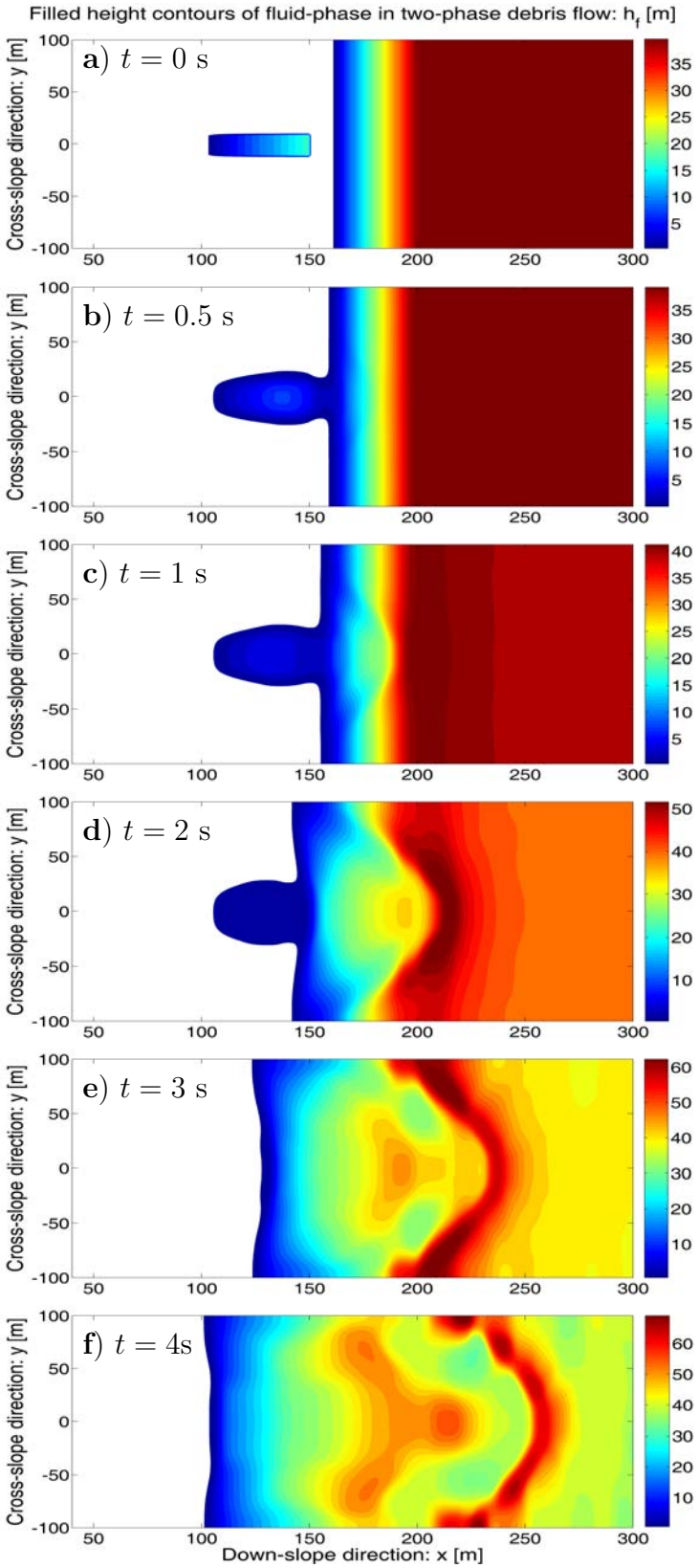

Figure 5.13: Dynamics of fluid component of Fig. 5.11: Evolution of the fluid-phase only when initially the reservoir contains no solid grain, while the initial subaerial debris consists of 70% solid grains.

$t = 4$ s (panel **f**) in Fig. 5.13. Large wave generation, amplification and propagation in the reservoir in Fig. 5.13 is due to fact that reservoir contains pure water, whereas, as in Fig. 5.4, that was hindered due to the presence of grains in the reservoir that increased drag against the motion and enhanced the fluid shear stress.

By properly translating the debris flow topography and the real field reservoir's physical settings in terms of our modeling and computational code, the magnitude and run-ups of the possible tsunamis and submarine sediment transport can be described, which can be useful for the prevention and mitigation plan.

5.3.4 An Outlook

The main aspect of this dissertation was to present and highlight some basic mechanisms of two-phase debris flow, its impact to and interaction with an initially quiet idealized fluid reservoir, submarine debris flow, and complex wave interactions including submarine debris wave and surface tsunami. Another aspect was to investigate the model performance through some numerical simulations. The results demonstrate that the general two-phase debris flow model (Pudasaini, 2012) [98] is able to adequately describe the complex dynamics of two-phase subaerial debris flows; particle-laden and dispersive flows; sediment transports; debris induced tsunamis and submarine debris flows; turbidity currents and associated sophisticated phenomena including the solid and fluid waves and their complex interactions and dynamic impacts. This helps to develop insight into the basic features of the complex non-linear solid and fluid behaviour and their interactions.

The information obtained from simulations can be useful for early warning strategies in the coastal regions, mountain lakes and hydropower plants. These findings substantially increase our understanding of complex multi-physics systems and multi-phase flows. Furthermore, they allow for the proper modeling of landslide and debris induced tsunami, the dynamics of turbidity currents and sediment transport, and the associated applications to hazard mitigation, geomorphology and sedimentology. Applications of these model simulations include: sediment transport on hill slopes, river streams, hydraulic channels (e.g., hydropower reservoirs and plants); lakes, fjords, coastal lines, and aquatic ecology; and submarine debris impact and the rupture of fiber optic, submarine cables and pipelines along the ocean floor, and damage to offshore drilling platforms. So, the basic results of this thesis can be expanded and utilized in the general description of particle-laden flows.

However, the simulation results have yet to be compared and validated with laboratory and/or field data, which is not within the scope of the present work. Furthermore, here,

the geometrically idealized three-dimensional and two-phase submarine debris flows and associated tsunami have been presented. These results present only a possible basic scenario, which however, may be much more complicated while dealing with the complex flows in real three-dimensional natural setting with lateral spreading, diffusion and accumulation during the deposition processes, and their applications with GIS or DTM (Fischer et al., 2012; Mergili et al., 2012) [23, 79]. These results can also be extended to more complete and full-dimensional simulations without depth-averaging (Domnik and Pudasaini, 2012; Domnik et al., 2013) [16, 17].

From the simulation point of view, one should focus on the development of an efficient and robust discretization for the emerging extended two-phase model for arbitrary three-dimensional topographies, with the proper choice of high order methods. A robust numerical methods built on reliable error estimates should use adaptivity in time and space for integrating the more advanced and suitable constitutive models. To accurately account for erosion and deposition an adaptive basal surface needs to be employed. This may be tested along with a recent innovative description of an automatically evolving general pressure- and rate-dependent yield-strength and Coulomb-Viscoplastic sliding law (Domnik et al., 2013) [17].

As well documented experimental data of real two-phase debris flows, with a largely varying degree of physical parameters, are not yet available, a further important direction of research would be to develop and conduct experimental investigations in physical model tests. Experiments can be conducted with dry, partly saturated, or saturated initially released debris mass. In these experiments, the debris mixture and the reservoir should consists of water, granular sand, gravel, silt and clay. The measurement engineering should consists of high-speed cameras, ultrasonic devices, pressure gauges and force plates. Such model tests should yield unique sets of data which are applicable for detailed validation and calibration of the extended general two-phase model (Pudasaini, 2012) [98], and should include the distributions of particle concentration, viscosity, non-Newtonian viscous shear stress, velocity, height, internal and wall frictions, etc. The set of data obtained this way can significantly improve the quality of the numerical predictions of granular and debris flows, mud flows, mud floods and water waves. Another very interesting future work would be to perform well-controlled laboratory experiments in which the solid concentration in the reservoir can be changed systematically in order to investigate the dynamics of two-phase submarine debris flow and to utilize these data to validate the model and the simulation results, e.g., in connection to the particle-laden flows in the hydraulic channels and plants.

Chapter 6

Summary

Gravitational flows like submarine and subaerial landslides and debris avalanches may generate tsunami waves as they hit some water body such as ocean, reservoir, lake or fjord. In this work, the tsunami trigger, types and impact have been introduced. The tsunami generated by landslides and debris flows have been discussed briefly. Also some aspects of tsunami scenarios, some other related geo-physical hazards and the respective mitigation strategies are presented. Moreover, different modeling approaches like single-phase models, quasi two-phase models and general two-phase mass flow models are presented.

Alongwith some rheology related to two-phase mixture flows, a three-dimensional and two-phase mass flow model proposed by Pudasaini (2012) [98] has been presented with focus to the depth-averaged model equations. Special features of the two-phase model equations are discussed. This shows that the two-phase debris flow model by Pudasaini (2012) [98] is the most general two-phase mass flow model to date which incorporates several dominant physical aspects of mass flows like the enhanced non-Newtonian viscous stress, virtual mass, generalized drag and buoyancy.

Two-dimensional high-resolution numerical simulation method, especially the Total Variation Diminishing Non Oscillatory Central Difference (TVD-NOC) is discussed along with its applications in two-phase debris flow model. The simultaneous dynamic simulation of the two-phase, geometrically three-dimensional subaerial debris flow, the resulting tsunami generation and propagation upon debris impact at the reservoir, the subsequent submarine debris flow, and the entire analysis of all three types of waves and their complex interactions are studied, and are simulated by applying the two-phase model [98] together with a high-resolution shock-capturing numerical scheme. With this result, a detailed analysis has been made on how the three-dimensional subaerial debris mass sliding

down an inclined surface penetrates a rectangular fluid reservoir and generates a three-dimensional tsunami, and how the submarine debris mass moves on the bottom of the reservoir basin [99, 107]. The analysis includes the generation, amplification and propagation of super tsunami waves and run-ups along coastlines, debris slide at the bottom floor, sediment transport and mechanism for the turbidity current and debris shock waves.

The employed simulation mainly focuses on: (*i*) initially the constant solid concentration in the reservoir, (*ii*) change in the solid concentration in the reservoir, and (*iii*) full dynamics of the total debris, fluid phase and solid phase evolution in the reservoir with pure water. The simulation results show that the amount of grains in the reservoir plays a significant role in controlling the overall dynamics of the tsunami wave and the submarine debris flow. It is observed that when the percentage of the solid grain increases in the reservoir, tsunami with less intensity is produced. This important result can be used to generate early warning signals in coastal regions, and also can be used to prevent possible catastrophic dam collapses.

. The simulation results show that when a real two-phase debris mass slides down an inclined plane, the debris height increases quickly from the front to the main body of the debris mass whose maximum height appears to be closer to the frontal part of the debris mass than to the middle part. The subaerial debris mass spreads downslope and cross-slope. When sliding debris mass hits the reservoir, tsunami waves are generated in the vicinity of the impact and are amplified when the fluid mass is pushed forward, and a three dimensional hydrodynamic impact vacuum is created. The produced tsunami waves propagate in all three directions.

When analysing the flow of solid (only) components of the debris mass, the solid mass forms a very special forward propagating cone-shaped solid-wave which is similar to a laterally sheared and curved barchan-dune form or, which is also very close to a bell-shaped wave. In case of pure water in the reservoir, the formation, amplification, propagation, reflection and intersection of the coupled three-dimensional tsunami waves are observed as subaerial two-phase debris mass impacts the quiescent water reservoir as time elapses. It was also found that the material and the fluid wave in the reservoir are substantially affecting the solid mass distribution in the reservoir.

These results can further be applied to properly analyze the stability of reservoir dams, embankments and slopes in response to the fluctuation of the water level (due to landslide impact) in the reservoir and lakes which plays a crucial role in the evolution of the pore-fluid pressure and seepage conditions. Similarly, the unified model and computational

technique can be applied to simulate sediment transport in hydro-electric power-plants and to advanced estimation of erosion on the power generating turbines. These basic results are simulated here with a two-phase mass flow model by applying a high resolution shock capturing scheme. This innovative approach allows for the adequate modeling of debris induced tsunami and submarine sediment transport, with significant applications in hazard mitigation, sedimentology, submarine geodynamics, and the integrity of hydro-electric power plants.

Bibliography

[1] S. Abadie, D. Morichon, S. Grilli, and S. Glockner. Numerical simulation of waves generated by landslides using a multiple-fluid Navier-Stokes model. *Coastal Engineering*, 57(9):779–794, 2010.

[2] A. A. Antobreh and S. Krastel. Mauritania slide complex: Morphology, seismic characterisation and processes of formation. *International Journal of Earth Sciences*, 96:451–472, 2007.

[3] R. A. Bagnold. Experiments on a gravity-free dispersion of large solid spheres in a Newtonian fluid under shear. *Proc. R. Soc. Lond., Ser. A*, 225:49–63, 1954.

[4] S. R. Bajracharya and P. Mool. Glaciers, glacial lakes and glacial lake outburst floods in the Mount Everest Region, Nepal. *Annals of Glaciology*, 50(53):81–86, 2009.

[5] D. Berzi and J. T. Jenkins. A theoretical analysis of free-surface flows of saturated granular liquid mixtures. *J. Fluid Mech.*, 608:393–410, 2008a.

[6] D. Berzi and J. T. Jenkins. Approximate analytical solutions in a model for highly concentrated granular-fluid flows. *Phys. Rev.*, 78:011304, 2008b.

[7] N. P. Bhandary, R. K. Dahal, and M. Okamura. Preliminary understanding of the Seti River debris-flood in Pokhara, Nepal, on may 5th, 2012- A report based on a quick field visit program. *ISSMGE Bulletin*, 6(4):8–18, 2012.

[8] C. S. Campbell. Rapid granular flows. *Annu. Rev. Fluid Mech.*, 22:57–92, 1990.

[9] C. Cecioni. *Numerical Modeling of Waves for a Tsunami Early Warning System.* Ph. D. Dissertation, Universit Degli Studi ROMA TRE, 2010.

[10] M. C. Chiou, Y. Wang, and K. Hutter. Influence of obstacles on rapid granular flows. *Acta Mechanica*, 175:105–122, 2005.

[11] S. H. Chou, L. S. Lu, and S. S. Hsiau. Dem simulation of oblique shocks in gravity-driven granular flows with wedge obstacles. *Granular Matter*, 14:719–732, 2012.

[12] G. B. Crosta, H. Chen, and C. F. Lee. Replay of the 1987 Val Pola Landslide, Italian Alps. *Geomorphology*, 60:127–146, 2004.

[13] F. Da Cruz, S. Emam, M. Prochnow, J. N. Roux, and F. Chevoir. Rheophysics of dense granular materials: Discrete simulation of plane shear flows. *Phys. Rev. E*, 72:021309, 2005.

[14] X. Cui, J. M. N. T. Gray, and T. Johannesson. Deflecting dams and the formation of oblique shocks in snow avalanches at Flateyri, Iceland. *Journal of Geophysical Research*, 112:F04012, 2007.

[15] A. Defina, F. M. Susin, and D. P. Viero. Bed friction effects on the stability of a stationary hydraulic jump in a rectangular upward sloping channel. *Physics of Fluids*, 20(3):036601–1, 2008.

[16] B. Domnik and S. P. Pudasaini. Full two-dimensional rapid chute flows of simple viscosplastic granular materials with a pressure-dependent dynamic slip-velocity and their numerical simulations. *J. Non-Newtonian Fluid Mech.*, 173-174:72–86, 2012.

[17] B. Domnik, S. P. Pudasaini, R. Katzenbach, and S. A. Miller. Coupling of full two-dimensional and depth-averaged models for granular flows. *J. Non- Newtonian Fluid Mech.*, 201:56–68, 2013.

[18] D. A. Drew. Mathematical modelling of two-phase flow. *Ann. Rev. Fluid Mech.*, 15:261–291, 1983.

[19] A. Emmer and V. Vilmek. Review article: Lake and breach hazard assessment for moraine-dammed lakes: an example from the Cordillera Blanca (Peru). *Nat. Hazards Earth Syst. Sci.*, 13:1551–1565, 2013.

[20] T. Faug, B. Chanut, M. Naaim, and B. Perrin. Avalanches overflowing a dam: dead zone, granular bore and run-out shortening. *Annals of Glaciology*, 49:77–82, 2008a.

[21] T. Faug, M. Naaim, and A. Fourriere. Dense snow flowing past a deflecting obstacle: An experimental investigation. *Cold Regions Science and Technology*, 49(1):64–73, 2007.

[22] E. D. Fernandez-Nieto, F. Bouchut, D. Bresch, M. J. Castro Diaz, and A. Mangeney. A new Savage-Hutter type model for submarine avalanches and generated tsunami. *J. Comput. Phys.*, 227(16):7720–7754, 2008.

[23] J. T. Fischer, J. Kowalski, and S. P. Pudasaini. Topographic curvature effects in applied avalanche modeling. *Cold Reg. Sci. Tech.*, 74-75:21–30, 2012.

[24] A. Foerster, R. G. Ellis, R. Henrich, S. Krastel, and A. J. Kopf. Geotechnical characterization and strain analyses of sediment in the Mauritania Slide Complex, NW-Africa. *Mar. Pet. Geol*, 27:1175–1189, 2010.

[25] K. Fujita, T. Eyal, S. Chaiken, Y. Trope, and N. Liberman. Influencing attitudes toward near and distant objects. *Journal of Experimental Social Psychology*, 44:562–572, 2008.

[26] K. Fujita, A. Sakai, S. Takenaka, T. Nuimura, A. B. Surazakov, T. Sawagaki, and T. Yamanokuchi. Potential flood volume of Himalayan glacial lakes. *Nat. Hazards Earth Syst. Sci.*, 13:1827–1839, 2013.

[27] J. Geersen, D. Voelker, J. H. Behrmann, C. Reichert, and S. Krastel. Pleistocene giant slope failures offshore Arauco Peninsula, Southern Chile. *Journal of the Geological Society*, 168:1–12, 2011.

[28] R. Genevois and M. Ghirotti. The 1963 Vaiont Landslide. *Giornale di Geologia Applicata*, 1:41–52, 2005.

[29] M. Govi, G. Gulla, and P. G. Nicoletti. Val Pola rock avalanche of July 28, 1987, in Valtellina (Central Italian Alps.), in S.G. Evans and J.V. Degraff (eds.) Catastrophic landslides: Effects, occurances and mechanism. *Geological Society of America Reviews in Engineering Geology*, 15:71–81, 2002.

[30] J. M. N. T. Gray. Granular flow in partially filled slowly rotating drums. *J. Fluid. Mech.*, 441:1–29, 2001.

[31] J. M. N. T. Gray, Y. C. Tai, and S. Noelle. Shock waves, dead zones and particle free regions in rapid granular free surface flows. *J. Fluid. Mech.*, 491:160–181, 2003.

[32] J. M. N. T. Gray, M. Wieland, and K. Hutter. Gravity-driven free surface flow of granular avalanches over complex basal topography. *Proc. R. Soc. A*, 455:1841–1874, 1999.

[33] R. Greve and K. Hutter. Motion of a granual avalanche in a convex and concave curved chute: Experiments and theoretical predictions. *Phil. Trans. R. Soc. A*, 342:573–600, 1993.

[34] S. T. Grilli, S. Vogelmann, and P. Watts. Development of a 3D numerical wave tank for modeling tsunami generation by underwater landslides. *Engineering Analysis with Boundary Elements*, 26:301–313, 2002.

[35] K. M. Hakonardottir, A. J. Hogg, J. Batey, and A.W. Woods. Flying avalanches. *Geophysical Research Letters*, 30:21–91, 2003a.

[36] M. A. Hampton, H. J. Lee, and J. Locat. Submarine landslides. *Rev. Geophys.*, 34:33–59, 1996.

[37] A. Harten. High resolution schemes for hyperbolic conservation laws. *J. Comput. Phys. Appl. Math.*, 49:357–393, 1983.

[38] K. B. Haugen, F. Lovholt, and C. B. Harbitz. Fundamental mechanisms for tsunami generation by submarine mass flows in idealised geometries. *Mar. Pet. Geol*, 22(1-2):209–217, 2005.

[39] P. Heinrich, A. Piatanesi, and H.Hebert. Numerical modelling of tsunami generation and propagation from submarine slumps: The 1998 Papua New Guinea events. *Geophys. J. Int.*, 145:97–111, 2001.

[40] R. Henrich, T. Hanebuth, S. Krastel, N. Neubert, and R. B. Wynn. Architecture and sediment dynamics of the Mauritania Slide Complex. *Marine and Petroleum Geology*, 25:17–33, 2008.

[41] J. Huebl and H. Steinwendtner. Debris flow hazard assessment and risk mitigation, in: Felsbau. *Rock and Soil Engineering*, 1:17–23, 2000.

[42] O. Hungr. A model for the runout analysis of rapid flow slides, debris flows, and avalanches. *Canadian Geotech. J.*, 32:610–623, 1995.

[43] K. Hutter and L. Schneider. Important aspects in the formulation of solid-fluid debris-flow models. Part I. Thermodynamic implications. *Continuum Mech. Thermodyn.*, 22:363–390, 2010a.

[44] K. Hutter and L. Schneider. Important aspects in the formulation of solid-fluid debris-flow models. Part II. Constitutive modelling. *Continuum Mech. Thermodyn.*, 22:391–411, 2010b.

[45] K. Hutter, B. Svendsen, and D. Rickenmann. Debris flow modelling review. *Continuum Mech. Thermodyn.*, 8:1–35, 1996.

[46] ICIMOD. *Glacial lakes and glacial lake outburst floods in Nepal*. ICIMOD, Kathmandu, 2011.

[47] J. Imran, G. Parker, J. Locat, and H. Lee. One-dimensional numerical model of muddy subaqueous and subaerial debris flows. *J. Hydr. Engng.*, 127:959–968, 2001.

[48] M. Ishii. *Thermo-Fluid Dynamic Theory of Two-Phase Flow*. Eyrolles, Paris, 1975.

[49] M. Ishii and N. Zuber. Drag coefficient and relative velocity in bubbly, droplet or particulate flows. *AIChE J.*, 25:843–855, 1979.

[50] R. M. Iverson. The physics of debris flows. *Rev. Geophys.*, 35(3):245–296, 1997.

[51] R. M. Iverson. Landslide triggering by rain infiltration. *Water Resour. Res.*, 36(3):1897–1910, 2000.

[52] R. M. Iverson. Regulation of landslide motion by dilatancy and pore pressure feedback. *J. Geophys. Res.*, 110:F02015, 2005.

[53] R. M. Iverson and R. P. Denlinger. Flow of variably fluidized granular masses across three-dimensional terrain: 1. Coulomb mixture theory. *J. Geophys. Res.*, 106(B1):537–552, 2001.

[54] R. M. Iverson and R. G. Lahusen. Dynamic pore pressure fluctuations in rapidly shearing granular materials. *Science*, 246:796–798, 1989.

[55] R. Jackson. Locally averaged equations of motion for a mixture of identical spherical particles and a Newtonian fluid. *Ch. Engng Sci.*, 52:2457–2469, 1997.

[56] G. S. Jiang and E. Tadmor. Nonoscillatory cental schemes for multidimensional hyperbolic conservation laws. *SIAM J. Sci. Comput.*, 19:1892–1917, 1998.

[57] P. Jop, Y. Forterre, and O. Pouliquen. A constitutive law for dense granular flows. *Nature*, 441(7094):727–730, 2006.

[58] J. Kafle, P. Kattel, P. R. Pokhrel, K. B. Khattri, D. B. Gurung, and S. P. Pudasaini. Dynamic interaction between a two-phase submarine landslide and a fluid reservoir. *Int. J. Lsld. Env.*, 1(1):35–36, 2013.

[59] J. Kafle, P. Kattel, P. R. Pokhrel, K. B. Khattri, D. B. Gurung, and S. P. Pudasaini. Dynamic interaction between a two-phase submarine landslide and a reservoir. 2014. (Submitted).

[60] P. Kattel. *Dynamics of Quasi-Three-Dimensional and Two-Phase Mass Flows.* M. Phil. Dissertation, Kathmandu University, School of Science, Dhulikhel, Kavre, Nepal, 2014.

[61] P. Kattel, J. Kafle, P. R. Pokhrel, K. B. Khattri, D. B. Gurung, and S. P. Pudasaini. Dynamics of three-dimensional, two-phase landslides and debris flows. *Int. J. Lsld. Env.*, 1(1):39–40, 2013.

[62] P. Kattel, J. Kafle, P. R. Pokhrel, K. B. Khattri, D. B. Gurung, and S. P. Pudasaini. Dynamics imuations of three-dimensional, two-phase landslides and debris flows. 2014. (Submitted).

[63] Y. Kervella, D. Dutykh, and F. Dias. Comparison between three dimensional linear and nonlinear tsunami generation models. *Theor. Comput. Fluid Dyn.*, 21:245–269, 2007.

[64] K. B. Khattri. *Sub-diffusive and Sub-advective Viscous Fluid Flows in Debris and Porous Media.* M. Phil. Dissertation, Kathmandu University, Kavre, Dhulikhel, Nepal, 2014.

[65] K. B. Khattri, P. R. Pokhrel, P. Kattel, J. Kafle, D. B. Gurung, and S. P. Pudasaini. Some new insights into the fluid flows in debris material and porous landscape. *Int. J. Lsld. Env.*, 1(1):39–40, 2013.

[66] K. B. Khattri, P. R. Pokhrel, P. Kattel, J. Kafle, D. B. Gurung, and S. P. Pudasaini. Fluid flows in porous landscape and debris materials: Some new insights. 2014. (Submitted).

[67] T. Koch, R. Greve, and K. Hutter. Unconfined flow of granular avalanches along a partly curved chute II: Experiments and numerical computations. *Proc. R. Soc. A*, 445:415–435, 1994.

[68] S. Krastel, R. B. Wynn, T. J. J. Hanebuth, R. Henrich, C. Holz, H. Meggers, H. Kuhlmann, A. Georgiopoulou, and H. D. Schulz. Mapping of seabed morphology and shallow sediment structure of the Mauritania continental margin, North Africa: some implications on the geohazard potential. *Norwegian J Geol*, 86:163–176, 2006.

[69] P. Lax. Weak solutions of nonlinear hyperbolic equations and their numerical computation. *Comm. Pure Appl. Math.*, 7:159–193, 1954.

[70] F. Legros. The mobility of long-runout landslides. *Eng. Geol.*, 63:301–331, 2002.

[71] R. J. LeVeque. *Numerical Methods for Conservation Laws*. Birkhäuser, Basel, 1990.

[72] K. A. Lie and S. Noelle. An improved quadrature rule for the flux-computation in staggered central difference schemes in multidimensions. *J. Sci. comp.*, 18:69–80, 2003.

[73] P. L. F. Liu, T. R. Wu, F. Raichlen, C. E. Synolakis, and J. C. Borrero. Runup and rundown generated by three-dimensional sliding masses. *Journal of Fluid Mechanics*, 536(1):107–144, 2005.

[74] P. Lynett and P. L. F. Liu. A numerical study of submarine-landslide generated waves and run-up. *Proc. The Royal Society London*, 458:2885–2910, 2002.

[75] J. J. Major and R. M. Iverson. Debris-flow deposition: Effects of pore-fluid pressure and friction concentrated at flow margins. *Geol. Soc. Am. Bull.*, 111:1424–1434, 1999.

[76] C. E. Martinez, F. Miralles-wilhelm, and R. Garcia-martinez. Quasi-three dimensional two-phase debris flow model acounting for boulder transport. *Italian Journal of Engineering Geology and Environment - Book*, 3:457–466, 2011.

[77] D. G. Masson, C. B. Harbitz, R. B. Wynn, G. Pedersen, and F. Lovholt. Submarine landslides: processes, triggers and hazard prediction. *Phil. Trans. R. Soc. A*, 364:2009–2039, 2006.

[78] B. W. McArdell, P. Bartelt, and J. Kowalski. Field observations of basal forces and fluid pore pressure in a debris flow. *Geophys. Res. Lett.*, 34:2009–2039, 2007.

[79] M. Mergili, C. Kopf, B. Mllebner, and J. F. Schneider. Changes of the cryosphere in the High-Mountain areas of Tajikistan and Austria : A comparison. *Geografiska Annaler, Series A*, 94(1):79–96, 2012.

[80] M. Mergili, K. Schratz, A. Ostermann, and W. Fellin. Physically-based modelling of granular flows with Open Source GIS. *Nat. Hazards Earth Syst. Sci.*, 12:187–200, 2012.

[81] H. Miao, G. Wang, K. Yin, T. Kamai, and Y. Li. Mechanism of the slow-moving landslides in Jurassic red-strata in the Three Gorges Reservoir, China. *Engineering Geology*, 2014. doi: 10.1016j.enggeo.2013.12.017.

[82] D. J. Miller. Giant Waves in Lituya Bay, Alaska. *Geological Survey Professional Paper*, 354-C(1):107–144, 1960.

[83] L. Miller. The rock slide in the Vajont Valley. *Rock Mech. Eng. Geoz.*, 2(3-4):148–212, 1964.

[84] F. Mohammed and H. M. Fritz. Experiments on tsunamis generated by 3D granular landslides, submarine mass movements and their consequences. *Journal of Geophysical Research*, 28:705–718, 2010.

[85] M. Naaim, T. Faug, F. Naaim-Bouvet, and N. Eckert. Return period calculation and passive structure design at the Taconnaz Avalanche Path (France). *Annals of Glaciology*, 51(54):89–97, 2010.

[86] Z. Narcisse, P. Efim, T. Tatiana, and N. Irina. Savage-Hutter model for avalanche dynamics in inclined channels: Analytical solutions. *Journal of Geophysical Research*, 115, 2010. B03402, doi:10.1029/2009JB006515.

[87] H. Nessyahu and E. Tadmor. Non-oscillatory central differencing for hyperbolic conservation laws. *Journal of Computational Physics*, 87(2):408–463, 1990.

[88] Y. Okura, H. Kitahara, H. Ochiai, T. Sammori, and A. A. Kawanami. Landslide fluidization process by flume experiments. *Engng Geol.*, 66:65–78, 2002.

[89] M. Pailha and O. Pouliquen. A two-phase flow description of the initiation of underwater granular avalanches. *J. Fluid Mech.*, 633:115–135, 2009.

[90] M. Pastor, M. Quecedo, E. Gonzalez, M. I. Herreros, J. A. Fernandez Merodo, and P. Mira. Simple approximation to bottom friction for Bingham fluid depth integrated models. *J. Hydr. Engrg*, 130:149–155, 2004.

[91] D. A. Petrakov, O. V. Tutubalina, A. A. Aleinikov, S. S. Chernomorets, S. G. Evans, V. M. Kidyaeva, I. N. Krylenko, S. V. Norin, M. S. Shakhmina, and I. B. Seynova. Monitoring of Bashkara glacier lakes (Central Caucasus, Russia) and modelling of their potential outburst. *Nat Hazards*, 2011. doi: 10.1007/s11069-011-9983-5.

[92] H. Philoppe, M. Annc, G. Sandrine, and R. Roger. Simulation of water waves generated by a potential debris avalanche in Montserrat, Lesser Antilles. *Geophysical Research Letters*, 25(19):3697–3700, 1998.

[93] E. B. Pitman and L. Le. A two-fluid model for avalanche and debris flows. *Phil. Trans. R. Soc. A*, 363(3):1573–1601, 2005.

[94] P. R. Pokhrel. *General phase-eigenvalues for two-phase mass flows: Supercritical and subcritical States*. M. Phil. Dissertation, Kathmandu University, Kavre, Dhulikhel, Nepal, 2014.

[95] P. R. Pokhrel, K. B. Khattri, P. Kattel, J. Kafle, G. B. Gurung, and S. P. Pudasaini. Enhanced descriptions of real two-phase landslides and debris flows. *Int. J. Lsld. Env.*, 1(1):75–76, 2013.

[96] P. R. Pokhrel, K. B. Khattri, P. Kattel, J. Kafle, G. B. Gurung, and S. P. Pudasaini. Real two-phase landslides and debris flows: Enhanced simulations. 2014. (Submitted).

[97] S. P. Pudasaini. Some exact solutions for debris and avalanche flows. *Phys. Fluids*, 23(4):043301, 2011.

[98] S. P. Pudasaini. A general two-phase debris flow model. *J. Geophysics. Res.*, 117, 2012. F03010, doi:10.1029/2011JF002186.

[99] S. P. Pudasaini. Dynamics of submarine debris flow and tsunami. *Acta Mechanica*, (Accepted) 2014.

[100] S. P. Pudasaini and B. Domnik. Energy consideration in accelerating rapid shear granular flows. *Nonlin. Processes Geophys*, 16:399–407, 2009.

[101] S. P. Pudasaini, W. Eckart, and K. Hutter:. Gravity-driven rapid shear flows of dry granular massess in helically curved and twisted channels. *Mathematical Models and Methods in Applied Sciences*, 13(7):1019–1052, 2003.

[102] S. P. Pudasaini and K. Hutter. Rapid shear flows of dry granular masses down curved and twisted channels. *J. Fluid Mech.*, 495:193–208, 2003.

[103] S. P. Pudasaini and K. Hutter. *Avalanche Dynamics: Dynamics of Rapid Flows of Dense Granular Avalanches*. Springer, Berlin, New York, 2007.

[104] S. P. Pudasaini and M. Krautblatter. A real two-phase mechanical model for rock-ice avalanches. *Geophysical Research Abstracts*, 14, 2012. EGU2012-2660.

[105] S. P. Pudasaini and C. Kroener. Shock waves in rapid flows of dense granular materials: Theoretical predictions and experimental results. *Physical Review E*, 78:041308, 2008.

[106] S. P. Pudasaini and S. A. Miller. Buoyancy induced mobility in two-phase debris flow. *American Institute of Physics Proceedings*, 1479:149–152, 2012a.

[107] S. P. Pudasaini and S. A. Miller. A real two-phase submarine debris flow and tsunami. *American Institute of Physics Proceedings*, 1479:197–200, 2012b.

[108] S. P. Pudasaini, Y. Wang, and K. Hutter. Modelling debris flows down general channels. *Nat. Hazards Earth Syst. Sci.*, 5:799–819, 2005.

[109] J. M. Reynolds. Glacial hazard assessment at Tsho Rolpa, Rolwaling, Central Nepal. *Q. J. Eng. Geol. Hydroge.*, 32:209–214, 1999.

[110] J. R. Rice. On the stability of dilatant hardening for saturated rock masses. *J. Geophys. Res.*, 80:1531–1536, 1975.

[111] M. Di Risio, P. De Girolamo, G. Bellotti, A. Panizzo, F. Aristodemo, M.G. Molfetta, and A.F. Petrillo. Landslide-generated tsunamis runup at the coast of a conical island: New physical model experiments. *J. Geophys. Res.*, 114, 2009.

[112] J. W. Rudnicki. Effects of dilatant hardening on the development of concentrated shear deformation in fissured rock masses. *J. Geophys. Res.*, 89:9259–9270, 1984.

[113] S. B. Savage and K. Hutter. The motion of a finite mass of granular material down a rough incline. *J. Fluid Mech.*, 199:177–215, 1989.

[114] S. B. Savage and K. Hutter. Dyanamics of avalanches of granular materials from initiation to runout. Part I: Analysis. *Acta Mech.*, 86:201–223, 1991.

[115] D. G. Schaeffer and R. Iverson. Steady and intermittent slipping in a model of landslide motion regulated by pore-pressure feedback. *SIAM Appl. Math.*, 69:768–786, 2008.

[116] R. H. Sharma and R. Awal. Hydropower development in Nepal. *Renewable and Sustainable Energy Reviews*, 21(2):684–693, 2013.

[117] A. B. Shrestha, M. Eriksson, P. Mool, P. Ghimire, B. Mishra, and N. R. Khanal. Glacial lake outburst flood risk assessment of Sun Koshi Basin, Nepal. *Geomatics, Natural Hazards and Risk.*, 1(2), 2010.

[118] L. E. Silbert, D. Ertas, G. S. Grest, T. C. Halsey, D. Levine, and S. J. Plimpton. Granular flow down an inclined plane: Bagnold scaling and rheology. *Phys. Rev. E*, 64(57):051302, 2001.

[119] R. Sosio, G. B. Crosta, and O. Hungr. Complete dynamic modelling calibration for the Thurwieser rock avalanche (Italian Central Alps). *Eng. Geol.*, 100:11–26, 2008.

[120] A. L. Strom and O. Korup. Extremely large rockslides and rock avalanches in the Tien Shan Mountains, Kyrgyzstan. *Landslides*, 3:125–136, 2006.

[121] Y. C. Tai. *Dynamics of Granular Avalanches and Their Simulations with Shock-capturing and Front-Tracking Numerical Schemes*. Ph. D. Dissertation, Darmstadt University of Technology, Darmstadt, Germany, 2000.

[122] Y. C. Tai, J. M. N. T. Gray, K. Hutter, and S. Noelle. Flow of dense avalanches past obstructions. *Annals of Glaciology*, 32:281–284, 2001.

[123] Y. C. Tai, S. Noelle, J. M. N. T. Gray, and K. Hutter. Shock-capturing and front-tracking methods for granular avalanches. *J. Comput. Phys.*, 175(1):269–301, 2002.

[124] T. Takahashi. *Debris Flow*. IAHR-AIRH Monograph Series A, Balkema, Rotterdam, Netherlands, 1991.

[125] S. Tinti, G. Pagnoni, and F. Zaniboni. The landslides and tsunamis of the 30th of December 2002 in Stromboli analyzed through numerical simulations. *Bull. Volcanol.*, 68:462–470, 2006.

[126] Y. Wang, K. Hutter, and S. P. Pudasaini. The Savage-Hutter Theory: A system of partial differential equations for avalanche flows of snow, debris and mud. *Journal of Applied Mathematics and Mechanics*, 84(8):507–527, 2004.

[127] R. Weiss, H. M. Fritz, and K. Wuennemann. Hybrid modeling of the mega-tsunami runup in Lituya Bay after half a century. *Geophys Res. Lett.*, 36, 2009. L09602, doi:10.10292009GL037814.

[128] M. Wieland, J. M. N. T. Gray, and K. Hutter. Channelized free surface flow of cohensionless granular avalanche in a chute with shallow lateral curvature. *J. Fluid. Mech.*, 392:73–100, 1999.

[129] R. Worni, M. Stoffel, C. Huggel, C. Volz, A. Casteller, and Brian Luckman. Analysis and dynamic modeling of a moraine failure and glacier lake outburst flood at Ventisquero Negro, Patagonian Andes (Argentina). *Journal of Hydrology*, 444-445:134–145, 2012.

[130] T. Zwinger, A. Kluwick, and P. Sampl. *Avalanche Flow of Dry Snow over Natural Terrain. Part II: Numerical Simulation. In K. Hutter, N. Kirchner (eds): Dynamic Response of Granular and Porous Materials under Large and Catastrophic Deformations*. Springer, Berlin, New York, 2003.